OPTICALLY PROGRAMMABLE FIELD PROGRAMMABLE GATE ARRAY (FPGA) SYSTEMS

California Institute of Technology

APPROVED FOR PUBLIC RELEASE; DISTRIBUTION UNLIMITED.

AIR FORCE RESEARCH LABORATORY
INFORMATION DIRECTORATE
ROME RESEARCH SITE
ROME, NEW YORK

STINFO FINAL REPORT

This report has been reviewed by the Air Force Research Laboratory, Information Directorate, Public Affairs Office (IFOIPA) and is releasable to the National Technical Information Service (NTIS). At NTIS it will be releasable to the general public, including foreign nations.

AFRL-IF-RS-TR-2004-21 has been reviewed and is approved for publication.

APPROVED: /s/

        PETER J. COSTIANES
        Project Engineer

FOR THE DIRECTOR: /s/

        JOSEPH CAMERA, Chief
        Information & Intelligence Exploitation Division
        Information Directorate

REPORT DOCUMENTATION PAGE

Form Approved
OMB No. 074-0188

1. AGENCY USE ONLY (Leave blank)	2. REPORT DATE JANUARY 2004	3. REPORT TYPE AND DATES COVERED Final Jul 98 – Sep 03	

4. TITLE AND SUBTITLE
OPTICALLY PROGRAMMABLE FIELD PROGRAMMABLE GATE ARRAY (FPGA) SYSTEMS

5. FUNDING NUMBERS
C - F30602-98-1-0199
PE - 62712E
PR - A28E
TA - 00
WU - 02

6. AUTHOR(S)
Jose Mumbru,
George Panotopoulos, and
Demetri Psaltis

7. PERFORMING ORGANIZATION NAME(S) AND ADDRESS(ES)
California Institute of Technology
Department of Electrical Engineering
Pasadena California 91125

8. PERFORMING ORGANIZATION REPORT NUMBER

N/A

9. SPONSORING / MONITORING AGENCY NAME(S) AND ADDRESS(ES)
Air Force Research Laboratory/IFEC
32 Brooks Road
Rome New York 13441-4114

10. SPONSORING / MONITORING AGENCY REPORT NUMBER

AFRL-IF-RS-TR-2004-21

11. SUPPLEMENTARY NOTES

AFRL Project Engineer: Peter J. Costianes/IFEC/(315) 330-4030/ Peter.Costianes@rl.af.mil

12a. DISTRIBUTION / AVAILABILITY STATEMENT
APPROVED FOR PUBLIC RELEASE; DISTRIBUTION UNLIMITED.

12b. DISTRIBUTION CODE

13. ABSTRACT *(Maximum 200 Words)*
This report presents the results of research in the use of holographic modules in optoelectronic systems, their applications, and the characterization of polymer materials on which to record volume holograms for these modules. The first chapter makes the case that a direct interface between an optical memory and a chip integrating detectors and logic circuitry can better utilize the high parallelism inherent in holographic modules.
Introduced also is the idea of reconfigurable computing and Field Programmable Gate Arrays (FPGAs) as the framework in which to design a hybrid system, the Optically Programmable Gate Array (OPGA), that outperforms its electronic counterpart by reducing its reconfiguration time by three orders of magnitude. The OPGA is the combination of three elements: an addressing device to selectively recall holographic data pages, an optical memory, and an optoelectronic chip. We also present a system that uses holograms to extract spatial and color information (4-D imaging) of a specimen and project it on to a 2-D space on the detector. By multiplexing several holograms many depth slices and color bands can be sent in parallel, making unnecessary the use of sophisticated and time-consuming scanning schemes.

14. SUBJECT TERMS
Holography, Holographic Recording, FPGA, Field Programmable Gate Arrays

15. NUMBER OF PAGES
118

16. PRICE CODE

17. SECURITY CLASSIFICATION OF REPORT UNCLASSIFIED	18. SECURITY CLASSIFICATION OF THIS PAGE UNCLASSIFIED	19. SECURITY CLASSIFICATION OF ABSTRACT UNCLASSIFIED	20. LIMITATION OF ABSTRACT UL

TABLE OF CONTENTS

List of Figures

LIST OF TABLES

1 Optically reconfigurable processors

1.1 Introduction

Reconfigurable processors bring a new computational paradigm where the processor modifies its structure to suit a given application, rather than having to modify the application to fit the device. The reconfigurability makes it possible for these processors to use more efficiently their resources by adjusting themselves depending on the characteristics of the input or on nonsatisfactory previous results to better implement the target task.
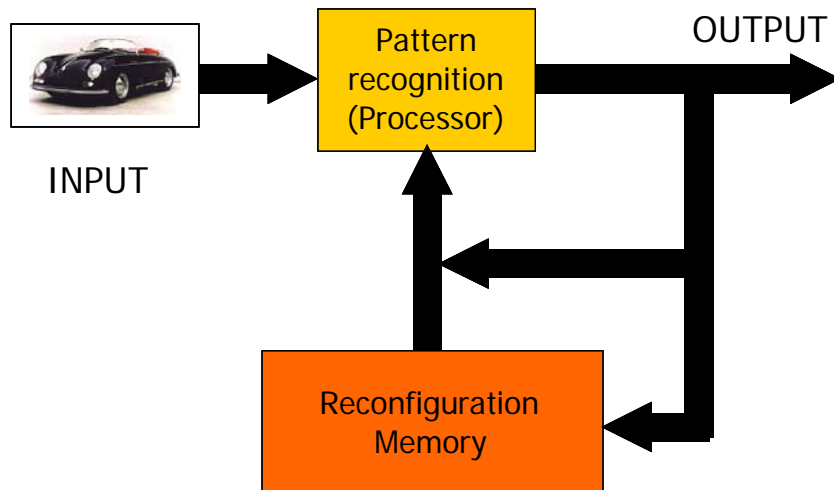
Fig. 1-1.   Reconfigurable processor applied to pattern recognition. The external memory stores the configuration templates that define the functionality of the processor. Using reconfiguration the same processor can perform different tasks on the same input image.

Given an application, like pattern recognition in Figure 1-1, the reconfigurable processor can be customized to deal with a specific class of objects, but with enough flexibility that, if at a later time the salient class of objects shifts to a different one, the device can be reprogrammed to deal with the new problem without degrading its performance. Further-

more, the processor can adapt itself in order to be robust to changes of orientation or illu-mination of the input object. By reprogramming, the same hardware can be time-multiplexed to carry out sequentially several tasks on the same input, or perform different tasks to different parts of the same input image. Reconfiguration also makes it possible to implement learning by allowing the processor to evolve in a controlled manner in order to learn the function that needs to be computed.

In other applications, where it is necessary to implement different concurrent tasks by partitioning the hardware resources among them, a reconfigurable processor can outper-form a nonreconfigurable solution by dynamically reallocating the hardware of idle tasks into those that may be temporarily overflowed. This feature, called spatial multiplexing, becomes especially attractive when partial rather than global reconfiguration is possible because it allows reprogramming part of the device without halting the execution in the rest of it.

In this chapter, we will see how optics can play a very important role in the devel-opment of reconfigurable processors. Section 1.2 provides the reader with a brief descrip-tion of Field Programmable Gate Arrays (FPGAs), while Section 1.3 explains how the performance of a conventional FPGA can be enhanced by interfacing the chip to a holo-graphic memory. Finally, the architecture of the OPGA module and the system design con-siderations are presented in Section 1.4.

1.2 Field Programmable Gate Arrays (FPGAs)

A Field Programmable Gate Array (FPGA) is a device where this idea of reconfig-urable hardware can be implemented. FPGAs emerged as a new technology for the imple-

mentation of digital logic circuits during the mid 1980's. The basic architecture of an FPGA consists of a large number of Configurable Logic Blocks (CLBs) and a programmable mesh of interconnections. Both the function performed by the logic blocks and the interconnection pattern can be specified by the circuit designer. In the beginning FPGAs were mostly viewed as large Programmable Logic Devices (PLDs) and they were usually employed for the implementation of the "glue-logic" used to tie together complex VLSI chips like microprocessors and memories used to build general purpose computers.

While several FPGAs were configured by static RAM (SRAM) cells, this was generally considered a limitation by users concerned about the chip's volatility. For this reason, fuse-based FPGAs were also developed and for many applications were much more attractive, both because they were faster and smaller, due to less programming overhead, and also because there was no volatility in their configuration since this had been burned into the chip. Not until the late 1980's and early 1990's did it become clear that the volatility of SRAM-based FPGAs was not a liability but could open an entirely new spectrum of applications, since the programming of such FPGAs could be changed electrically at almost any point during operation.

These devices have gained popularity due to the fact that they are between a software oriented solution, like a microprocessor running a program stored in memory, and a hardware-oriented solution, like an application specific integrated circuit (ASIC) (Figure 1-2). The FPGA-based solution is faster than a microprocessor or Digital Signal Processors (DSPs) because the FPGA is conceived as a large array of small logic blocks working in parallel and operating at the bit level, exactly where general purpose processors are most inefficient. Even though microprocessors have more capabilities, in order to keep

3
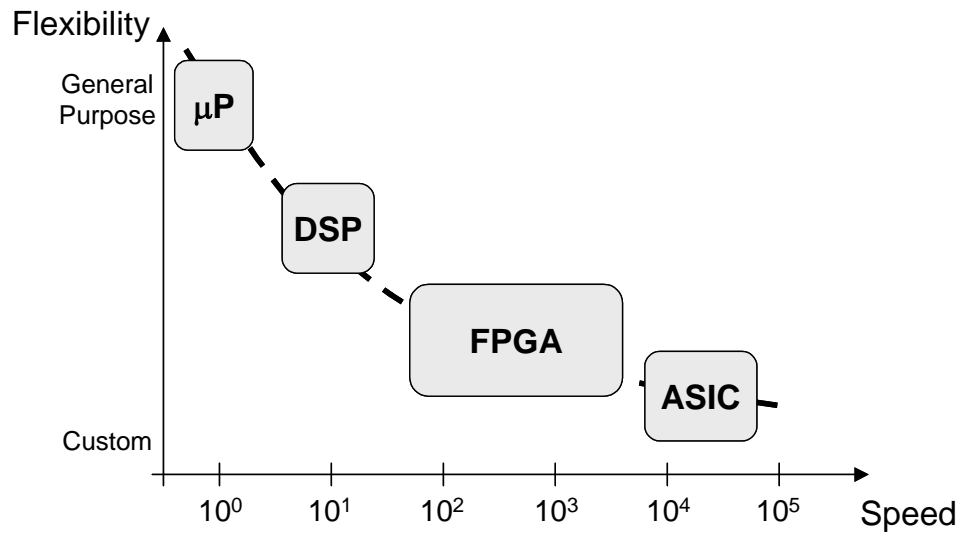
Fig. 1-2. Flexibility/speed trade-off comparison for different hardware implementations: microprocessors (µP); digital signal processors (DSP); field-programmable gate arrays (FPGA); and application specific integrated circuits (ASIC).

their generality, they are still designed to operate with fix data formats (8, 16, 32, 64 bits…). Therefore, they perform poorly when they need to deal with problems where data has "non-standard" lengths. On the other hand, the fine granularity of the computing blocks of the FPGA allows the user to better map the hardware resources of the chip to meet the demands of the problem. Using FPGA platforms, speedups of several orders of magnitude have been achieved for some applications [1-1]-[1-4]. The ASIC solution provides most of the time the optimal implementation both in terms of speed and silicon area requirement, however, it has the drawbacks of being a single-purpose processor. Compared to ASICs, FPGAs are much more flexible since they contain some hardware resources that can be programmed by the user to implement some given task and, by changing that configuration, the same hardware can be used to carry out something totally different with minimal development time and cost.

4

Although FPGA architecture design is a field of important ongoing research in the FPGA community, and many different implementations have already become commercially available, it is beyond the scope of this section to describe all of them. To illustrate the common features of their internal structure, one of the most widely used designs, the symmetric array [1-5], Figure 1-3, will be analyzed. In this case, the logic blocks are
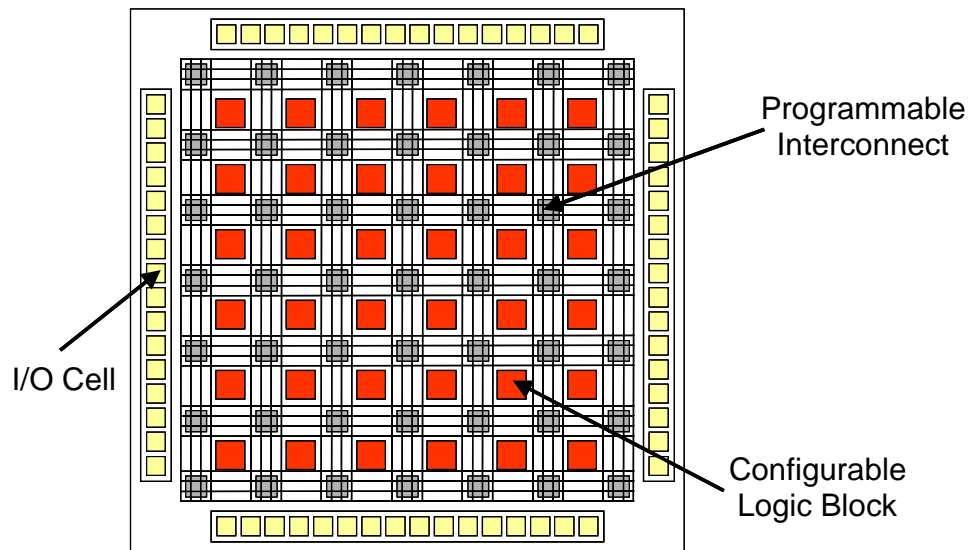
Fig. 1-3. Architecture of a typical FPGA. A symmetric array of CLBs is surrounded by a mesh of buses and matrices of programmable interconnects that provide connectivity among the CLBs, as well as with the input/output (I/O) cells.

arranged in a two-dimensional array and interleaved with vertical and horizontal buses used to establish connectivity among them. Connections between segments in two different buses can also be performed by means of programmable interconnects in switching matrices. Finally, on the periphery of the chip, there are some input/output cells.

The basic functional unit of the FPGA is the Configurable Logic Block (CLB), which implements an elementary Boolean operation. Despite the fact that there are CLBs based on multiplexors or OR-AND arrays, the use of look-up tables (LUTs) to synthesize

5

logic functions enjoys much greater flexibility [1-5]. A LUT can be seen as a small bank of

memory where the inputs encode the address of a position in this memory, which stores the

result of a pre-programmed logic function of the inputs. By changing the bits stored in the

LUT, the function computed is altered.
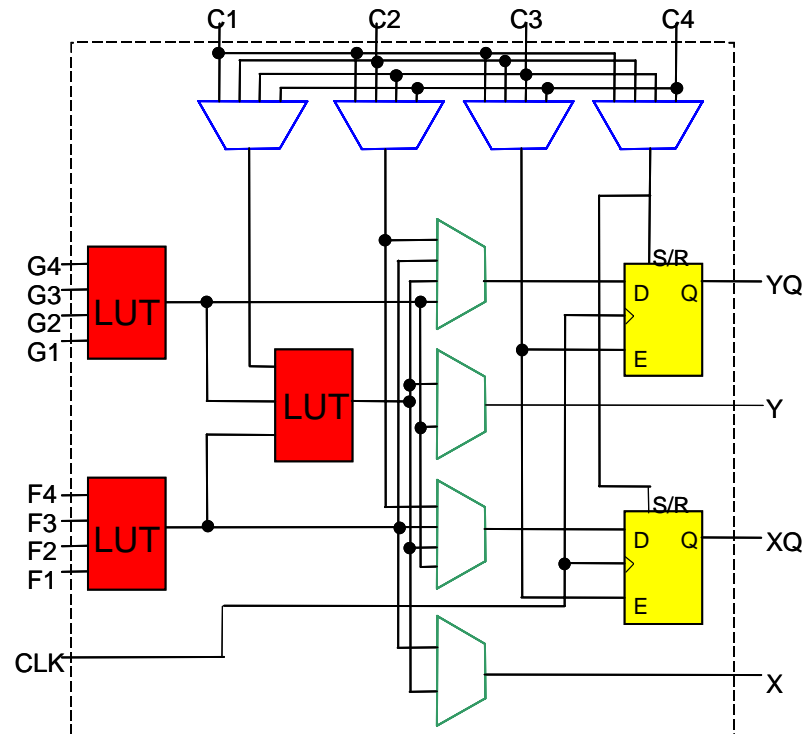
Fig. 1-4.   Schematic of a LUT-based CLB. Two independent sets of inputs F[1:4] and G[1:4] feed
the LUTs on the left of the figure. The outputs of the LUTs can be combined using an additional
LUT for more complex Boolean functions. The control signals C[1:4] define the way the results of
the LUTs are routed to the output of the CLB by means of the multiplexors. This output can be
buffered, which allows implementing sequential logic.

The schematic of a LUT-based CLB is shown in Figure 1-4. In this case, two sets

of inputs, on the left-hand side, feed two independent 4-input LUTs. A third LUT has the

ability of combining the results of the LUTs from the previous stage, increasing the func-

tionality of the CLB to implement more complex logic functions. The two outputs of the

CLB are on the right-hand side and they can be buffered if necessary by means of flip-flops. These registers allow implementing sequential logic in the CLB.

FPGAs have traditionally been used very successfully as accelerators in many applications like signal processing [1-1], image filtering [1-2], automated target recognition [1-3], or cryptography [1-4]. In a typical arrangement, as shown in Figure 1-5, the
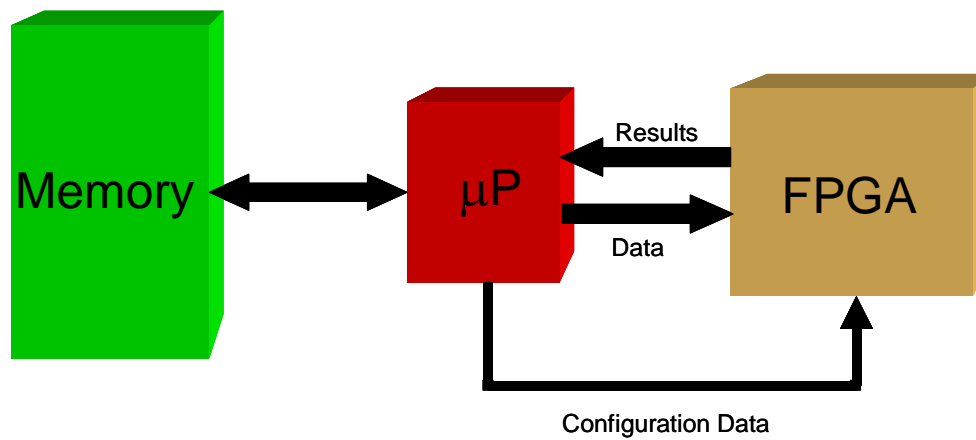
Fig. 1-5. FPGAs are usually used as accelerators. The master processor (µP and memory) programs the slave processor (FPGA) to perform those most computationally intense tasks.

FPGA is setup as a coprocessor that is controlled by the microprocessor. For a given application, if there is some task that is computationally very expensive, the microprocessor can program the FPGA to perform that task much faster than if it was executed by the main processor. The configuration data of the FPGA, which specifies the values in the LUTs and the interconnection pattern, is stored in an external memory, in most cases an EPROM, and downloaded into the FPGA chip on demand. The microprocessor just feeds the data into the FPGA and waits for the results, and all the cumbersome computation has been hardwired inside the FPGA.

7

Although the size of these devices, in terms of logic gates, can vary among different models and manufacturers, they can easily contain on the order of 10^5 gates and the trend is to keep increasing the logic density to go beyond the million-gate FPGA. This means that the configuration data page for a medium size FPGA can be as large as 1 Mbit. Despite the fact that the FPGA can be reprogrammed multiple times, the user typically does not take advantage of this feature. In most cases, the FPGA is configured only once and this configuration is downloaded into the FPGA off-line, before the execution is started. The main reason for not reconfiguring dynamically the device, i.e., changing its internal configuration once the execution has started and some data is already flowing into the device, has been the small communication bandwidth between the external configuration memory and the FPGA chip itself. The configuration bandwidth of the FPGA has not scaled well enough to keep up with the enormous data throughput. Upon programming, the configuration data is downloaded serially by shifting a long bit stream into the FPGA. The transfer data rate between memory and FPGA is only on the range of 100 Mbps, which results on configuration times of tens or even hundreds of milliseconds. These long reconfiguration times, if compared to clock cycles of just tens of nanoseconds and input/output throughputs reaching 100 Gbps, become an important overhead. Some attempts to decrease the reconfiguration times have been proposed, like providing a dedicated parallel bus to increase the bandwidth with the configuration memory, or having fast-access cache memory built in the chip [1-6],[1-7]. Both solutions only contribute to further increase the already high power dissipation of the FPGAs, which although application dependent can easily be in the range of 1–10 Watts.

1.3 Optically Programmable Gate Array

Optical memory modules possess inherently a high degree of parallelism, since the data is handled in the format of pages. Such parallelism results in a large communication bandwidth between the memory and the array of photodetectors during a readout cycle, or the Spatial Light Modulator (SLM) upon recording. The use of optical memories in information processing systems makes it necessary to consider the interface between the holographic module and the silicon circuitry that processes the data retrieved from the memory and stores computational results.

Traditionally, holographic systems have not addressed this issue, so even though the information can be delivered very fast to and from the optical memory, this parallelism is lost in the communication between the optoelectronic chips and the processor, becoming a bottleneck. Therefore, a direct interface between memory and processor would be much more effective since the parallelism would always be preserved, as suggested in Figure 1-6. The direct interface avoids the slow interchip communication by simply integrating on the same silicon die the logic circuitry and an array of photodetectors. However, the question now is to identify which computing devices have enough hardware parallelism to exchange data efficiently with the optical memory. It is here that the distributed hardware resources of the FPGA marry the parallelism of the optical memory.

Based on the FPGA architecture, the OPGA [1-8] is a device where the computation is still performed by programmable logic blocks and interconnects as in the conventional FPGA, but where the configuration data is brought into the chip optically. The design of the OPGA is conceptually different from a similar system described in [1-9], in which the information is brought into the chip via optical I/O ports while the configuration is still per-
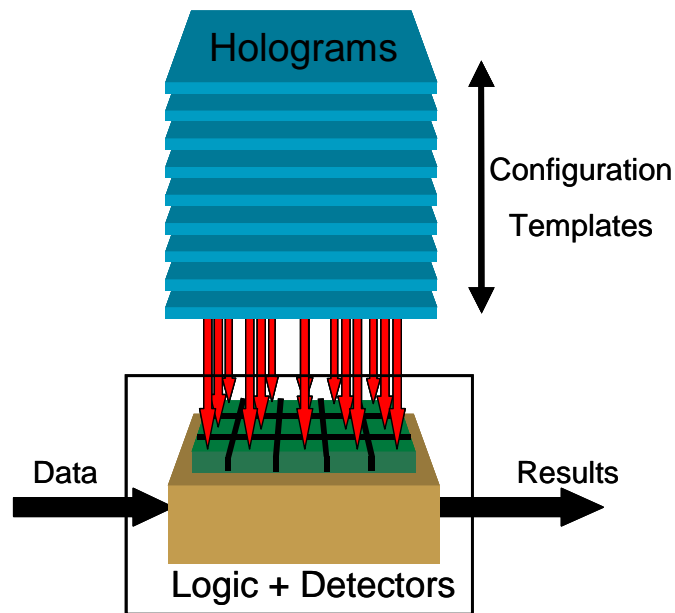
Fig. 1-6. Direct interface between the optical memory and the silicon chip carrying photodetectors and logic circuitry. The configuration templates stored as holograms (depicted as slices) can be downloaded in parallel to the chip.

formed electronically. This optical reconfiguration capability in the OPGA results from interfacing an optical memory with an optoelectronic chip, as illustrated in Figure 1-6. The holographic memory can store a large number of configuration templates that can be transferred down to the FPGA chip as a single page. By taking the reconfiguration circuitry out of the FPGA chip, the OPGA can achieve a larger logic density, i.e., more CLBs can be implemented, than in the conventional device.

In its initial implementation, the OPGA module is intended to operate as a Holographic Read-Only Memory (HROM), where a priori and for a given application, the user will decide the library of different configuration templates that needs to be stored in the memory. This frees the OPGA module from all the optics and optoelectronics required to write in the memory, like the SLM, and makes it very compact. However, it is conceivable

that future OPGA designs encompass both read and write capabilities, which would enable an increased computational flexibility.

The OPGA is basically the integration of three main components or technologies: an array of vertical cavity surface-emitting lasers (VCSELs) used to retrieve the templates stored in the memory; the optical memory that contains a large set of configuration contexts; and the VLSI chip that combines CMOS logic and photodetectors. Each one of these components presents a number of issues that will be discussed in the next chapter.

1.4 OPGA system architecture

The technique used to store and multiplex the holograms in the optical memory determines the architecture of the entire module. For this reason, it is not possible to discuss the holographic memory, the VCSEL array, or the chip separately without giving first a more general view to the system involving these three elements. The OPGA has the potential to outperform conventional FPGAs in two different aspects:

- **Number of fast-access configurations:** The OPGA module can contain one hundred holographic templates, formatted as pages of 1000×1000 pixels, so there is enough information in each hologram to program a medium-sized FPGA. Compared to cache-based FPGAs, in which between four and eight configurations are stored locally [1-6], the 100 templates stored in the optical memory represent a two-order of magnitude increase in flexibility for the OPGA.

- **Reconfiguration speed:** The parallel interface between holographic memory and chip makes it possible to decrease reconfiguration times in two or three orders of magnitude and go from the millisecond regime in electric FPGAs down to micro-

seconds in their optical counterpart. The reconfiguration time of the device depends greatly on the optical power available per VCSEL and is eventually limited by the integration time of the photodetectors, being the target configuration time between 1–100 µs.

This section introduces the two architectures that have been considered for the OPGA module, compares the main system-level requirements of the two designs, and discusses how they are interrelated.

1.4.1 Transmission-geometry OPGA module

The initial design for the OPGA consisted of a symmetric transmission-geometry module as depicted in Figure 1-7. Each one of the VCSELs in the array is used to record a different hologram in the memory, which in this case is a thin layer of red-sensitive photopolymer. For a matter of robustness, the polymer film is sandwiched between two prisms.
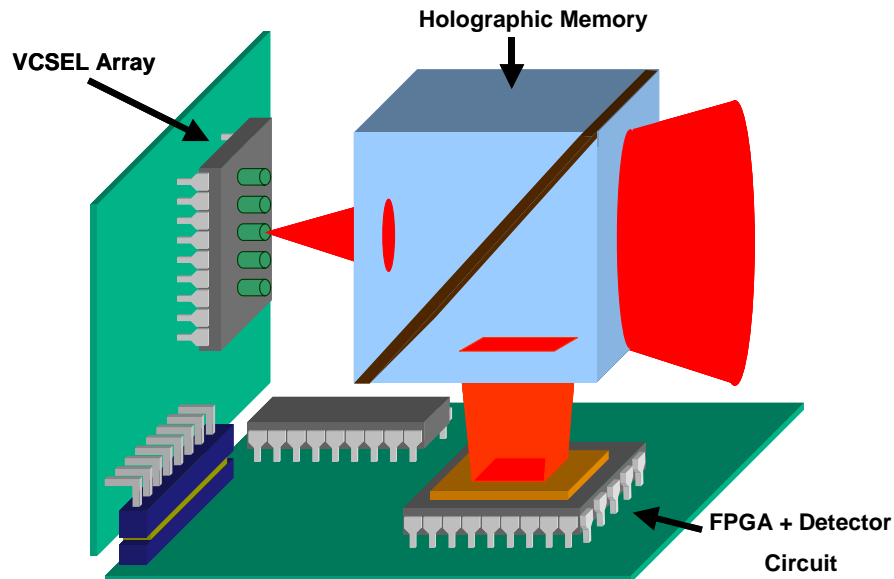
Fig. 1-7.   Transmission-geometry OPGA module. The spherical wave emitted by the VCSEL retrieves a holographic template from the optical memory and projects it onto the photodetector array in the chip.

12

The technique used to multiplex the holograms is shift multiplexing with spherical reference [1-10],[1-11]. Therefore, the shift selectivity of the material needs to be matched to the spacing between adjacent VCSELs in order not to have crosstalk between data pages. Phase-conjugate reference is used to read out the holographic templates, so the reconstructions self-focus on the array of photodetectors on the FPGA chip. Since no additional optics is required for the readout, the module is very compact.

(a)	(b)
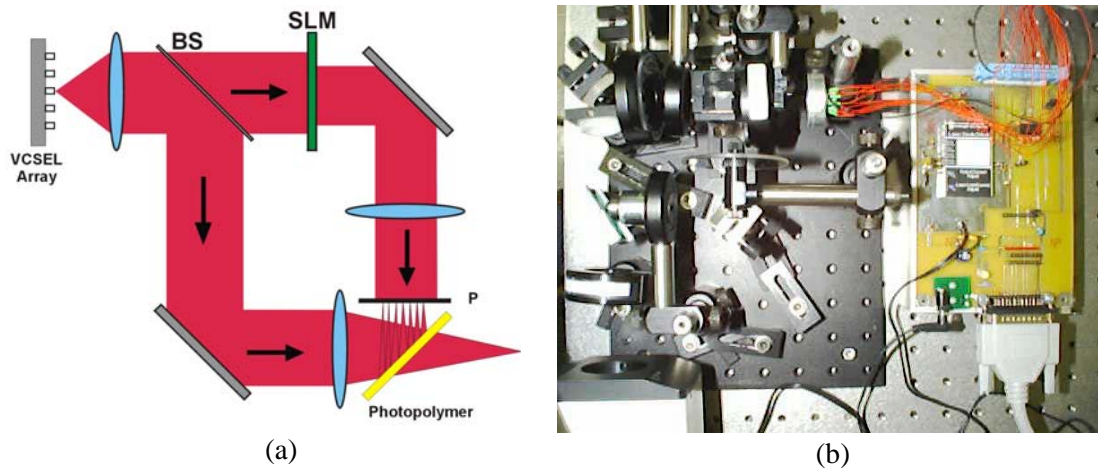
Fig. 1-8. (a) Schematic drawing of the recording setup for the OPGA, where BS is a beam splitter and SLM is a spatial light modulator, and (b) actual setup used in the experiments.

In the recording setup, as the schematic in Figure 1-8(a) shows, the beam emitted by the VCSELs is collimated by the first lens. Then a beam splitter (BS) creates the reference and signal beams. A SLM is used to transfer the information that needs to be stored in the memory into the signal beam. The SLM image is projected to plane P, where the photodetectors will be upon readout, by a lens. The lens on the reference arm focuses the reference beam creating a converging spherical beam used to record the hologram on the photopolymer. During readout the array of VCSELs should be placed on the plane where

the converging reference beam focuses, so that the diverging beam emitted by the VCSEL

creates the phase-conjugate reference that reads out the hologram.

Some experiments have been performed with this architecture to record and multi-

plex holograms in the memory, in this case a 100 μm thick film of Du Pont HRF700 pho-

topolymer. In the experimental setup, Figure 1-8(b), a single mask with a chessboard

pattern was used instead of the SLM and it was rotated to store different holograms. The

board on the right of the picture corresponds to the circuit to drive the array of VCSELs.

Figure 1-9 presents the reconstruction of two different pages. Since the VCSELs can be

switched on and off in less than a nanosecond, different pages can be retrieved in very short

time. This means that the OPGA module could switch rapidly among configuration con-

texts.

Hologram 1   Hologram 2
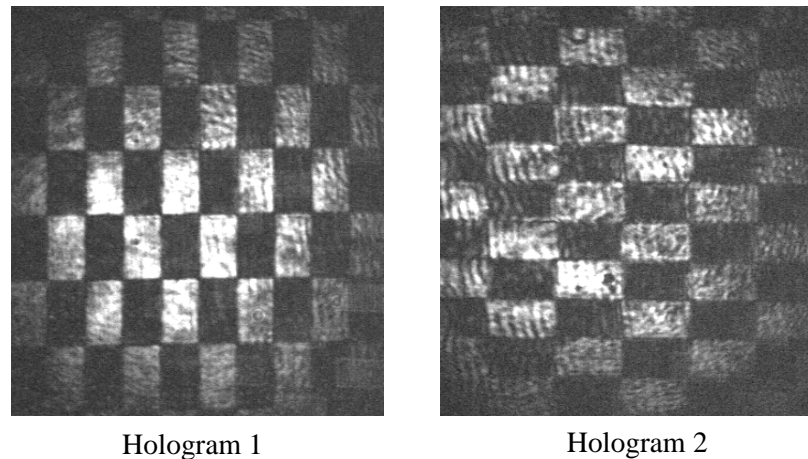
Fig. 1-9.   Detail of the reconstruction using VCSELs of two shift-multiplexed holograms in the transmission-geometry module.

A number of problems have been encountered in this architecture, not intrinsically

related to the architecture itself but to the VCSELs, which were not specially designed for

this application, and the medium used in the optical memory. The main problem, noticeable

14

in Figure 1-9, is that there is some crosstalk between holograms. The reason is that for the thickness of the medium, 100 μm, the shift selectivity of the memory is larger than the spacing between VCSELs (50 μm in particular for this array) and, consequently, Bragg-mismatch between neighboring holograms is not achieved. Placing the VCSELs much closer to the optical medium would narrow the shift selectivity of the memory. However, the small divergence angle of the VCSEL requires placing the array far enough as to overlap the entire footprint of the signal beam in order to record the hologram. Therefore, these two requirements turn out to be incompatible. Nevertheless, this limitation could be overcome by having a custom array of VCSELs with larger separation between elements and larger divergence angles. Another possibility would be to place a lenslet array on top of the VCSELs in order to increase their divergence angle.

Another issue is the quality of the reconstructed holograms. In this architecture, the spot of the signal beam on the material is relatively large, which makes the recording very sensitive to irregularities in the optical medium. However, a more serious issue is the power required per VCSEL to have short reconfiguration times in the OPGA. Since the 100 holographic pages are stored in a single location, the power requirement on each VCSEL becomes more demanding. If the target is to fully reconfigure the device in tens of μs, a straightforward calculation assuming a material with M/5 requires that each laser output a few mWatts. The characterization of the VCSEL arrays will reveal that a power requirement of 0.5 mW per element is more realistic.

1.4.2 Reflection-geometry OPGA module

Mostly due to the limitation in power, the architecture of the OPGA evolved towards a new design where the device could still have short reconfiguration times, in the range of tens of μs, but with a not so demanding requirement on the power per VCSEL. The technique used to store the holograms combines both spatial and shift multiplexing. The main difference with respect to the previous architecture is that upon recording, Figure 1-10, a lens focuses the beam before it impinges the SLM, as in a van der Lugt imag-
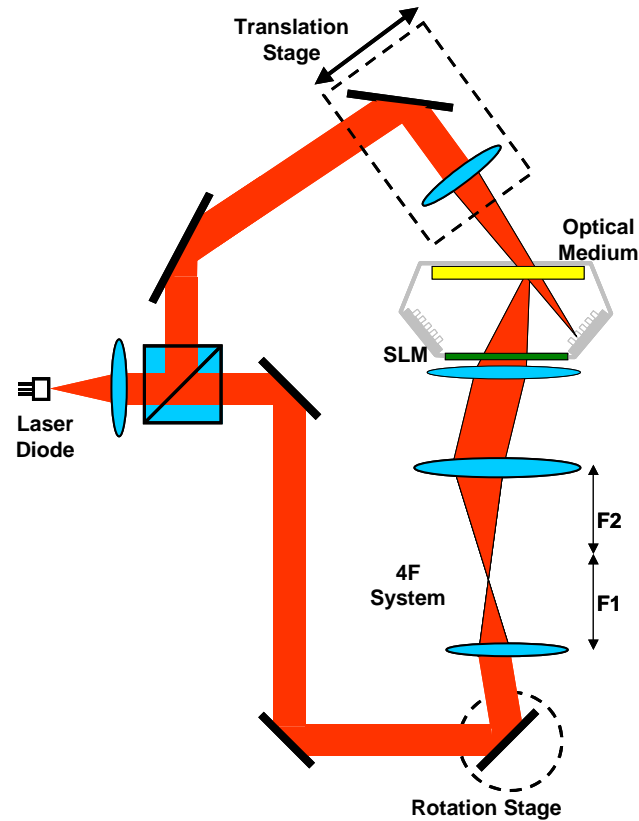
Fig. 1-10.   OPGA recorder setup. The linear translation stage in the reference arm, combined with the rotation stage and the lenses in the 4-F system in the signal arm, is used for the shift multiplexing of the holograms.

ing system [2], down to a small spot on the recording medium. By changing the angle of incidence of the beam on the lens, the signal spot focuses on a different location in the mate-

rial, which is partially overlapping with the previous ones. The pages of data are recorded in these partially overlapping circles that span a stripe on the optical material. To achieve Bragg mismatch among holograms, a converging reference beam needs to be shifted accordingly to illuminate the corresponding signal spot. In the recording setup, a laser diode with enough coherence length can be used instead of the VCSEL array. The beam emitted by the diode is collimated and splitted into the signal and reference arm. The signal beam passes through a rotation stage and a 4-F system that changes its angle before it illuminates the SLM. The reference beam is focused by a lens mounted on a mechanical scanner used to translate the beam beyond the shift-selectivity of the optical medium.
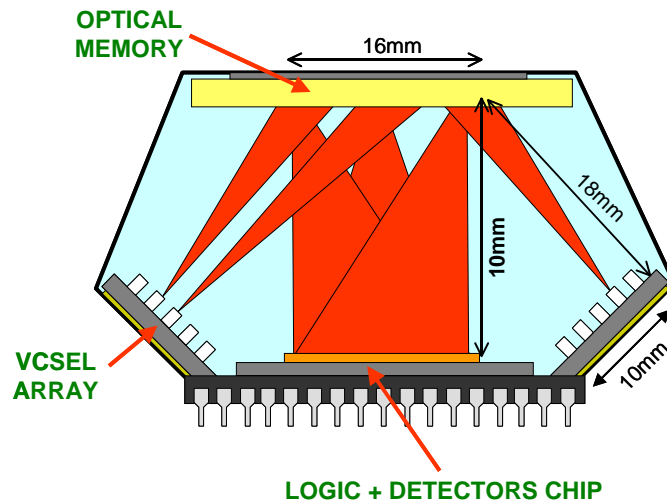
Fig. 1-11.   OPGA reader module. The light emitted by each VCSEL is used to read out a different hologram that self-focuses, due to phase-conjugation, on the array of detectors in the chip.

During readout, the system becomes very compact (Figure 1-11) for two reasons. First, the module uses reflection geometry for recording, so during readout the beam from the VCSEL and the array of photodetectors are both located on the same side of the material. Secondly, phase-conjugate readout makes unnecessary the use of any extra component. The VCSEL array is placed on the plane where the recording reference beams focus.

17

Thus, each VCSEL illuminates one of the spots in the memory and the reconstructed image back-propagates to the plane of the SLM where the photodetector array is located upon readout.
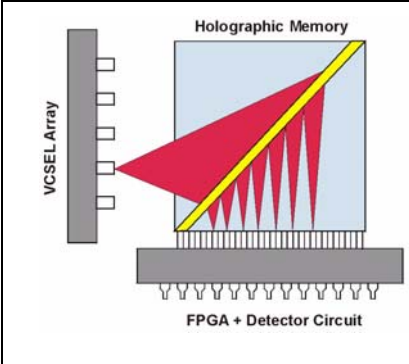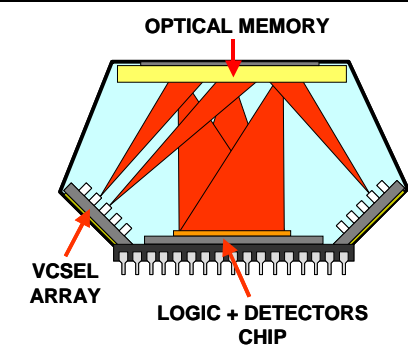
	Transmission OPGA module	Reflection OPGA module
Signal spot size on material (D)	$\sqrt{2}\left[Np + (\lambda/p)\dfrac{2d + Np(\lambda/p)}{1 - (\lambda/p)^2}\right]$	$\dfrac{2\lambda F}{p}$
Distance from VCSEL array (Z_o)	$D \cdot \left[\dfrac{\sin(\alpha)}{\sin(\theta + \alpha)} + \dfrac{\sin(\alpha)}{\sin(\theta - \alpha)}\right]^{-1}$	$D \cdot \left[\dfrac{\sin(\alpha)}{\sin(\theta + \alpha)} + \dfrac{\sin(\alpha)}{\sin(\theta - \alpha)}\right]^{-1}$
Shift selectivity (δ)	$\dfrac{\lambda Z_o}{2L\sin(\theta)}$	$\dfrac{\lambda Z_o}{L\sqrt{n^2 - \sin(\theta)^2}}$
Wavelength selectivity ($\Delta\lambda/\lambda$)	$\dfrac{\lambda\sqrt{n^2 - \sin(\theta)^2}}{2L\sin(\theta)^2}$	$\dfrac{\lambda}{L[n + \sin(\theta)]}$

Table 1-1. Summary of the expressions of system design features for the transmission- and reflection-geometry OPGA modules.

A benefit of this new architecture is that the diffraction efficiency per hologram now scales not as the total number of stored holograms but the number of overlapping ones at any location. Therefore, an important increase in diffracted power is obtained. Assuming that the same 100 configuration pages are stored in the M/5 material, but only 20 holograms overlap at any given location, then the diffraction efficiency per hologram is as high as 6.25%. The increase in diffracted power makes possible to achieve μsec-scale reconfigura-

tion times with only 0.5 mW of available power. A comparison of the main features between the transmission and the reflection modules is presented in Table 1-1, their relevance towards the design of the OPGA will be discussed in the following paragraphs. Table 1-2 provides the description of the system parameters and their values. They will help to illustrate the differences between the two proposed designs.

Parameter name	Symbol	Transmission OPGA system	Reflection OPGA system
Pixel size	p	5μm	
Data page format	N×N	1000×1000	
VCSEL wavelength	λ	680nm	
VCSEL divergence angle (half angle)	α	4.4^o	
Distance from recording plane (Fresnel hologram)	d	10mm	
Focal length of transforming lens (Fourier hologram)	F		10mm
Reference beam angle (w.r.t. material surface)	θ	45°	30°
Material thickness	L	200μm	

Table 1-2. Description of the parameters and values assumed for them in the comparison between the transmission- and reflection-geometry OPGA modules.

Besides relaxing the power requirement of the VCSELs, another benefit of the new architecture is that recording occurs at the Fourier plane, rather than in the Fresnel zone as in the original transmission module. In the transmission module, a 1000×1000 pixel hologram with 5 μm pixel-size placed at a distance of 10 mm from the recording plane would result in a footprint of 11 mm in diameter. On the other hand, for the reflection module, if the SLM is placed at the same distance from the recording material, and the lens that focuses the signal beam has a focal length of 10 mm, the signal spot size on the material will be just 2.7 mm in diameter. Given the smaller dimension of the area where the pages are recorded, the holograms are much less sensitive in the second case to any nonuniformity of the medium and, consequently, the quality of the reconstructed images is better.

The size of the signal spot on the recording plane has a major impact on the shift selectivity of the memory because the spherical reference beam emitted by the VCSEL must originate far enough to be able to completely overlap the signal spot on the material. For example, the large footprint in the transmission module, compounded with the low divergence angle of the VCSELs, makes necessary to position the VCSEL array at a distance of 51 mm, which in turn results in a shift selectivity of 122 μm. In the second design, the fact that the signal spot is smaller allows to position the VCSELs much closer to the medium (the minimum Z_o is 8.7 mm), lowering the shift selectivity to 21 μm.

Large shift selectivities are very undesirable. As δ increases, so does the spacing required between VCSELs in the array, which compromises their uniformity. One approach to narrow the shift selectivity is by increasing the thickness of the recording medium; however, this also narrows the tolerance of the holograms to differences between the nominal wavelength of emission of the array and the actual wavelength of each individual element. This can be observed in Figure 1-12, where the diffraction efficiency of the hologram is plotted as a function of the thickness of the material when the readout and recording wavelength differ by 0.17 nm, which corresponds to a dispersion of 0.05%. If we want to ensure that wavelength mismatch never accounts for more than 10% loss in diffraction efficiency, the thickness of the material should not exceed 250 μm. This shows that the thickness of the medium plays an important trade-off between shift-selectivity and dynamic range on one side (in which the larger, the better), and tolerance to wavelength mismatch on the other (in which the smaller, the better).

It is important to point out that the advantages of the second architecture over the first one originate not in that the former uses reflection geometry as opposed to transmis-
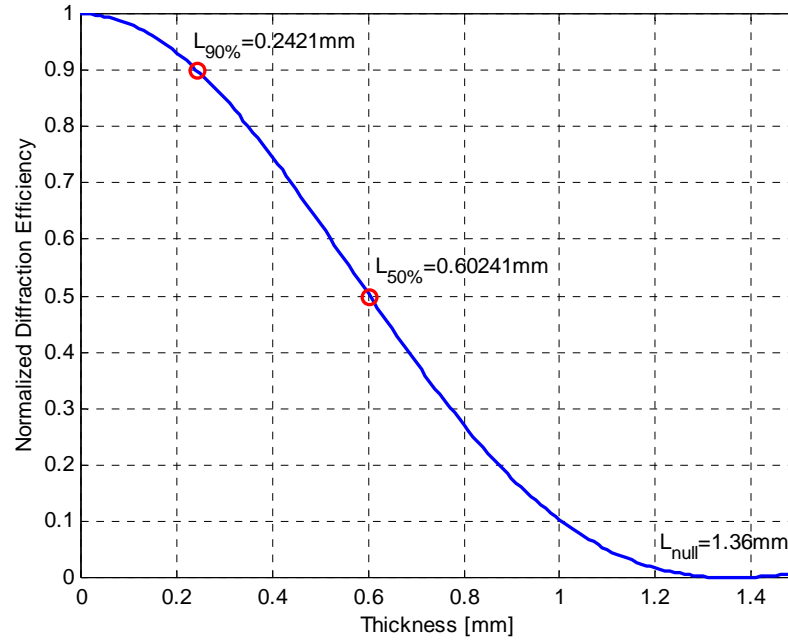
Fig. 1-12.   Diffraction efficiency as a function of the thickness of the material in the reflection-geometry OPGA module when the readout wavelength differs in 0.05% with respect to the wavelength used for recording.

sion geometry, but in the difference between Fourier-plane versus Fresnel-region recording. As a matter of fact, a transmission-type architecture using a van der Lugt imaging system is also possible. This case would be particularly interesting because the system would enjoy both small shift selectivity and, at the same time, broader wavelength selectivity than in a reflection module, which means more tolerance to wavelength nonuniformity.

References

[1-1] P. Stogiannos, A. Dollas, and V. Digalakis, "A configurable logic based architecture for real-time continuous speech recognition using hidden Markov models," *Journal of VLSI Signal Processing Systems for Signal Image and Video Technology* **24**, 223-240 (2000).

[1-2] A. Benedetti, and P. Perona, "Real-time 2-D feature detection on a reconfigurable computer", *Proceedings of the 1998 IEEE Conference on Computer Vision and Pattern Recognition*, Santa Barbara, 1998.

[1-3] J. Jean, X. J. Liang, B. Drozd, K. Tomko, and Y. Wang, "Automatic target recognition with dynamic reconfiguration," *Journal of VLSI Signal Processing Systems for Signal Image and Video Technology* **25**, 39-53 (2000).

[1-4] J. P. Kaps, and C. Paar, "Fast DES implementations for FPGAs and its application to a universal key-search machine," *Selected Areas in Cryptography Lecture Notes in Computer Science* **1556**, 234-247 (1999).

[1-5] S. D. Brown, R. J. Francis, J. Rose, and Z. G. Vranesic, *Field-Programmable Gate Arrays*, Kluwer Academic Publishers, Norwell, 1992.

[1-6] S. Trimberger, D. Carberry, A. Johnson, and J. Wong, "A time-multiplexed FPGA," *Proceedings of the IEEE Symposium on FPGA-Based Custom Computing Machines*, 34-40, IEEE Computer Society, Los Alamitos, 1997.

[1-7] M. Motomura, Y. Aimoto, A. Shibayama, Y. Yabe, and M. Yamashina, "An embedded DRAM-FPGA chip with instantaneous logic reconfiguration," *Proceedings of the IEEE Symposium on FPGAs for Custom Computing Machines*, 264-266, IEEE Computer Society, Los Alamitos, 1998.

[1-8] J. Mumbru, G. Zhou, S. Ay, X. An, G. Panotopoulos, F. Mok, and D. Psaltis, "Optically reconfigurable processors," *SPIE Critical Review 1999 Euro-American Workshop on Optoelectronic Information Processing* **74**, 265-288 (1999).

[1-9] T. H. Szymanski, M. Saint-Laurent, V. Tyan, A. Au, and B. Supmonchai, "Field-programmable logic devices with optical input-output," *Applied Optics* **39**, 721-732 (2000).

[1-10] D. Psaltis, M. Levene, A. Pu, G. Barbastathis, and K. Curtis, "Holographic storage using shift multiplexing," *Optics Letters* **20**, 782-784 (1995).

[1-11] G. Barbastathis, M. Levene, and D. Psaltis, "Shift multiplexing with spherical reference waves," *Applied Optics* **35**, 2403-2417 (1996).

[1-12] A. van der Lugt, "Packing density in holographic systems," *Applied Optics* **14**, 1081-1087 (1975).

2 OPGA elements and system integration

2.1 Introduction

After focusing on the system as a whole in the previous chapter, this chapter will look at each one of the elements of the OPGA separately. The following sections consider specific issues of the VCSEL array, the chip and the optical material, and the requirements they have to meet for their use in the OPGA system. Section 2.5 deals with the integration of the three components into a small package and presents a prototype for the OPGA that demonstrates, in a compact module, the operation of VCSELs as addressing devices to readout holograms from the optical memory. Finally, the integration between a holographic memory and a silicon chip is demonstrated in Section 2.6, where holograms are utilized to configure the logic in the chip.

2.2 Red VCSEL arrays

Vertical Cavity Surface Emitting Lasers (VCSELs) operating in the infrared wavelengths are widely used in optical fiber data links, optical interconnects, and storage applications. In contrast to conventional laser diodes, which emit light from the edge of the chip, VCSELs emit light vertically from the wafer surface. Therefore, instead of having to cleave the wafer into single elements, they can be packaged as large arrays [2-1]. The first VCSELs emitting in the red wavelengths were reported in 1993 [2-2]. The shift towards shorter wavelengths has opened the possibility of using such devices in holography, since most optical materials are sensitive in the visible range of the spectrum.

As described in Chapter 2, a VCSEL array can be used as addressing device in the OPGA module to selectively retrieve one data page from the optical memory. Section 2.2.1 describes the requirements the VCSEL array must meet, while Section 2.2.2 presents the results of the experimental characterization of arrays with different VCSEL sizes and element count that have been fabricated by Honeywell.

2.2.1 VCSEL requirements

The two most important parameters for the VCSELs, if they are to be used in the OPGA module, are their output power and wavelength uniformity across the array.

Consider first the wavelength uniformity: As seen in Section 2.4, the holograms are recorded in the memory of the OPGA module using a laser diode. However, they are read out with the VCSELs. Any difference between the recording and readout wavelengths will have a double effect on the reconstruction of the hologram: First, the amount of diffracted light will decrease due to Bragg-mismatch, making necessary longer detector integration times and therefore degrading the reconfiguration performance of the OPGA. Second, the reconstruction of the hologram will shift on the plane of the detector, resulting in pixel mis-registration and incorrect programming of the OPGA chip.

These two effects are depicted in the K-sphere diagram in Figure 2-1. A grating (vector $\mathbf{K_G}$) is recorded at wavelength λ (solid circumference) by the interference of the reference beam propagating at an angle θ with respect to the x-axis (vector $\mathbf{K_R}$) and the signal beam. If the hologram is now read out at a wavelength λ' (dashed circumference) by the beam $\mathbf{K'_R}$, the reconstructed signal beam will be Bragg-mismatched by an amount $\Delta \mathbf{K_Z}$ and propagate along $\mathbf{K'_S}$ at an angle α with respect the z-axis.

24
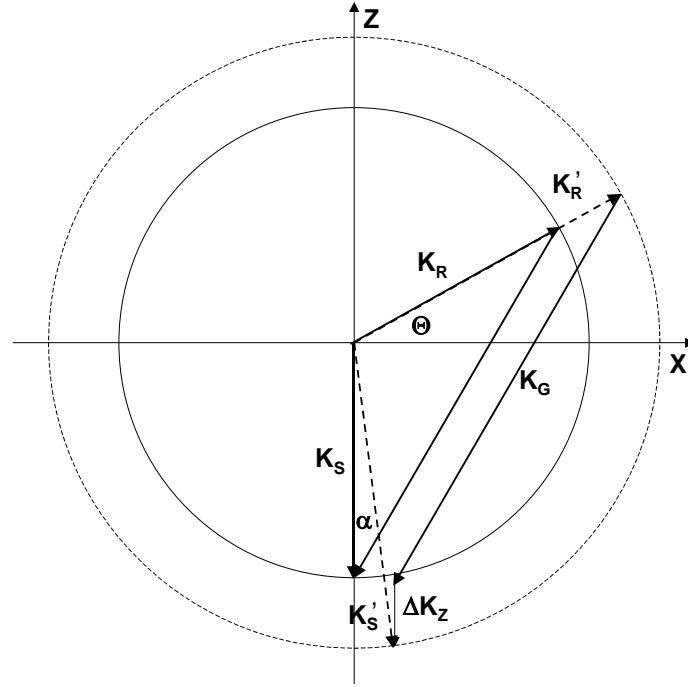
Fig. 2-1.   K-sphere diagram to illustrate the deviation angle α of the diffracted beam κ'_S when the grating is read out with a reference beam at wavelength λ' instead of λ.

According to the definition of angles in Figure 2-1, and assuming that the medium has a thickness L along the z-axis and is infinite in the transverse dimensions, the wavelength selectivity of the hologram can be readily calculated and is given by

$$\left(\frac{\Delta\lambda}{\lambda}\right) = \frac{\lambda}{L(1 + \sin\theta)},\qquad(2\text{-}1)$$

where $\Delta\lambda = \lambda - \lambda'$. Furthermore, if the detector plane is perpendicular to the z-axis and located at a distance D from the material, the amount of shift along the x-axis (δx) of the reconstructed hologram on the detector plane results in

$$\delta x = D\tan\alpha \approx D\left(\frac{\Delta\lambda}{\lambda}\right)\cos\theta.\qquad(2\text{-}2)$$

The approximately equal sign is due to $\tan\alpha \approx \sin\alpha \approx \alpha$, which is true only for small $\Delta\lambda$. Equation 2-2 can be rewritten in the form of a constraint on the ratio $\left(\frac{\Delta\lambda}{\lambda}\right)$ for a maximum

25

acceptable shift $(\delta x)_{max}$ that the system can tolerate without suffering from pixel misregistration

$$\left(\frac{\Delta\lambda}{\lambda}\right) \leq \frac{(\delta x)_{max}}{D\cos\theta}. \qquad (2\text{-}3)$$

In the context of the OPGA module ($\theta=30^{\mathrm{o}}$, D=10 mm, L=200 μm, and λ=680 nm) the condition in Equation 2-3 becomes more restrictive than the wavelength selectivity. To avoid a maximum shift larger than 20% of a 10 μm pixel detector, $(\delta x)_{max}=\pm2$ μm results in $\left(\frac{\Delta\lambda}{\lambda}\right) \leq \pm0.021$ %. Therefore the ratio of the difference between highest and lowest wavelengths across the VCSEL array, λ_H and λ_L, respectively, to the recording wavelength must satisfy $\left(\frac{\lambda_H - \lambda_L}{\lambda}\right) < 0.05$ %.

As far as the power requirement is concerned, the maximum optical power that the VCSEL can output has a direct impact in the reconfiguration time of the OPGA. It is important to point out that the VCSEL must operate in single mode. The presence of higher-order modes would degrade the quality of the reconstructed holograms as the wavefront of the beam emitted by the VCSEL would not match the wavefront of the laser diode used during recording.

The incident power required per VCSEL (P_{Inc}) depends on parameters of the holographic memory and the photodetectors. The former can be either related to the medium itself, like the dynamic range, or to the design of the optical memory, like the number of holograms sharing the same spatial location (M) and the number of pixels in each hologram ($N \times N$). Among the latter, there is the integration time of the detectors (T_{Int}) and the minimum number of photons for correct detection (#photons), which in turn is a function of the detector quantum efficiency and the threshold number of signal electrons required at the

26

detector. The required incident power can then be parametrized as a function of the integration time (OPGA reconfiguration time) and described by

$$P_{Inc} \geq (\#photons) \cdot \left(\frac{hc}{\lambda}\right) \cdot N^2 \cdot \left(\frac{M/\#}{M}\right)^{-2} \cdot \frac{1}{T_{Int}}. \qquad (2\text{-}4)$$

As described in Chapter 2, each location on the material contains only 20 holograms (M=20) of 1000×1000 pixels each ($N^2=10^6$). The number of photons required is a function of the integration time. As the integration time increases, the number of collected noise-electrons increases as well, and therefore more signal electrons (photons) are required for correct detection. Testing of the photodetectors has revealed that up to 50 µsec integration time, 2600 photons are required for correct detection [2-3].
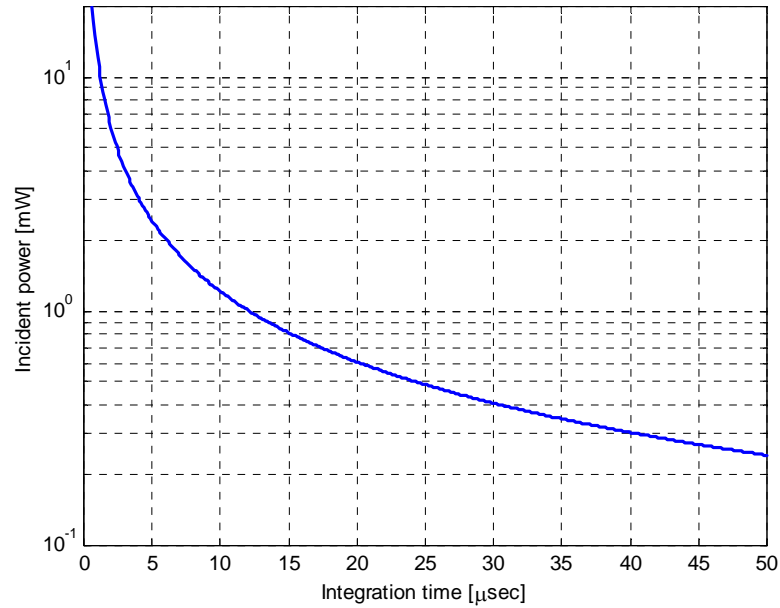
Fig. 2-2.   Minimum power emitted by the VCSEL for correct signal detection as a function of the integration time of the photodetectors.

The dependence between power and integration time described in Equation 2-4 is presented in Figure 2-2. As it can be observed, 25 µsec integration time can be attained if

27

each VCSEL is able to output 0.5 mW in single mode. Although shorter reconfiguration times could be achieved if the VCSEL was able to emit a few milli-Watts of power and, for example 5 mW in single-mode would make possible an integration time of just 2.5 µsec, the value of 0.5 mW per VCSEL will be taken as a more realistic power requirement.

2.2.2 Array characterization

Initial experiments to characterize red VCSELs and to verify the suitability of this type of laser diodes for applications in holographic systems were performed on a 4×4 symmetric array with a 50 µm spacing between elements.

The VCSELs operate in single mode and produce a spherical beam with a full divergence angle of 8.7°. When switching on the VCSELs, the rise time is less than 100 ps, which allows switching speeds over 1 GHz. Their output power is on the range of hundreds
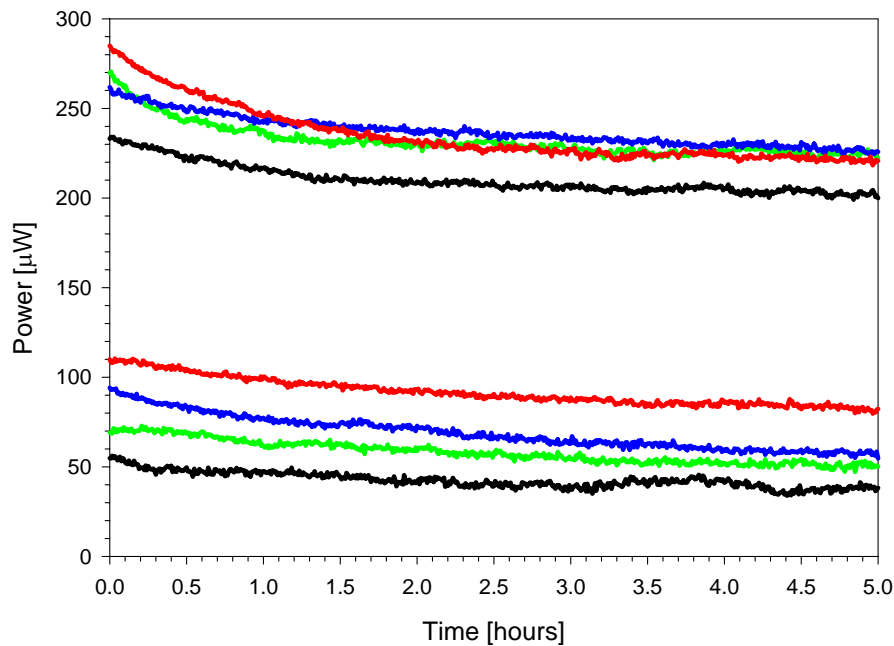
Fig. 2-3. Temporal evolution of the power emitted in continuous mode by the VCSELs over a period of five hours. Each curve correspond to a different element of the VCSEL array.

of μWatts, from 50 μW for the worst elements up to almost 300 μW for the best ones. The stability over time of the output power has also been studied. The power emitted by the VCSELs has been monitored over a period of 5 hours. Figure 2-3 shows the measurements for eight different elements in the array. As it can be observed, there is an initial drop in power due most probably to thermal heating of the P-N junction of the lasers. The long-term stability measured after a one hour warm-up over the last 4 hours results to be on average 18.6%, although in the worst case it is as large as 32.9%. A more realistic parameter is the short-term stability over a 15 minute interval after the initial warm-up, which turned out to be on average 4.8% and never larger than 9.2%.
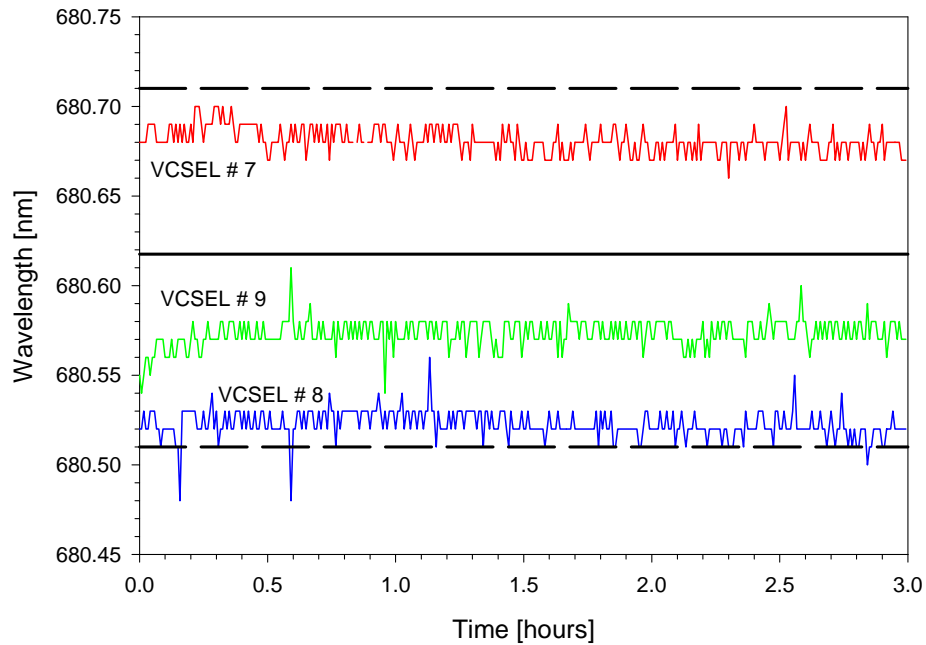
Fig. 2-4. Drift in wavelength of emission of the VCSELs monitored for a period of three hours. The solid line corresponds to the ensemble-averaged wavelength across the array, while the dashed lines indicate the maximum and minimum time-average wavelength for an individual laser.

The wavelength of all the operating devices in the array has been measured (Figure 2-4). The average wavelength across the entire array is 680.62 nm, with the highest and lowest wavelengths being 680.71 nm and 680.56 nm, respectively. This dispersion of values of just 0.15 nm across the array corresponds to a uniformity of 0.022%, in compliance with the specifications.

The fluctuation of the wavelength for individual elements with time has also been investigated, and it has been found to be smaller than 0.016%. This very good stability, even without any thermal control of the VCSEL, and a coherence length better than a meter, makes the VCSELs adequate to record and readout holograms, as shown in Figure 2-5.
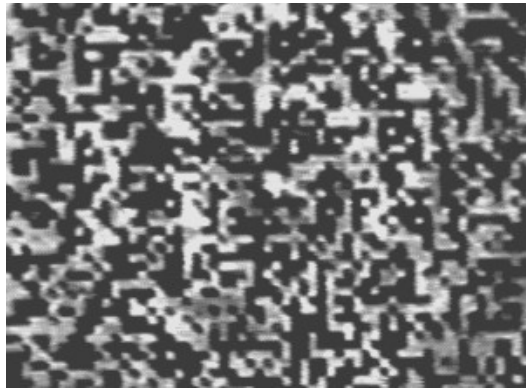
Fig. 2-5.   Hologram of a 34 μm pixel-size mask recorded on 100 μm thick Du Pont photopolymer using VCSELs.

The characterization of the 4 × 4 array revealed that, in order to use VCSELs in the OPGA module, the amount of optical power emitted by each device needed to be augmented and that the good wavelength uniformity in the small array might be difficult to preserve as the size of the array was increased. Both issues were taken into consideration when specifying larger arrays of 25 × 1 VCSELs. Figure 2-6 shows the die containing columns

of 25 VCSELs each, with a 100 µm pitch. The devices where fabricated in three different diameters: 20 µm, 15 µm, and 10 µm.
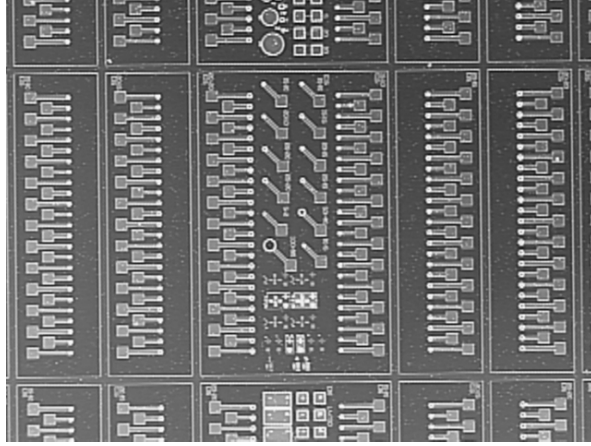
Fig. 2-6.   Picture of the die containing several 25×1 arrays of red VCSELs, arranged in columns. The devices are the small circles at the end of the square pads.

The optical power vs. current curve has been measured for the three sizes of devices. Figure 2-7 shows the typical results for a 10 µm, 15 µm and 20 µm cell. It was observed that as the size of the VCSEL is augmented, so are its threshold current and optical power. However, the device becomes multimode at lower levels of current. The 10 µm VCSEL could not produce more than 0.34 mW single-mode on average across the entire array. On the other hand, the 20 µm VCSEL becomes multimode slightly above its threshold current at 0.4mW, despite the fact that it can produce more than 1 mW. The 15 µm VCSEL turned out to be the one that is able to put out the highest power in single-mode, around 0.58 mW on average across the array, satisfying the power requirement for the OPGA module.

The wavelength stability of individual VCSELs was about 0.012%. As far as the wavelength uniformity across the 15µm-VCSEL array is concerned, the wavelength varies
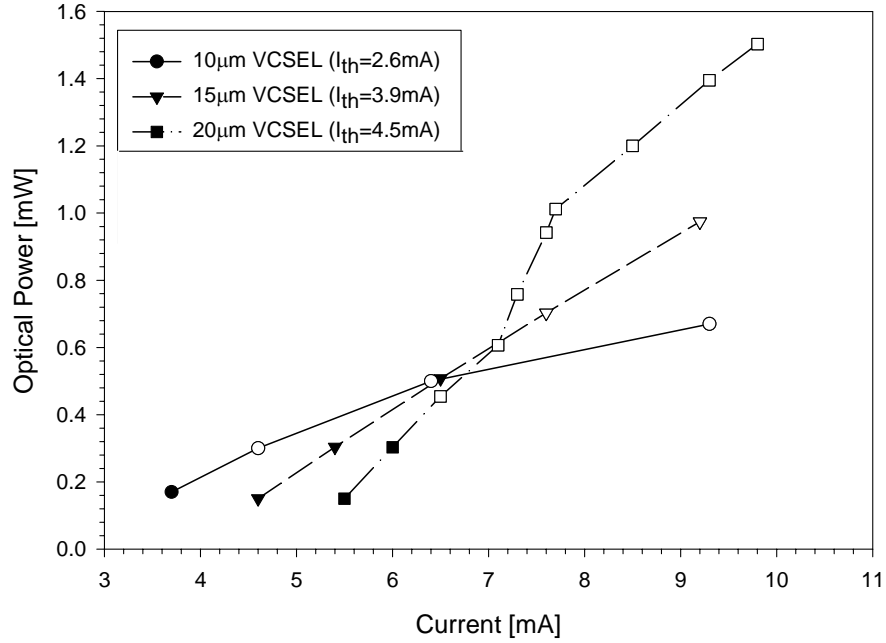
Fig. 2-7.   Typical Optical power vs. current characteristic curve for the 10 μm (circles), 15 μm (triangles) and 20 μm (squares) VCSEL. For each curve, the change from solid to clear markers indicates the transition in the VCSEL beam profile from single mode to multimode.

form 677.87 nm to 677.46 nm, being 677.65 nm the array-average wavelength. This results

in a uniformity of 0.06%.

2.2.3 Conclusions

Improvements in the fabrication process of the 25 × 1 arrays with respect to previous generations of devices have made possible to increase their output power and meet the

desired target of 0.5 mW single-mode. However, the wavelength uniformity has proved to

be difficult to preserve in larger arrays as the physical distance between VCSELs increases.

Despite the fact that Honeywell has been able to produce some arrays with a level of uni-

formity better than 0.05%, the consistency from die to die seems to still require further

research in the fabrication process.

The degradation of the wavelength uniformity as the size of the VCSEL array increases is the main cause that prevents VCSELs from being used as the addressing device in the OPGA system, and forces to consider other alternatives instead, like having a MEMS array of mirrors deflecting the beam of a single laser diode.

2.3 OPGA chip

The development of pixel sensors using standard CMOS technology [2-4], the same that is used for most microprocessors and memory modules, enables the integration of photodetectors with on-chip processing circuitry and has coined the expression "camera-on-a-chip" [2-5]. The OPGA chip makes use of the system-on-a-chip idea and integrates on the same die an array of pixels to detect the reconstructed holograms, as well as the logic circuitry of a conventional FPGA.

The photodetectors can be combined with the existing logic of the FPGA using either one of the two different topologies depicted in Figure 2-8: the detectors can be sparsely distributed across the whole chip interleaving them with the logic, or conversely, they can be laid out as a single large array on a specific region of the chip.

From the electronics point of view, the first topology is more convenient, because each pixel is detected exactly where it is needed to program the logic element. This makes unnecessary to distribute the detected signals all across the chip. However, from the optics side, to have detectors spread over the entire chip means that the quality of the reconstructed hologram must be uniform over a much larger area. Therefore, the second topology makes the optics simpler because the hologram needs to be uniform in a smaller region.

Logic Blocks   **Photodetectors**

(a)   (b)
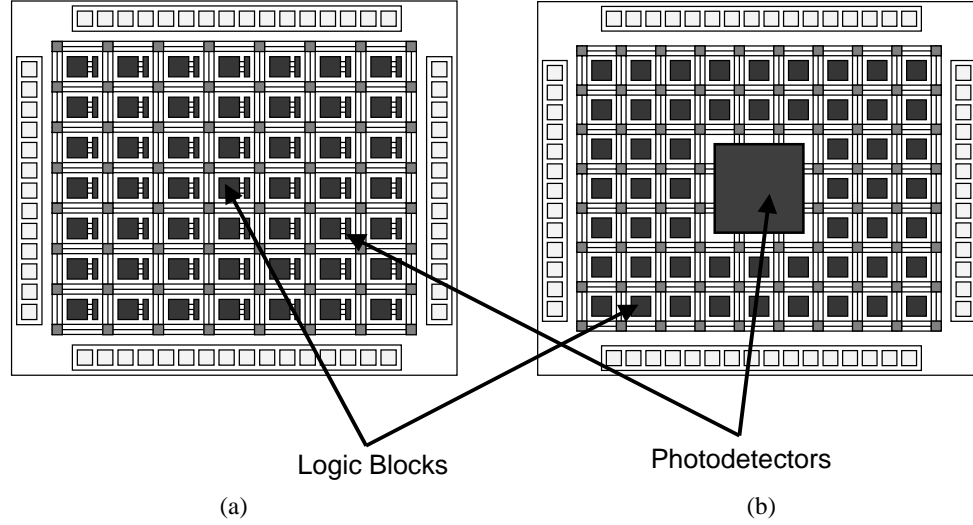
Fig. 2-8. Detector distribution on the OPGA chip: (a) Sparse, where the photodetectors are interleaved with the logic; or (b) Concentrated, where all the photodetectors are implemented as an array and detected signals need to be delivered to the programmable elements.

However, this comes at the price of having to implement a more complex mesh of buses to deliver the detected signals to the logic blocks.

Since each one of these topologies presents interesting aspects, both of them have been considered in the OPGA chips that have been designed and fabricated. In the first two generations of the chip, the photodetectors were arranged in small arrays and integrated into each logic block. However, the concentrated topology has been adopted in the final design because it simplifies the interface with a regular SLM.

2.3.1 Differential encoding

The light detected by each pixel needs to be converted into a logic value "1" or "0" by comparing its voltage to some threshold. The simplest way to perform such conversion is to set the same threshold to all the photodetectors in the chip. However, a global threshold cannot compensate for spatial variations of intensity across the entire data page. An alternative is to use different threshold levels across the area of the chip. This is not a perfect

34

solution either, even assuming that generating many different bias voltages for the thresholds is not an issue, because the spatial nonuniformity in the reconstructed hologram can change from one holographic page to another.

A very efficient way to be more robust to the intensity nonuniformity of the reconstructed data page is differential encoding [2-6], [2-7]. In this case, a pair of pixels in the hologram represents each single bit of information required to program the chip. The differential photodetector must have two photosensitive areas, referred to as the left and right pixels, which need to be matched to the pixel pair in the hologram. The logic "1" is then represented by left pixel ON and right pixel OFF and logic "0" by left pixel OFF and right pixel ON. This coding scheme makes it unnecessary to set any threshold for the photodetectors. Since the global variation of the incident illumination is reduced, the signal-to-noise ratio is increased and therefore the bit-error rate is improved. From the optics point of view, this type of data representation is simple and does not increase the system cost.

2.3.2 Photodetector structure

CMOS pixel sensors are based on either a passive or an active structure. Passive pixel sensors (PPS), depicted in Figure 2-9(a), consist of just a photosite that converts photons into electrons. The generated photocurrent discharges the reset voltage stored in the floating diffusion of the pixel. The analog pixel value is carried off the pixel to the support circuits that will amplify and digitize it. The simplicity in design of the passive pixel makes possible to dedicate most of the area of the pixel to the collection of light, obtaining high fill factors. However, this simplicity also makes the PPS more vulnerable to noise. On the other hand, active pixel sensors (APS), Figure 2-9(b), incorporate additional transistors
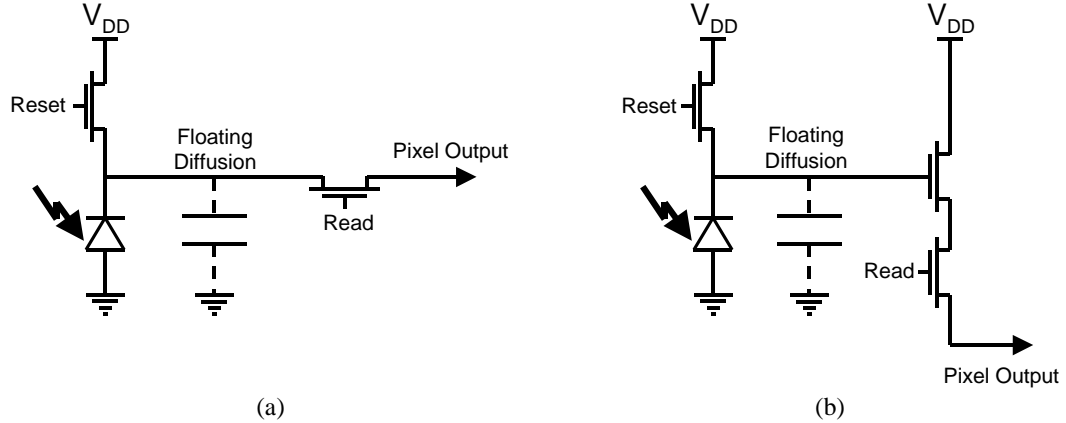
Fig. 2-9. Circuit schematic of (a) a passive pixel sensor, and (b) an active pixel sensor that includes a source-follower amplifier.

inside each pixel, like the source follower amplifier in Figure 2-9, to amplify the photo-generated signal and reduce noise. However, adding these components reduces the fill factor of the APS.

In the OPGA chip, the main two requirements on the photodetectors are their size and speed. The pixel sensors must have small pitch to result in a low overhead in silicon area. The smaller size of passive pixels makes them interesting for this application. But at the same time, the pixels must have enough sensitivity to guarantee a short integration time in the range of 1–100 μsec. This second requirement is better satisfied by active pixels, which reject better noise and crosstalk.

In order to find out which type of CMOS sensor is the most adequate for the OPGA application, and in particular to investigate the possibility of utilizing passive pixels, a first prototype chip has been designed and fabricated by Photobit using 0.35 μm CMOS process. The chip contains a 2×3 array of optically addressable logic blocks. The architecture of the logic block, Figure 2-10, is based on a 4-input 1-output LUT that can be programmed
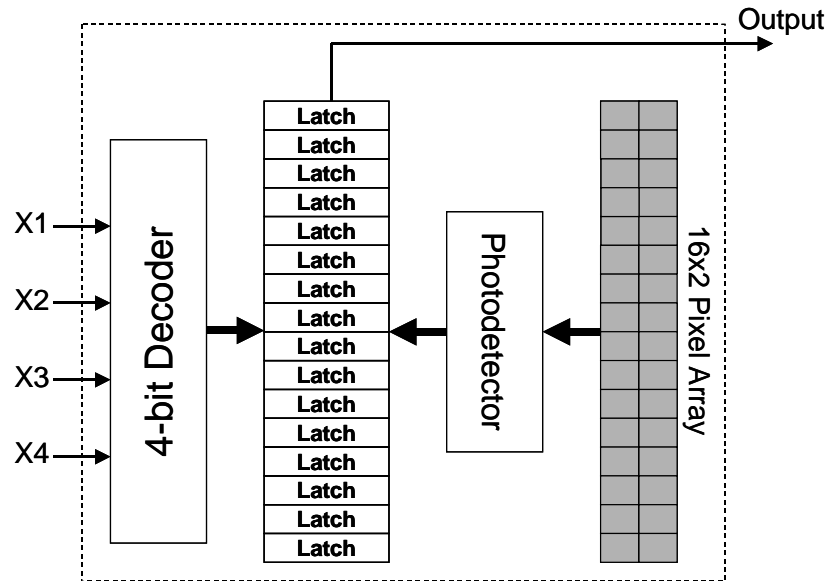
Fig. 2-10. Architecture of an optically addressable 4-input 1-output LUT. During the programming cycle, the array of 16 differential pixels time-share the photodetector. The detected bits are stored into the latches, and can be accessed during normal operation via the decoder.

by an array of l6 differential pixels with 5 μm pitch implemented inside the logic block. The areas of the OPGA chip that are not light sensitive have been shielded with metal to avoid stray radiation interfering with the logic circuit.

The optically addressable CLB in Figure 2-10 consists of a 4-bit decoder and a memory bank formed by an array of 16 latches to store the value of the computation, as in a conventional LUT; but dislike an "all-electronic" LUT, the logic block incorporates a 16×2 pixel array and a shared photodetector. The size of each CLB is about 125×85 μm, and the overhead due to optoelectronics is 24.8%. A detailed block diagram of the detection chain is provided in Figure 2-11. During the programming cycle, the photodetector will sequentially interrogate the 16 pixel pairs to read out the analog value in the left and right pixel of the pair. These voltages are taken to the first amplification stage, where a common source amplifier amplifies each channel separately before the signals are fed to the second

stage of the photodetector: a differential amplifier/comparator that produces the digitized

output that is delivered to the corresponding latch in the LUT.
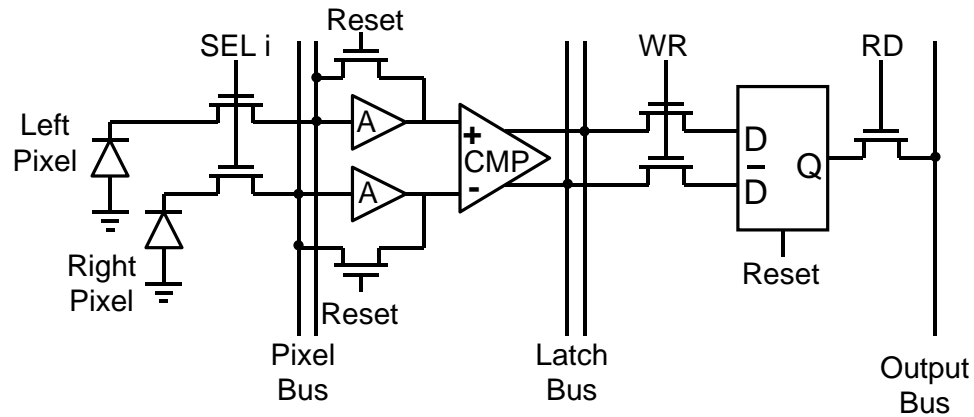
Fig. 2-11.   Block diagram of the detection chain. The first stage consists of two common source amplifiers (A) to amplify the value of each pixel in the pair separately. The second stage is a differential amplifier and comparator (CMP) that produces a 1-bit digitized output.

The preliminary testing of the passive-pixel chip showed satisfactory operation of

the logic blocks at low clock speeds around 60 KHz. The performance of the chip degrades

at higher clock speeds, as the electron injection noise in the pixel buses becomes more seri-

ous and leads to problems like blooming and crosstalk, which result in erroneous program-

ming of the LUTs. The lesson learned from the characterization of the first-generation chip

was that despite the potential savings in real estate obtained when using PPS, the chip

requires a higher level of noise suppression for high-speed operation only achievable with

the use of the APS. This is the reason why an active pixel solution was adopted for the

second and third generation chips, the latter also referred to as full OPGA chip and

described in the next section, also fabricated by Photobit.

2.3.3 Full OPGA chip design

The final version of the OPGA chip [2-3], Figure 2-12, mimics a small-scale FPGA. The chip combines a 64×32 array of differential APS sensors (the big block on the left in the picture); and the logic array (the small block on the right in the picture) containing the logic blocks and interconnecting resources.
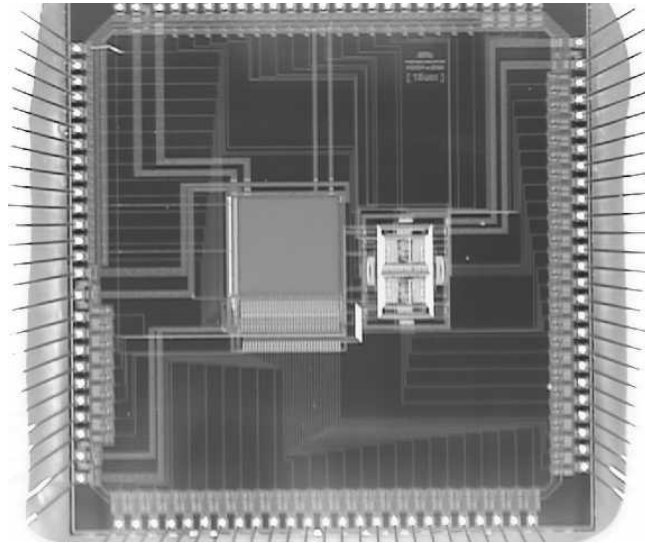
Fig. 2-12. The full OPGA chip, designed by Photobit in 0.35 µm standard CMOS process, integrates a 64×32 array of differential photodetectors (the large block on the left in the picture) and fully connected logic array (the small block on the right).

The programmable logic array contains four logic blocks in a 2×2 arrangement, and an interconnection network based on five crossbar switching matrices and four connection matrices, and four 5-bit tri-state I/O ports. A schematic of the logic array is provided in Figure 2-13. The architecture of the CLB is based on a 5-input LUT with 1-bit buffered output. The crossbar switching matrices (S-Boxes) allow for connectivity between two segments of bus lines or between the buses and the I/O ports. On the other hand, the connection matrices (C-boxes) establish connectivity between segments of bus and the inputs of the logic blocks.
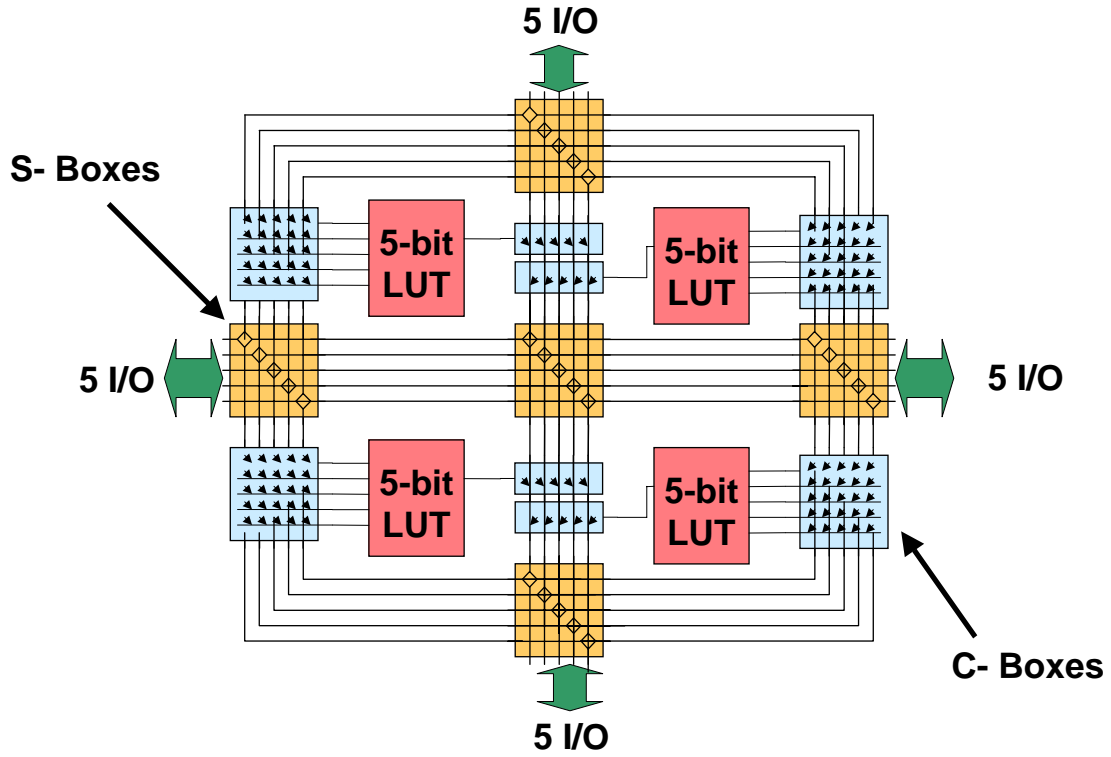
Fig. 2-13.   Schematic of the programmable logic array. The logic circuitry consists of a 2×2 array of 5-input LUTs with one buffered output each. The LUTs are fully interconnected by means of 5 switching matrices located in the center, left, right, top, and bottom of the array.

The APS array has been designed with pixel size of 15 μm. Although smaller sizes can be fabricated, the 15 μm sensor size has been selected to match the pixel size of the Kopin SLM that will be used to record the holograms in the optical memory. The detection process to read out the analog signal in each APS pair and convert it into a 1-bit digitized output is performed in parallel row-wise by an array of 32 detectors, physically located on the bottom of the APS array in Figure 2-12, and time-shared within each column of the APS array. The block diagram of the photodetector is essentially the same as the one depicted in Figure 2-11, with the difference that the passive sensors have been replaced by active ones.

Once a 32-bit control word has been detected, it can be used to program the on-chip logic. A total of 13 words, or equivalently rows of the APS array, are necessary to configure

40

the entire logic of the OPGA, therefore 4 different configurations can be downloaded simultaneously into the chip. This feature makes it possible to switch between configuration contexts within the same hologram and implement partial reconfiguration of the OPGA chip.

2.4 Optical materials

After deciding upon the mechanism to store the configuration templates in the holographic memory of the OPGA, it is not less important to consider which optical media are appropriate for the OPGA system. One of the basic requirements on the optical material is its M/#. The medium must have enough dynamic range to support 100 holographic reconfiguration templates. As discussed in Section 2.4, a material with at least M/5 would be desirable. It is worth making the remark that this M/# must be achieved not just for plane wave holograms but for high-bandwidth data pages as well. In general, thicker media are preferred because they offer larger dynamic range and better selectivity, which allows for more dense multiplexing. However, in this particular application, a too thick material would result in a very narrow wavelength selectivity, making even more stringent the requirement in wavelength uniformity of the VCSEL array.

In order to make possible the recording of high-bandwidth data pages, the holographic material should exhibit very good optical quality and uniformity, low scattering and not undergo significant dimensional changes during recording, like shrinkage in certain photopolymers. Finally, the material should also have a broad modulation transfer function (MTF) to provide enough flexibility to work in both transmission and reflection geometries.

Since the optical memory in the OPGA is intended to operate in a read-only mode, many different polymer-based materials can be used. In these media, readout of the stored data does not result in erasure, therefore, the lifetime of the holograms is only limited by the aging of the polymer itself. Holographic polymers are interesting because they exhibit very good dynamic range and also have high sensitivity. For example, Du Pont photopolymer has been used in early experiments in the OPGA, as well as in the system demonstration described in Section 2.6. However, this polymer suffers from shrinkage and poor optical quality due to nonuniformity of the material, which distorts the reconstructed images. This problem becomes more important as the pixel size is reduced, even if phase-conjugate readout is used. Therefore, Du Pont photopolymer is not the best option for a full scale system. Another alternative that has been considered is a red-sensitive acrylamide-based PVA material (see Section 2.4.1). This medium is fairly similar to Du Pont photopolymer and in fact suffers from many of the same problems as the Du Pont films.

The possibility of using PQ-doped PMMA has also been explored. This material shows good optical quality and M/# [2-8], but it has extremely poor absorption in the red, making necessary to use green wavelength laser sources in the OPGA module. A full description of the mechanism of grating formation in PQ-PMMA, along with experiments to optimize the performance of the material, are provided in Chapter 5. Nevertheless, the most solid choice seems to be the Aprilis film [2-9]-[2-11], since it enjoys both good recording dynamics and high optical quality. Chapter 4 presents the experimental characterization of the material and its use in holographic data storage applications.

A list of optical materials would not be complete without taking into consideration the photorefractive crystals. Iron-doped lithium niobate crystals are another good option for

the OPGA (see Section 2.4.2), and an advance packaging design that uses a $LiNbO_3$ crystal is described in Section 2.5 and has been demonstrated in [2-12]. The volatility of the stored information during readout, or even in the dark, has been traditionally seen as a drawback in this class of materials, however, recent research has successfully developed nonvolatile re-writable memories using doubly doped crystals [2-13], [2-14].

	Du Pont	Aprilis	$LiNbO_3$:Fe	MB-PVA	PQ-PMMA
Thickness	20-100 μm	200-500 μm	cm	80 μm	1-10 mm
M/#[*]	4.5 (100 μm)	10 (200 μm)	5 (8 mm)	1 (80 μm)	4.8 (3 mm)
Sensitivity: 1% energy Saturation	~1 mJ/cm^2 300 mJ/cm^2	1 mJ/cm^2 300 mJ/cm^2	>100 mJ/cm^2 N/A	20 mJ/cm^2 40 mJ/cm^2	12 mJ/cm^2 ~1 J/cm^2
Scattering	5×10^{-4}/strad	10^{-5}/strad	10^{-6}/strad	~ Du Pont	10^{-4}/strad
Optical Quality	Good	Very good	Excellent	Good	Very good
MTF	Good	0.2-10 μm	Good	--	Good
Shrinkage	~3.5%	~0.05%	N/A	~ Du Pont	N/A
Post-processing	Curing	Curing	N/A	--	Baking
Volatility	No	No	Yes w/o fixing	No	No
Lifetime: Shelf life Data retention	Months Years	Months >10 years	Years Years	-- --	Years Years

Table 2-1. Comparison of the main properties of available holographic materials that have been considered for the OPGA. (*M/# measured for the actual thickness of the material)

Before presenting the experimental characterization of each one of the materials and discussing of their particularities, Table 2-1 provides a comparative overview of the main properties of the different holographic media that have been considered for the OPGA module.

2.4.1 MB-doped acrylamide-based PVA polymer

The repertory of red-sensitive holographic media has been increased with the development of an acrylamide in polyvinyl alcohol (PVA) photopolymer film. The use of acry-

lamide material for holography was first published in [2-15]. High diffraction efficiency holograms using acrylamide in PVA solution films were reported in [2-16]. This particular material is doped with 3,7-bis(dimethylamino)phenothiazin-5-ium chloride, usually called methylene blue (MB), which is a chromophore sensitive to red wavelengths.

Films of MB-PVA polymer have been synthesized to characterize its performance. Sample preparation consists of dissolving the acrylamide, along with the MB dye and a polymerization initiator, triethanolamine, in an aqueous solution with 10% wt of PVA. The concentrations of monomer, dye and initiator were chosen to match the values for material optimization published in [2-17] and summarized in Table 2-2. The solution was poured onto glass plates and let dry in the dark to obtain films of 80 μm in thickness.

Component	Concentration
Acrylamide	3.4×10^{-1} M
Triethanolamine	2.0×10^{-1} M
Methylene blue	2.4×10^{-4} M

Table 2-2. Concentrations of the optimal composition of the photosensitive PVA solution. Concentrations are in Molar (i.e., Mol/l)

The absorption spectrum of one of the samples, Figure 2-14, shows that the material is highly absorptive in the region of the red wavelengths, resulting in an optical density of 1.17 for an 80 μm thick film at 633 nm.

The photochemistry of this material is fairly similar to the one of Du Pont polymer. Exposure of the sample to red light excites the dye molecules, which in turn activate the molecules of the initiator, triggering the free-radical polymerization of the acrylamide. Holographic recording is achieved by illuminating the sample with an interference pattern. The photoinduced polymerization of the acrylamide in the bright fringes, combined with
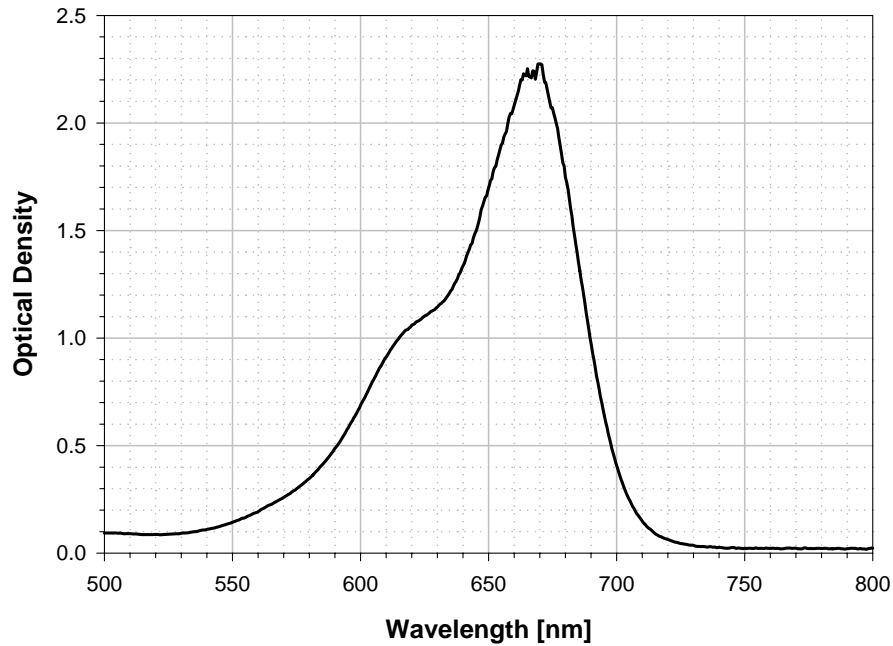
Fig. 2-14.   Absorption spectrum of an 80 μm thick MB-PVA film.

the diffusion of the monomer from the dark into the bright regions, results in significant local changes of the index of refraction.

Recording experiments on this material have been performed using a He-Ne laser in a symmetric transmission-geometry setup. The angle of incidence of each one of the beams (outside the material) is 30° with respect to the surface normal of the sample. The growth of the hologram to saturation is plotted in Figure 2-15. The recording curves saturate after 250 mJ/cm^2 of exposure, achieving a level of diffraction efficiency about 35%. The square root of these curves has been fitted to saturating mono-exponentials to determine the recording "time" constant. This constant resulted to be 99.5 mJ/cm^2 on average, which corresponds to a sensitivity of 791 cm/J.

The material seems to require about 10 mJ/cm^2 of pre-exposure energy before there is any growth in the diffraction efficiency of the hologram. This agrees well with the results
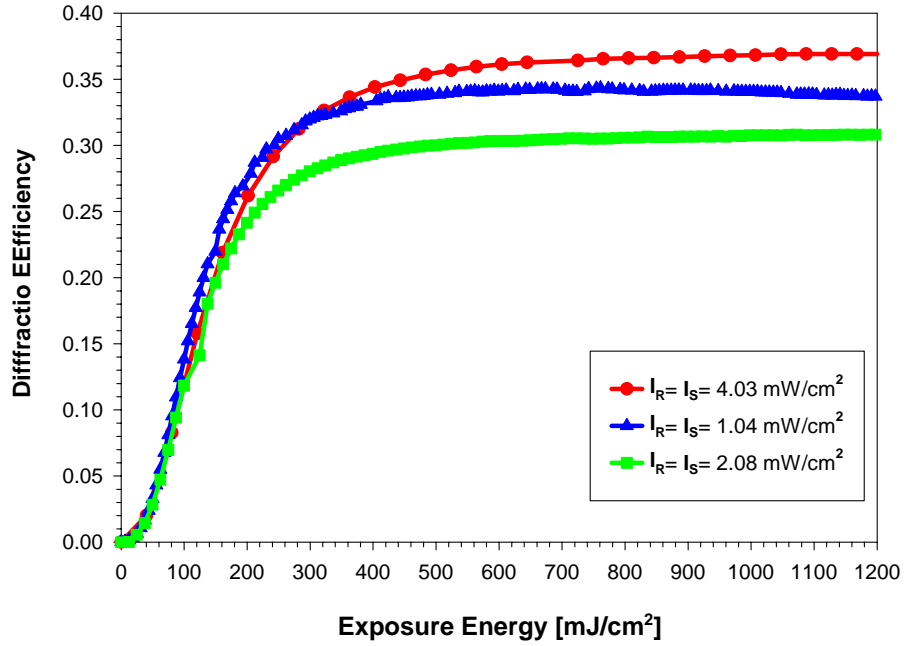
Fig. 2-15.   Hologram diffraction efficiency as a function of the recording exposure energy.

from the multiplexing experiments in which the early holograms are consistently weaker, like the first two holograms in Figure 2-18(a) and Figure 2-19.

The recorded holograms presented good quality and rendered nice selectivity curves, like the one presented in Figure 2-16. The measured angular selectivity turned out to be 0.74^o (outside the material). This very wide angular selectivity is fully consistent with the 80 μm thickness of the samples.

Multiplexing experiments have been performed in order to measure the M/# of the material. The small thickness of samples, which results in large angular selectivity, greatly limits the number of holograms that can be angularly multiplexed. Alternatively, peristrophic multiplexing [2-18] can accommodate more easily a larger number of co-located holograms. The sample is mounted on a rotation stage in the experimental setup, so it can be rotated around the normal to its surface between successive exposures. As the

46
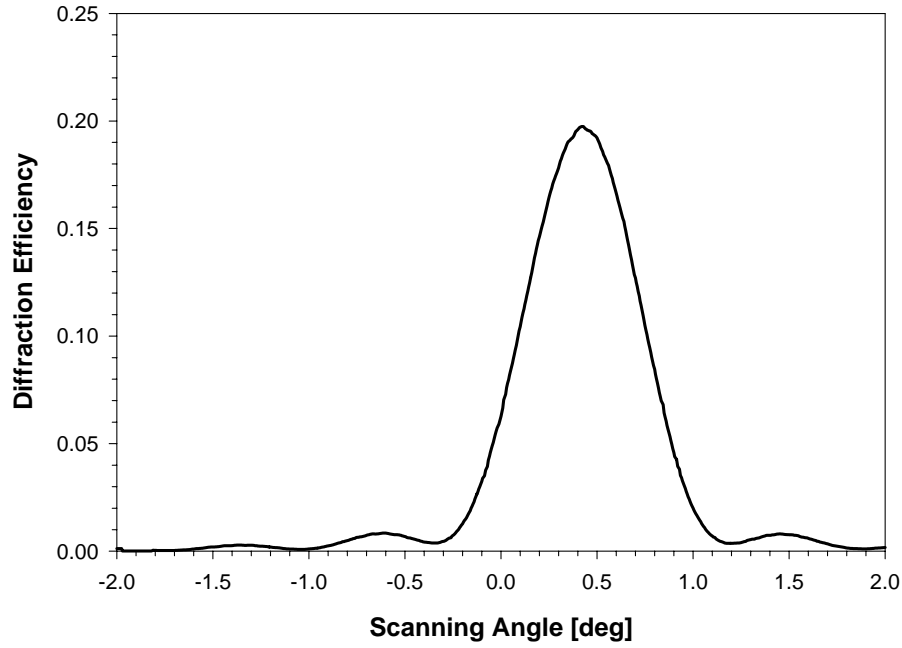
Fig. 2-16.   Angular selectivity curve for a hologram recorded in an 80 μm thick MB-PVA film.

sample rotates, the direction of propagation of the diffracted wave changes, which can then

be filtered off the detector, making it possible to record a new hologram without having

crosstalk from the previous one. In general the sample can be rotated 360°, however the

degeneracy of the symmetric recording geometry reduces that range to just 180°.

Figure 2-17(a) plots the diffraction efficiencies of 31 multiplexed holograms. Each

recording beam had 1.04 mW/cm^2 in intensity and a 7 mm diameter. The exposure energy

was 17 mJ/cm^2 for all the holograms, ensuring that the dynamic range of the sample is used

up after approximately 530 mJ/cm^2. The cumulative grating strength of the holograms is

then computed in Figure 2-17(b). The M/# can be estimated from the saturation value of

this curve, being M/0.91 for the actual thickness of the material.

The M/# can be optimized by equalizing the strengths of the holograms using a

recording schedule. A schedule was calculated by fitting a sixth order polynomial to the
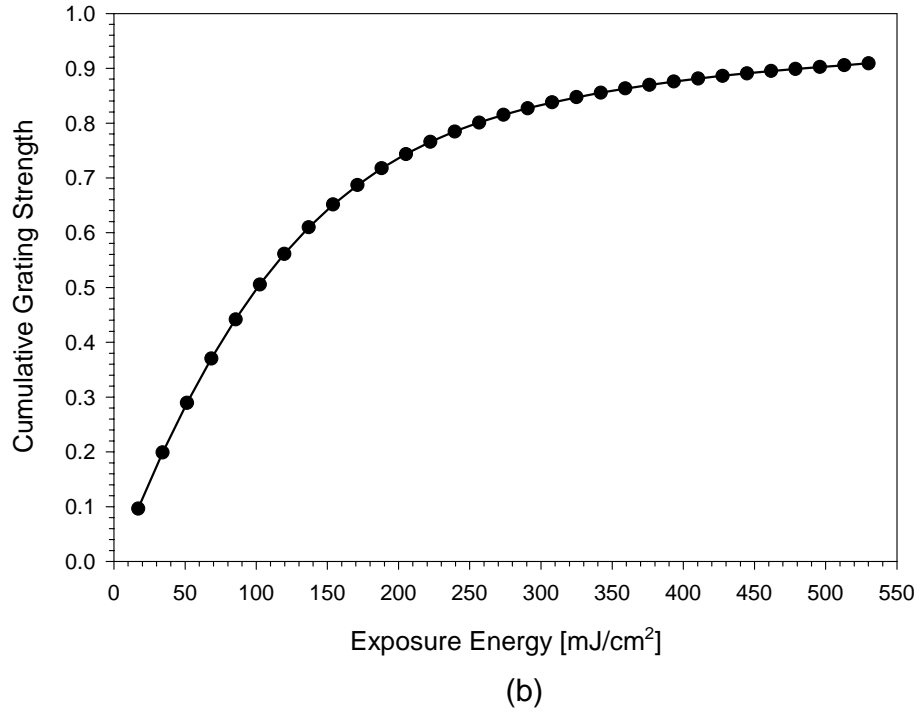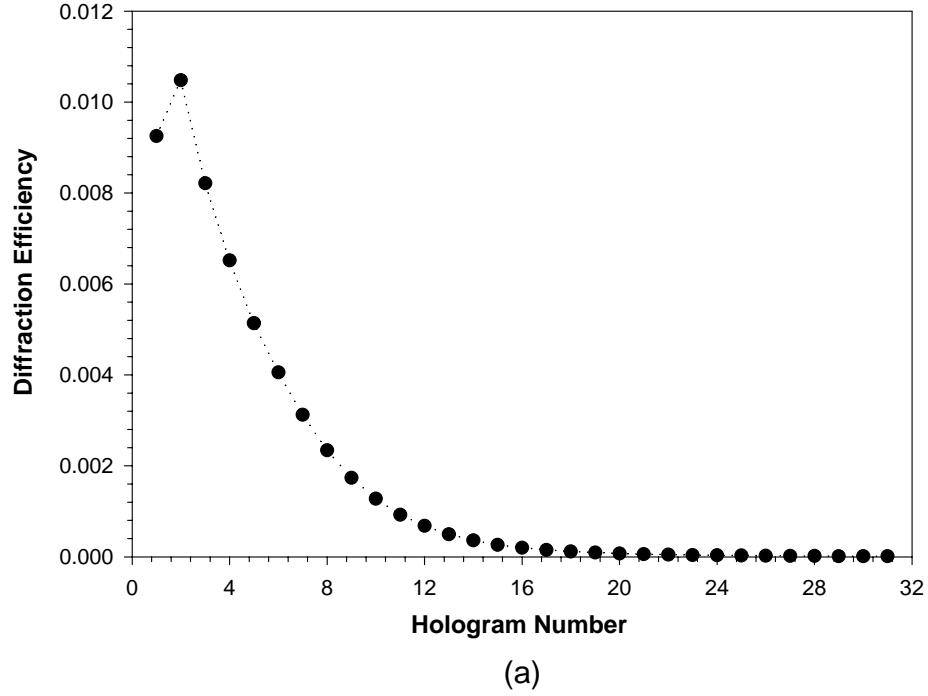
Fig. 2-17.   (a) Individual hologram strengths of 31 holograms multiplexed with equal exposures, and (b) their cumulative grating strength. The solid line in (b) is a sixth order polynomial fit.

experimental data in Figure 2-17(b) according to the method described in [2-19]. The

scheduled recording experiment produced more equal holograms, Figure 2-18(a), with an

average diffraction efficiency $\eta = 9.6 \times 10^{-4}$. The cumulative grating strength curve in Figure 2-18(b) saturated at M/0.94, which is slightly higher than in the previous case for constant exposure.

The optimization process can be iteratively refined by computing a new recording schedule for the next iteration based on the results from the previous one. As the holograms become more equalized, the cumulative grating strength should saturate at a higher value, indicating that the dynamic range of the material is used more efficiently. Although better equalization has been achieved in the experiments, Figure 2-19, it has not necessarily been coupled to higher M/# (M/0.81 in Figure 2-19, with an average $\eta = 7.5 \times 10^{-4}$). This is most probably due to differences in the thickness of the samples

The material presents a good M/# for its small thickness. Further multiplexing experiments produced a maximum M/# of 1.3. However, the large absorption of the material at 633 nm leaves little room to increase the dynamic range by making thicker samples. The consistency of the results throughout different experiments was poor due to sample-to-sample variance. Further development of the MB-PVA material is necessary if this material is to be used for holographic data storage applications, like in the OPGA system.

Another aspect that needs consideration is the image quality of the reconstructed holograms. Shrinkage during recording is expected in this material due to the process of polymerization induced by illumination with the laser beam. In that sense, the fact that the angle of incidence of the probing beam needed to be detuned to Bragg-match the hologram in Figure 2-16 is an indication of the presence of shrinkage. Other issues like material uni-
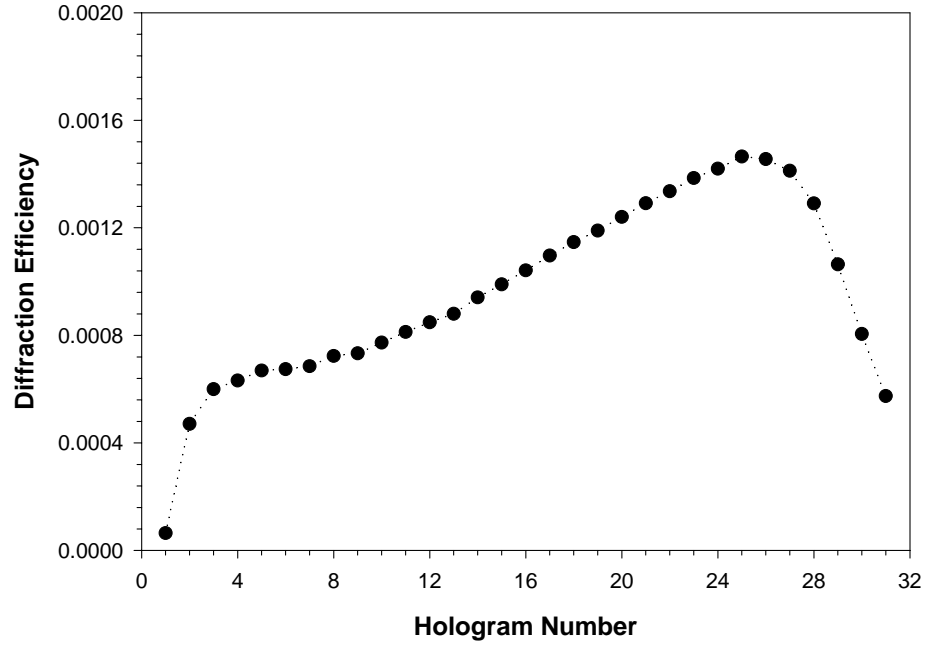
(a)
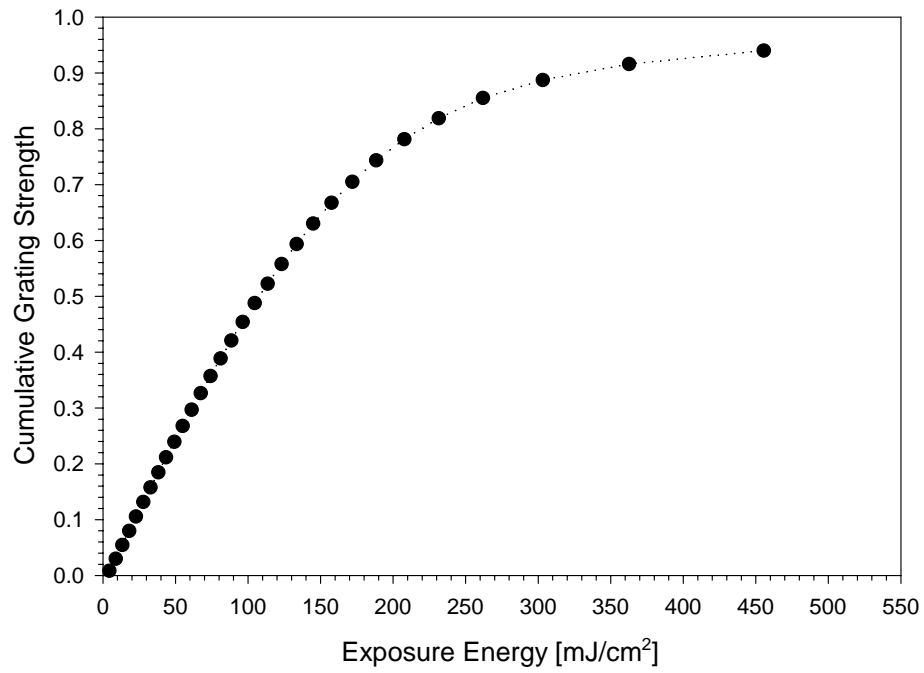
(b)

Fig. 2-18.   (a) Individual strengths of 31 multiplexed holograms recorded with an exposure schedule and (b) their cumulative grating strength.
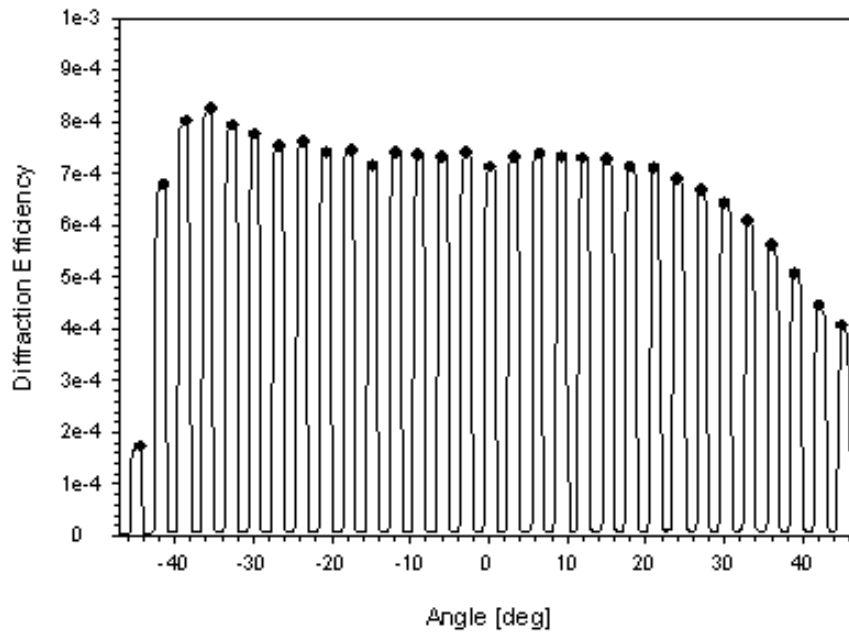
Fig. 2-19.　Comb function of 31 peristrophically multiplexed holograms recorded with exposure schedule.

formity and scattering were not investigated, although no significant improvements with respect to Du Pont photopolymer are expected.

2.4.2 Lithium niobate crystals

Photorefractive crystals have been widely used as support for holographic data storage applications [2-20], [2-21]. Unlike the other materials compared in Table 2-1, hologram formation in $LiNbO_3$ is achieved by means of the photorefractive effect. During recording, the interference pattern of two light beams excites electrons in the bright fringes into the conduction band of the crystal. At the end of their lifetime, the excited electrons return to either the valence band or to centers in the bandgap created by dopants like iron, where they can be promoted again into the conduction band. However, the electrons that recombined into centers in the dark fringes of the interference pattern can no longer be excited and remain trapped. The redistribution of charges in the crystal, and their eventual

51

trapping, builds a spatially variant electric field that induces in turn the modulation of the refractive index of the crystal through the electro-optic effect, known as Pockel's effect. Of course, the process of index modulation is reversible, so uniform illumination will erase any local distribution of electric charges.

The recording sensitivity in $LiNbO_3$ crystals is between one and two orders of magnitude lower than in photopolymers, making the recording process more slowly. However, this is relatively unimportant in the context of the OPGA, because the OPGA module is intended to operate as a read-only memory and therefore the recording of the holographic configuration templates occurs off-line. Furthermore, unlike photopolymers, $LiNbO_3$ crystals offer the possibility of implementing a fully read-write module. A holographic RAM type of memory [2-22] makes it possible to update the set of configuration templates that the OPGA chip can access at any particular time, giving a higher level of flexibility to the OPGA system.

Although a comprehensive characterization of $LiNbO_3$:Fe is beyond the scope of this section, experiments have been performed using Fe-doped crystals in the reflection geometry for red wavelengths to verify that their performance meets the requirements for this particular application. The experimental setup is a symmetric reflection-geometry system in which each recording beam impinges the crystal at an angle of 10° (outside the medium) and has an intensity of 4.03 mW/cm^2.

Among the z-cut $LiNbO_3$ crystals available in the laboratory, the best results have been obtained in an 8 mm thick crystal with 0.02% wt Fe that was reduced in order to increase its absorption at 633 nm. The evolution of a grating in that crystal is monitored in

Figure 2-20, in which the hologram is recorded for 30 minutes, growing up to 4.8% in diffraction efficiency. The square root of the rising edge of the curve has been fitted to a line and the sensitivity of the crystal has been estimated to be 0.031 cm/J. The hologram is then exposed to non-Bragg-matched uniform illumination for an interval of 6 hours to study the erasure dynamics. This portion of the curve has been fitted to a monoexponential, resulting in an erasure time constant (τ_e) of 29304 sec.
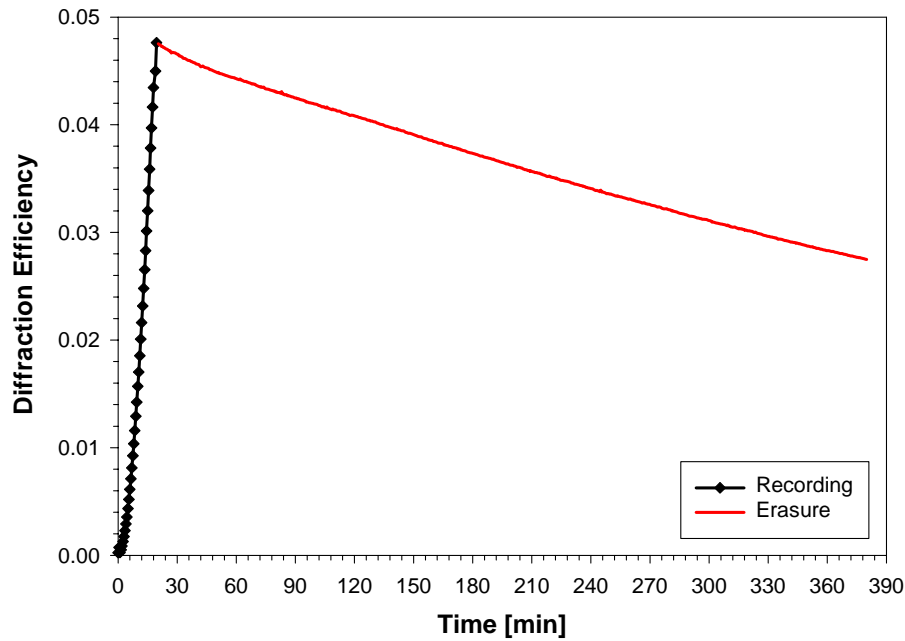
Fig. 2-20.   Recording and Bragg-mismatched erasure curves at 633 nm for an 8 mm thick z-cut LiNbO$_3$:Fe 0.02% wt crystal.

In photorefractive materials, the dynamic range is directly related to the asymmetry between the recording and erasure rates. The recording process follows an exponential growth to saturation (A$_o$) with recording time constant τ_w. The M/# is obtained as the product of the recording slope at the origin and the erasure time constant [2-23]:

$$M/\# = \frac{A_0}{\tau_w} \cdot \tau_e, \qquad (2\text{-}5)$$

53

resulting in M/5.8 for the thickness of this particular LiNbO$_3$ crystal.
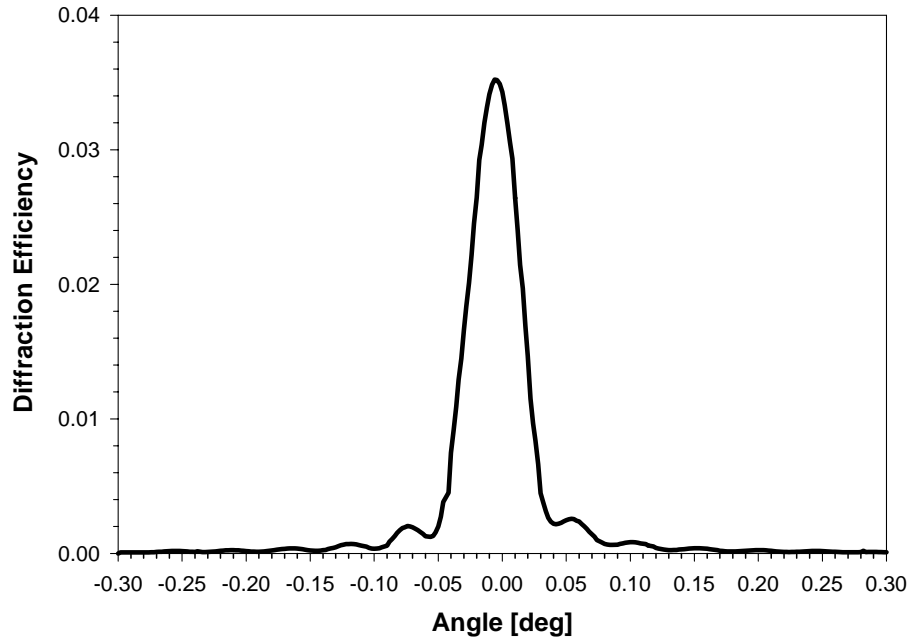
Fig. 2-21.   Angle selectivity curve of a hologram in an 8 mm thick crystal.

An alternative way to measure the dynamic range, also less subject to errors due to the estimation of the recording and erasure time constants, is by multiplexing several holograms at the same location. To minimize crosstalk between neighbor holograms, the angular separation between them was chosen to be 0.15^o, which corresponds to the third null of the selectivity curve shown in Figure 2-21. The results of two different experiments, in which 41 and 101 holograms were angularly multiplexed, are presented in Figure 2-22.

The holograms have been equalized using a recording schedule computed as explained in [3], and according to which the recording time for the mth hologram (t_m) is given by the following expression:

(a)

(b)
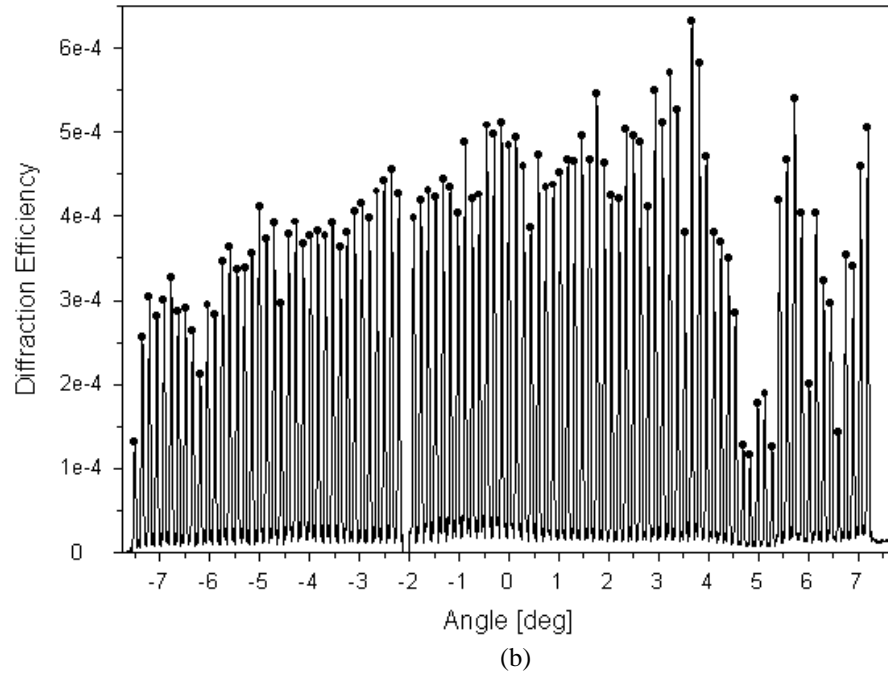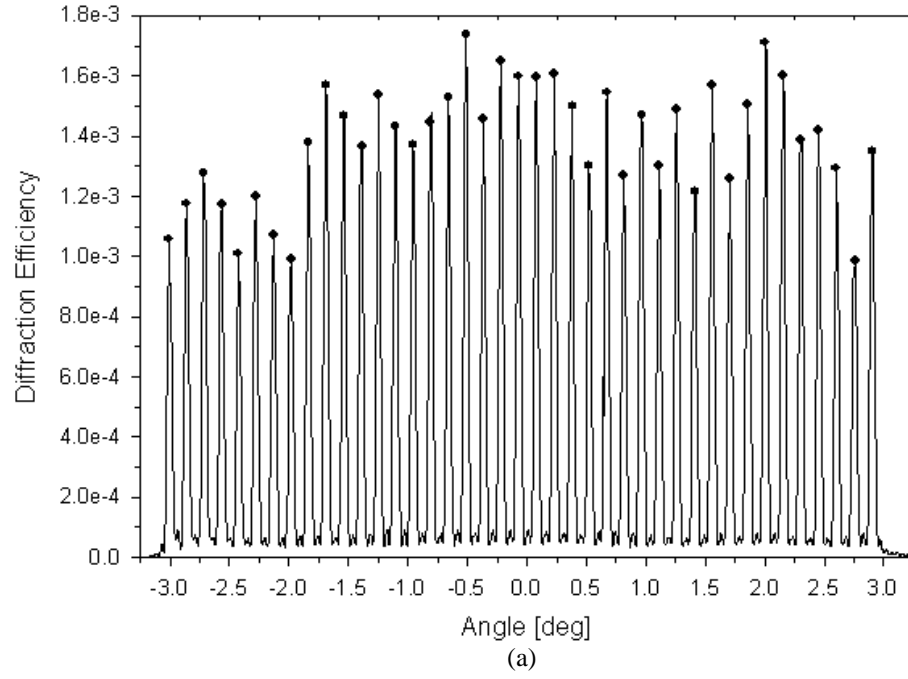
Fig. 2-22.   Comb function of (a) 41 and (b) 101 angularly multiplexed holograms equalized using recording schedule.

$$t_m = \cfrac{\tau_e}{m - 1 + \cfrac{\tau_e}{t_1}}, \qquad\qquad (2\text{-}6)$$

where τ_e is the erasure time constant of the crystal (in this case $\tau_e = 29304$ sec) and t_1 is the recording time of the first hologram. If t_1 is chosen to be τ_e, then the expression of t_m reduces to $\dfrac{\tau_e}{m}$. However, $t_1 = \tau_e$ may lead to undesirably long recording times, as it occurs in this case in which the erasure time constant is more than 8 hours.

If t_1 is smaller than τ_e, it is still possible to equalize the multiplexed holograms, although not the entire dynamic range of the material will be used. To see how the used portion of the dynamic range, $(M/\#)_{Used}$, relates to the real $(M/\#)$ of the material, consider the Mth hologram. Since it is the last hologram, it sees no erasure and therefore its grating strength is given by

$$\sqrt{\eta_M} = \frac{\partial}{\partial t}\sqrt{\eta} \cdot t_M. \qquad\qquad (2\text{-}7)$$

Plugging in the expressions for the recording slope and t_M, Equation 2-7 becomes

$$\sqrt{\eta_M} = \frac{A_o}{\tau_w} \cdot \cfrac{\tau_e}{M - 1 + \cfrac{\tau_e}{t_1}}, \qquad\qquad (2\text{-}8)$$

which can be re-written as

$$\sqrt{\eta_M} = (M/\#)_{Real} \cdot \cfrac{1}{M - 1 + \cfrac{\tau_e}{t_1}}. \qquad\qquad (2\text{-}9)$$

On the other hand, given the fact that the holograms have been equalized, the used portion of the $(M/\#)$ satisfies the relation $(M/\#)_{Used} = \sqrt{\eta_m} \cdot M$, in which $\sqrt{\eta_m}$ is the grating strength of the mth hologram. Since all the holograms are equally strong, it suffices

to take the case m=M and replace into Equation 2-9 to obtain finally the relation between

$(M/\#)_{Used}$ and $(M/\#)_{Real}$:

$$(M/\#)_{Used} = (M/\#)_{Real} \cdot \frac{M}{M - 1 + \dfrac{\tau_e}{t_1}} \qquad (2\text{-}10)$$

In Figure 2-22(a), the holograms have a diffraction efficiency of 1.39×10^{-3} on average, resulting in $(M/\#)_{Used}=1.53$. Since t_1 is just 1.02% of τ_e, only the 29.77% of the dynamic range was used, which means in fact M/5.13 for the thickness of the crystal. A similar result is obtained in Figure 2-22(b), in which the measured $(M/\#)_{Used}=2.26$ corresponds to just the 45.47% of the dynamic range, being M/4.97 the true value for the crystal. In both cases, the M/# is somewhat lower than the value computed using Equation 2-5.

The optical quality of $LiNbO_3$ is much higher than in any other of the materials that have been considered. This property, combined with a very low level of scattering of the material, makes possible to store data pages with very small pixel size. Figure 2-23 shows
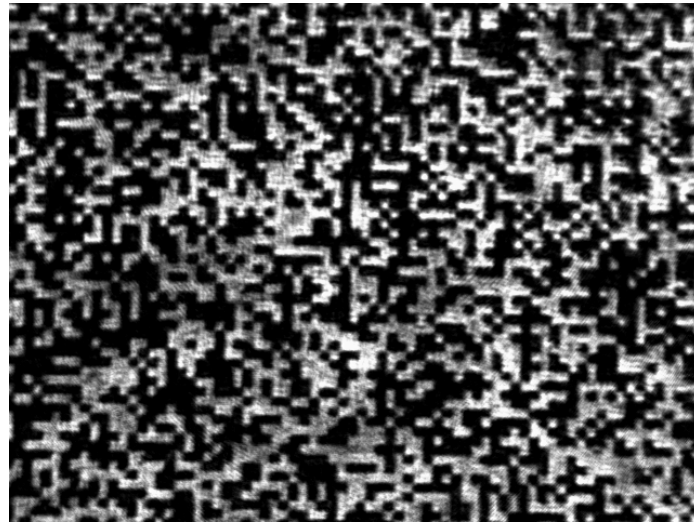
Fig. 2-23.   Phase-conjugate reconstruction of a 4 μm pixel hologram recorded in $LiNbO_3$.

a phase-conjugate reconstruction of a 4 μm pixel hologram recorded in the same 8 mm thick crystal. In the experiment, the hologram has been magnified using a ×40 microscope objective to image it onto a CCD camera with 9 μm pixel pitch. However, the system could have been made totally lensless by matching the pixels in the hologram to a 4μm-pitch CMOS detector. Two different metrics are commonly used to measure the quality of a detected hologram: the signal-to-noise ratio (SNR) and the bit-error rate (BER).
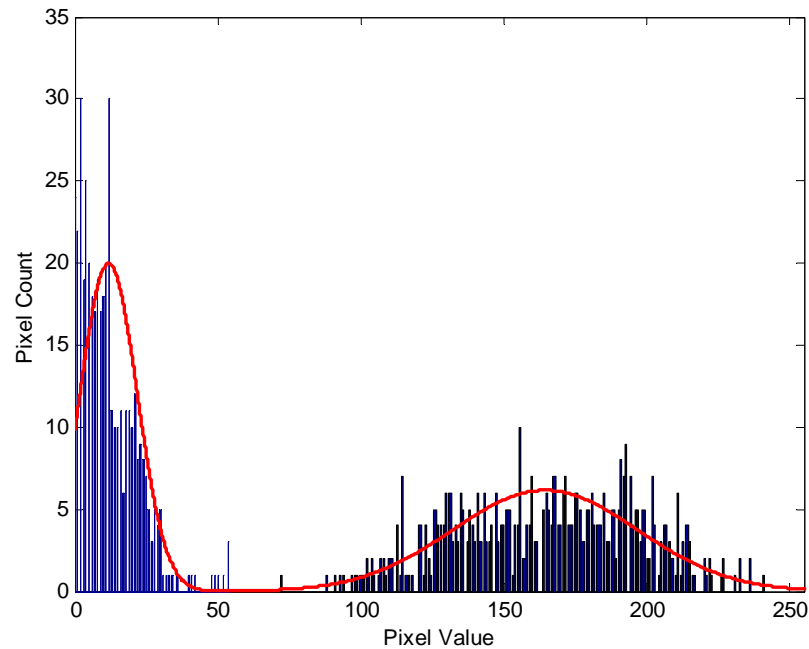
Fig. 2-24.   Histogram of pixel intensity of hologram shown in Figure 2-23 fitted to two normal distributions to compute the BER.

The SNR measures the contrast between the ON and OFF pixels of the hologram, which can be easily observed from the histogram of the intensities (digitized into 256 levels in an 8-bit resolution CCD) of the hologram pixels, as shown in Figure 2-24. Imperfections and local defects in the material, as well as in the optics of the setup, lead to intensity non-

uniformity of the reconstructed hologram, which results in a distribution of pixel intensities that cluster into two groups in the histogram. The SNR is then defined as

$$\text{SNR} = \frac{\mu_1 - \mu_0}{\sqrt{\sigma_1^2 - \sigma_0^2}}, \tag{2-11}$$

where μ_1 and σ_1 are the mean and standard deviation of the cluster corresponding to the ON pixels (logic "1"); and similarly μ_0 and σ_0 for the cluster of OFF pixels (logic "0").

The BER provides information about the probability of erroneous detection, and can also be obtained from the histogram by fitting each cluster to some type of probability distribution: $f_1(\cdot)$ for "1", and $f_0(\cdot)$ for "0". For example, the data in Figure 2-24 has been fitted to two normal distributions. The BER is then defined as

$$\text{BER} = P_1 \int_{-\infty}^{\gamma} f_1(\xi) \cdot d\xi + P_0 \int_{\gamma}^{\infty} f_0(\xi) \cdot d\xi, \tag{2-12}$$

where P_1 and P_0 are the symbol priors, usually taken $\frac{1}{2}$ because the holograms are random-pixel images, and γ is the decision threshold, which according to the maximum likelihood criterion is optimal when determined as the solution to $P_1 \cdot f_1(\gamma) = P_0 \cdot f_0(\gamma)$. If $f_1(\cdot)$ and $f_0(\cdot)$ are normally distributed, Equation 2-12 reduces to

$$\text{BER} = P_1 \cdot \text{erfc}\left(\frac{\mu_1 - \gamma}{\sqrt{2} \cdot \sigma_1}\right) + P_0 \cdot \text{erfc}\left(\frac{\gamma - \mu_0}{\sqrt{2} \cdot \sigma_0}\right). \tag{2-13}$$

The hologram in Figure 2-23 presents a global SNR across the entire image of 4.98, with regions where the SNR reaches a maximum of 5.18. The resulting raw BER (i.e., before any error-correction techniques are implemented) is 5.25×10^{-4}.

The above presented experimental results show that $LiNbO_3$ is able to meet both the optical quality requirements for small-sized pixels and the dynamic range considerations (i.e., M/5) for rapid configuration of the OPGA system. However, the larger thickness of the crystals (a few millimeters rather than a few hundred microns in polymers) puts more strain in the level of wavelength uniformity of the VCSELs. It is also important to point out that the volatility of the holograms has to be addressed for a long-term operation of the OPGA module. Solutions to this problem exists, like thermal fixing [2-21], although nonvolatility is obtained at the expense of M/#.

2.5 Module packaging

After presenting the properties and main issues of each one of the three major components of the OPGA module, it is necessary to discuss next the integration of the addressing device, optical memory, and CMOS chip, in a single package. The main goal is that the OPGA module needs to be small enough to be mounted on a computer board, thus the module should have a low profile. As already mentioned in Chapter 2, the height of the module depends only on the focal length of the lens used before the SLM, and this distance can be made as little as 1 cm. The module is very compact due to the lensless readout and to the small size of the area of the recording medium used to store the holograms.

The package shown in Figure 2-25 houses the optical memory on the top rectangular window. The VCSEL arrays, integrated on both sides, retrieve the holograms detected on the chip located on the bottom of the package. The package also needs to be robust to ensure the proper alignment between all of its components. It is important to preserve the one-to-one correspondence between the pixels in the hologram and the photodetectors on
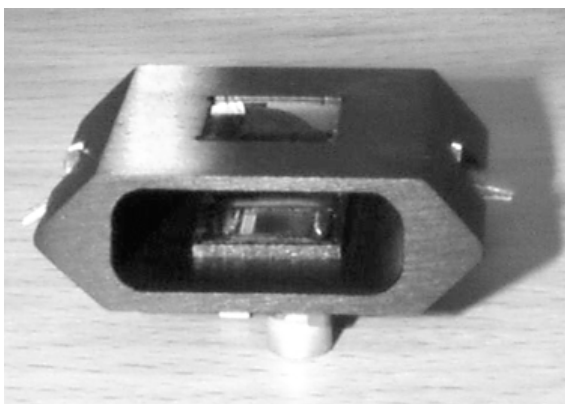
Fig. 2-25. Mechanical design of the OPGA module integrating in a compact package the optical memory (window on the top), VCSEL arrays (one on each side) and the chip (bottom).

the chip and also to avoid any change on the areas illuminated by the VCSELs on the optical material.

A first prototype has been developed to demonstrate that it is possible to integrate all three elements in a compact module. The module uses a 5×1 array of VCSELs to read out the holograms that have been stored in a 100 μm thick layer of DuPont photopolymer used as the optical memory. For this demonstrator, instead of the OPGA chip, a simple CCD camera chip was interfaced to the optical memory to detect the reconstructed holograms.

During recording, a laser diode stores two shift-multiplexed holograms in the memory at the two locations that match the position of the two VCSELs at each end of the array. The laser diode has been thermally controlled to match its wavelength to the one of the VCSELs. The experimental setup, shown in Figure 2-26, combines a reflection geometry architecture and lensless readout making the OPGA module very simple and compact. Once the recording operation is finished, the VCSEL array is assembled into the OPGA reader module, and the module removed from the setup of the recorder.
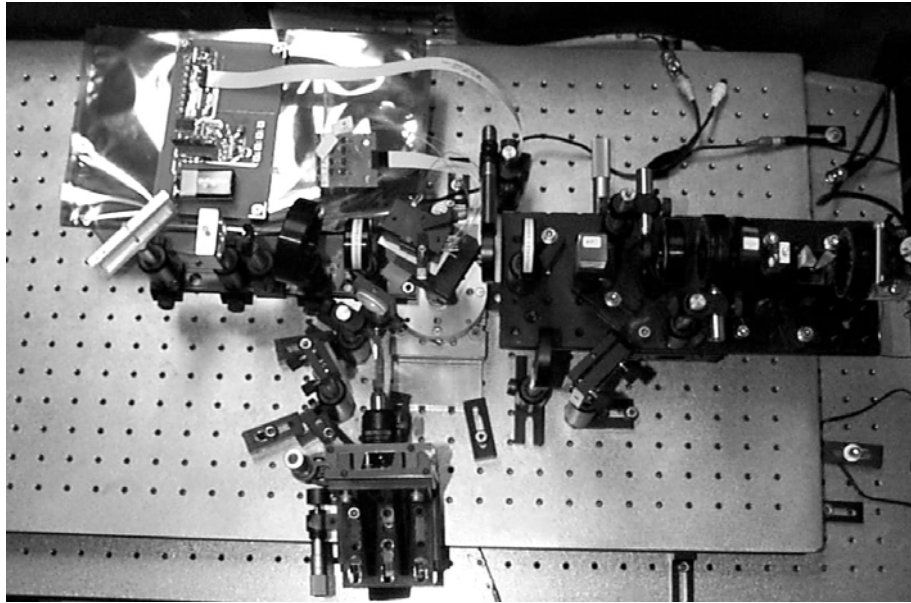
Fig. 2-26. Picture of the experimental setup used to record the holograms into the optical memory of the OPGA module.
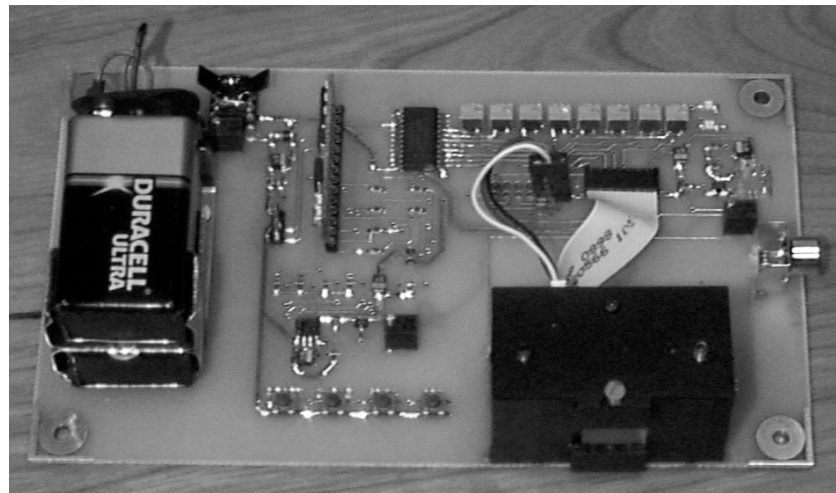
Fig. 2-27. First generation OPGA prototype mounted on the board that carries the circuitry to drive single VCSELs in the array and to power up the module.

The OPGA module is then mounted on a demo board, shown in Figure 2-27, that contains the additional circuitry to drive the VCSELs and select which element in the array is active. The board also carries the interface to the monitor where the holograms are displayed as they are read out by the VCSELs (Figure 2-28).

62
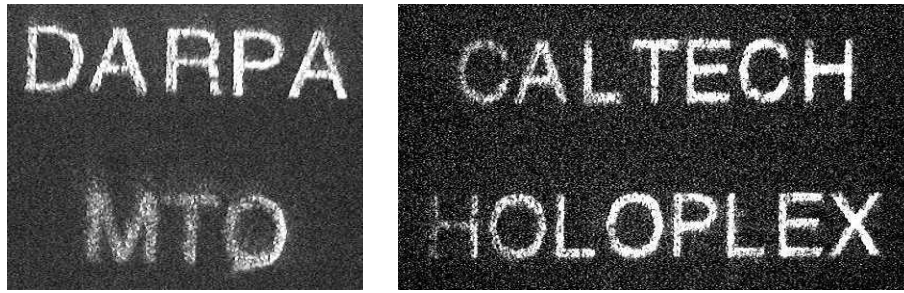
Fig. 2-28. Reconstruction of the two holograms stored in the optical memory of the OPGA prototype. Two different VCSELs are used to retrieve one hologram at a time.

A more advanced packaging for the OPGA module has been proposed and demonstrated in [2-12]. The module achieves an extremely low profile by directly mounting the optical memory, a thin slab of $LiNbO_3$:Fe, on top of the OPGA chip as depicted in Figure 2-29. The system makes use of the folded shift multiplexing technique[2-12] to store holograms into the memory. The light from the VCSELs is coupled into the crystal from the edge and guided along the crystal as it bounces off the top and bottom surfaces due to total internal reflection to read out the holograms, which are projected onto the OPGA chip.
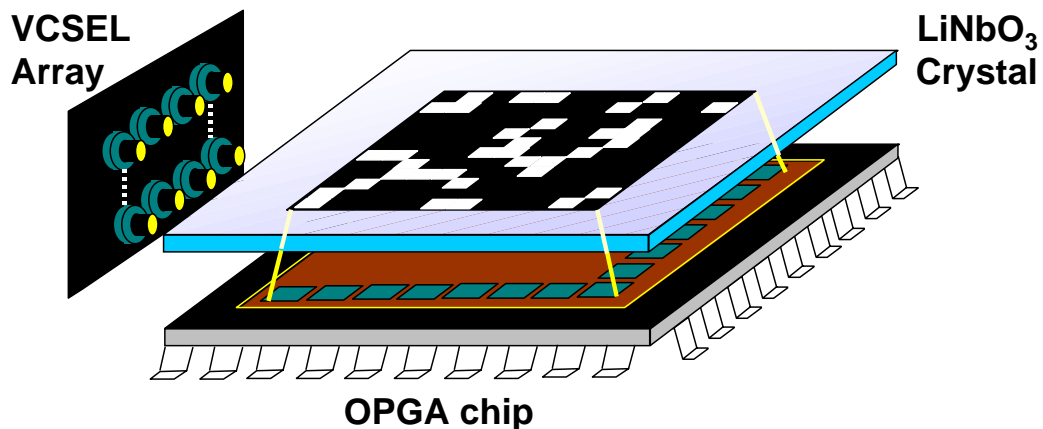
Fig. 2-29. Advanced packaging for the OPGA in which a thin slab of $LiNbO_3$ is directly mounted on top of the OPGA chip. The beam from the VCSEL is guided inside the crystal.

2.6 System demonstration

The previous section discussed the integration of the three components of the OPGA into a compact module. A demo OPGA module was developed in which VCSELs were used to read out holographic data pages from the optical memory. However, the system used a CCD camera instead of the OPGA chip. In this section, the holographic programming of the OPGA chip will be demonstrated. The system described here interfaces the full OPGA chip with an optical memory containing the configuration templates that are downloaded onto the chip upon readout.

2.6.1 Demonstrator setup

The 514 nm line of an Argon ion laser is used in the experimental setup sketched in Figure 2-30. In order to record the holograms in the OPGA system, the laser light beam is split into two arms. The signal beam illuminates a 15 μm pixel 320 × 240 Kopin SLM. The pattern displayed on the SLM is projected onto the chip using two 5 cm focal length Nikon lenses arranged in a 4-f system and pixel-matched to the APS array of the chip.

The holographic memory, in this particular demonstration a 38 μm thick sample of Du Pont photopolymer, is placed between the SLM and the first Nikon lens. The optical medium is mounted on a rotation stage to provide peristrophic multiplexing. The iris placed at the Fourier plane of the first lens in the 4-f system, initially intended to filter out the higher diffraction orders of the signal beam produced by the pixelation of the SLM, will also serve to block all the peristrophically multiplexed holograms that are not selected to program the chip at any given time. Simple additional optics is necessary to bring a plane wave reference beam onto the holographic material at an angle of incidence of 45° with
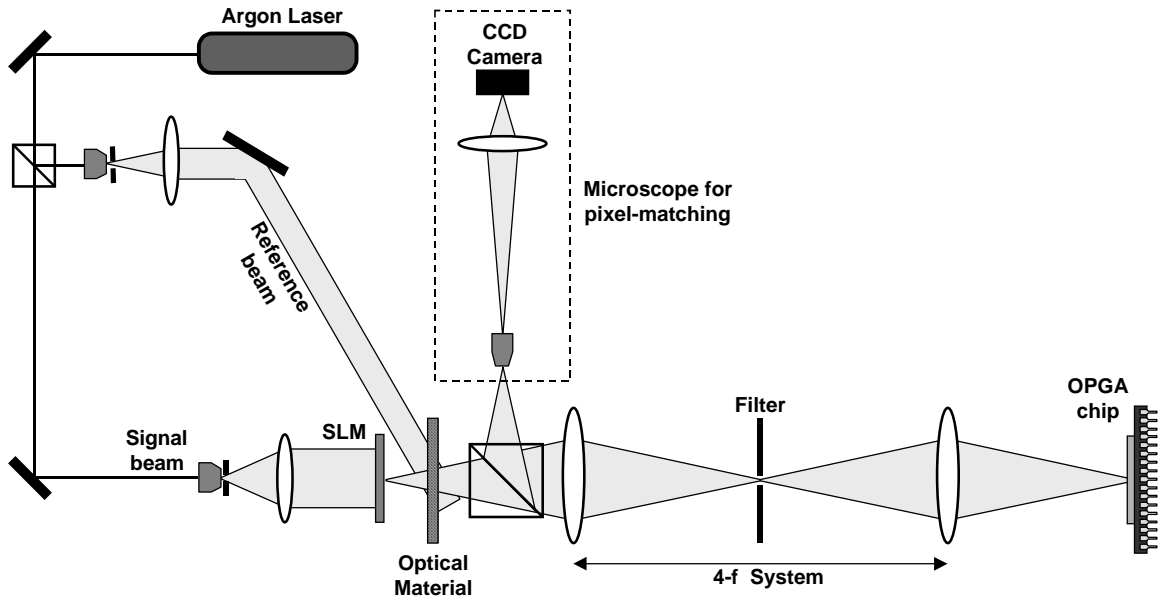
Fig. 2-30. Experimental setup for the holographic programming of the OPGA chip. The microscope (inside the dashed-line box) is used to monitor the pixel-matching process.

respect to its surface normal. The total intensity of the recording beams has been set to 1.5 mW/cm^2.

2.6.2 Pixel alignment process

The differential-encoding scheme used by the OPGA chip makes the process of pixel-matching the SLM to the APS array more difficult. As described in Section 2.3.1, each pair of pixels in the SLM is mapped into one bit of information. The alignment is complicated by the fact that the output of the chip does not correspond to the image on the SLM as seen by the APS array on the chip (i.e, a 64×64 pixel array), but to the differentially detected configuration bits (i.e., a 64×32 data page). Therefore, the digitized output of the chip alone does not provide enough information to guide the alignment process.

Instead, pixel-matching between the SLM and the chip has been performed with the aid of a microscope as shown in Figure 2-30. Due to the imaging property of the 4-f system,

when the chip is illuminated with an incoherent light source (e.g., a white LED illuminator), the light reflected off the surface of the chip forms an image of the array of photodetectors at a distance equal to one focal length in front of the first Nikon lens. The microscope magnifies this image, Figure 2-31(a), and projects it onto a CCD camera.

| (a) | (b) | (c) |
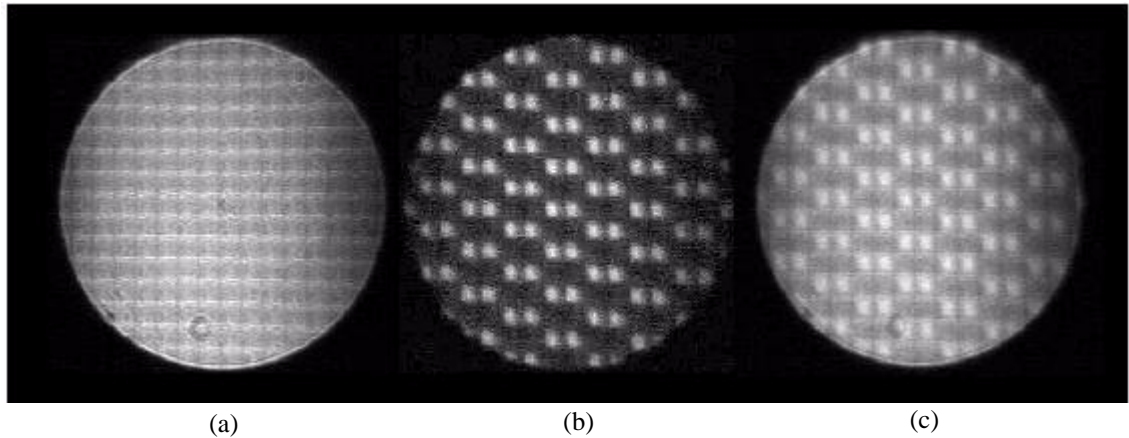
Fig. 2-31.   Pixel alignment process showing the image of (a) the APS array on the chip, (b) the pixels on the SLM, and (c) the SLM pixels superimposed on the APS array.

Similarly, the pattern displayed on the SLM can also be observed on the microscope. The pixels of the SLM are imaged first on the OPGA chip. However, the chip can be viewed as a partial mirror that reflects some of the light that comes from the SLM. This light travels back through the 4-f system and forms an image again at one focal length away from the first lens, right in front of the microscope, Figure 2-31(b). The pixel-matching condition is achieved when the pattern displayed on the SLM coincides with the layout of the APS array, Figure 2-31(c).

2.6.3 Holographic programming

Once the optical interface is properly aligned, holograms carrying configuration data can be recorded in the optical memory, and their reconstructions used to drive the logic

of the OPGA. Figure 2-32 shows the reconstruction of a hologram as seen by the APS array on the chip. The differential nature of the encoded data is evident from the fact that columns of mostly ON pixels are immediately followed by a column in which the only ON pixels occur at the vacancies of the previous column.
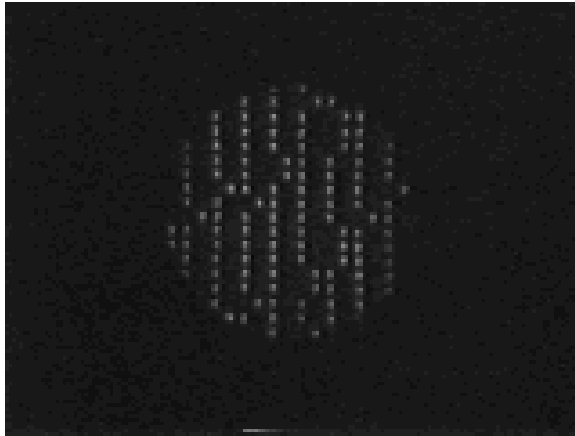
Fig. 2-32.   Reconstruction of a hologram containing configuration data. The extension of the region of the hologram that can be visualized on the CCD is limited by the aperture of the objective lens in the microscope.

The digitized output of the APS array is accessible from the outside of the chip and can be visualized on a computer screen via a parallel port that connects the board that carries the OPGA chip to a computer. The 64×32 output pattern in Figure 2-33, corresponding to the hologram showed in Figure 2-32, is retrieved free from error. The detected data is then used to program the logic array of the OPGA to perform some type of computation. Given that only 13 rows out of the 64 available in the APS array are needed to fully configure the logic, several optical programs can be stored in the hologram and downloaded into the chip in less than 8 µs (APS integration time).

Two different operations can be programmed using this hologram: Configuration #1 routes a 5-bit input signal from the I/O port on the left of the chip throughout the chip
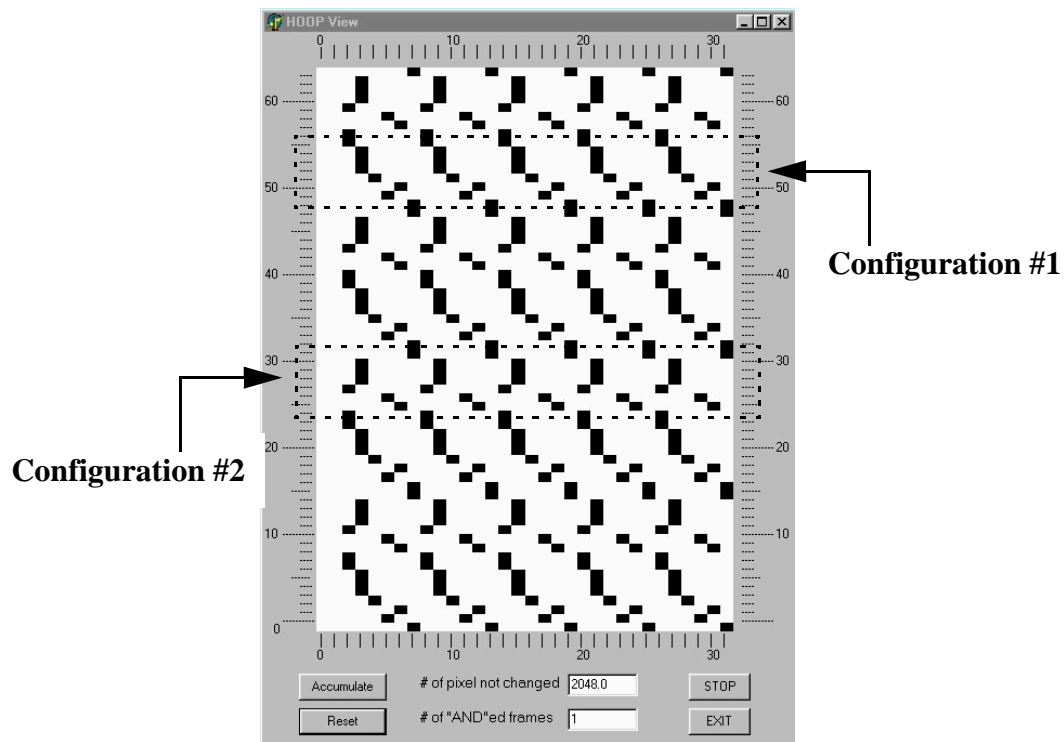
Fig. 2-33. Digitized output of the APS array showing the programming information contained in the hologram after being differentially detected. The hologram contains two configuration templates in the rows encircled by dotted lines.

and is finally delivered to the I/O port on the top of the logic array (labeled as Output Port A) in Figure 2-34(a). On the other hand, configuration #2 modifies the internal state of the crossbar switching matrices, so the input signal is re-routed towards the I/O port on the right of the chip (labeled as Output Port B) in Figure 2-34(b). The operation of the chip is experimentally verified with a test signal generated by a 5-bit counter that cycles through all its 32 logic states. The results of the holographic programming can be observed in the scope trace in Figure 2-35. As the programming of the chip toggles continuously between configuration #1 and #2, the input signal is alternatively delivered to either port A or port B.

The ability to reconfigure the OPGA using different rows of the APS array is equivalent to the concept of partial reconfiguration used in the FPGA community, when only part

Fig. 2-34. Routing scheme programmed by each one of the two configurations contained in the hologram. (a) Configuration #1 delivers the 5-bit input to Output Port A (on the top), while (b) Configuration #2 sends it to Output Port B (on the right).
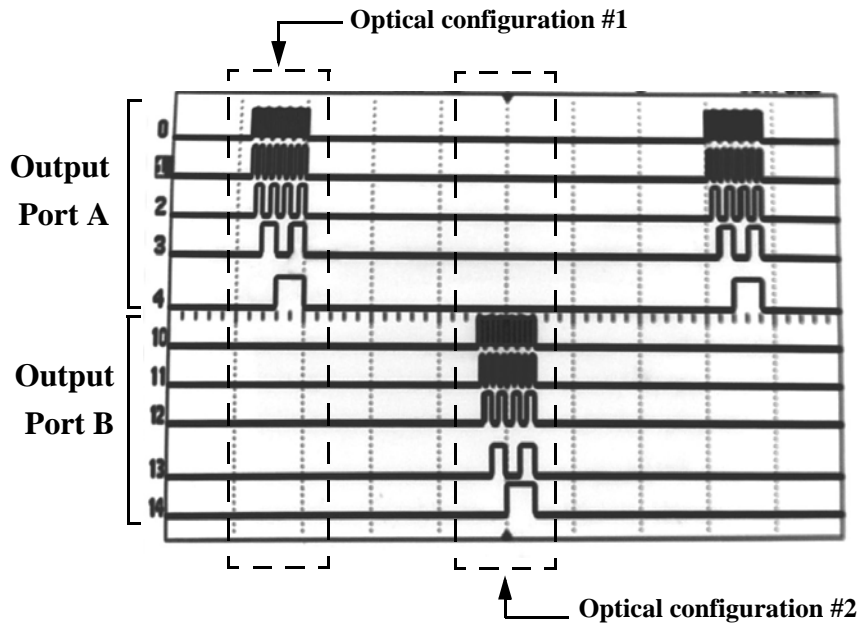
Fig. 2-35. Scope trace of the output of the logic block array as programmed optically. A 5-bit input signal is delivered cyclically to either Output Port A during Configuration #1, or Output Port B during Configuration #2.

of the logic of the FPGA needs to be reprogrammed. Having different configurations coex-

isting on the same hologram adds flexibility to the OPGA.
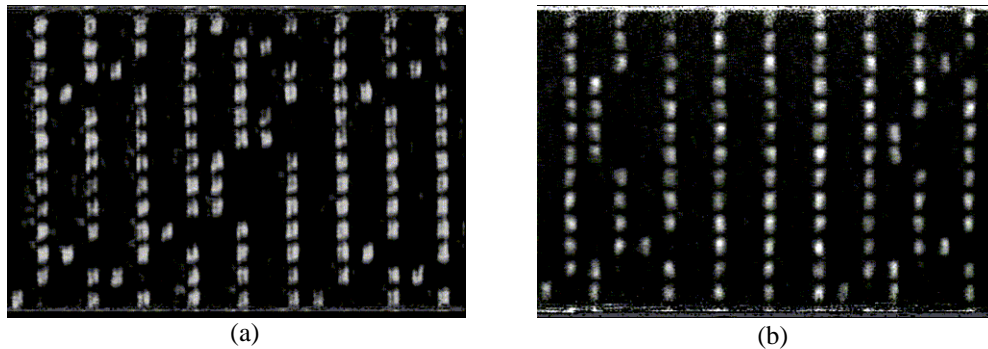
Fig. 2-36. Reconstruction of the two multiplexed holographic templates as seen by the APS array. Each hologram carries two configuration programs: (a) *Hologram I* contains Configuration #1 and #2, while (b) *Hologram II* contains #3 and #4.

Finally, full reconfiguration using different holograms has been demonstrated by

peristrophically multiplexing two holographic patterns in the optical memory with an angu-

lar separation of 20° between them. The reconstruction of the two holographic templates is presented in Figure 2-36. By rotating the optical medium, it is possible to select between *Hologram I* and *Hologram II* to implement global reconfiguration of the chip. Furthermore, by choosing which rows to use within each hologram, two different functions can be programmed. Therefore, 4 different configurations can be downloaded into the chip. While the two operations performed by *Hologram I* have already been described (see Figure 2-34), the ones performed by *Hologram II* (configurations #3 and #4) are presented in Figure 2-37 and explained below.

Configuration #3 broadcasts the signals from the input port to both output ports, while configuration #4 splits the input lines into two groups: those corresponding to the even bits are sent to Output Port A, and the lines carrying the odd bits are sent to Output Port B. The experimental results are presented in Figure 2-38. The 5-bit counter used as test input signal appears on both output ports during configuration #3, as shown in the scope trace. When the OPGA is programmed with configuration #4, the bits with weights 2^0, 2^2 and 2^4 are detected on Output Port A, while the ones with weights 2^1 and 2^3 appear on Output Port B.

The reconfiguration time (T_{config}) can be defined as the interval between the end of the execution of the program under the current configuration (i.e., once the 5-bit counter has cycled through its 32 logic states) and the beginning of the execution of a different program with the new configuration (i.e., the first logic state of the counter). The configuration time includes the readout cycle of the selected rows of the APS array, plus the delivery time of the configuration bits to the logic blocks. In the experiment shown in Figure 2-38, the measured T_{config} was 127 µs for full chip configuration. This time has to be interpreted as

71
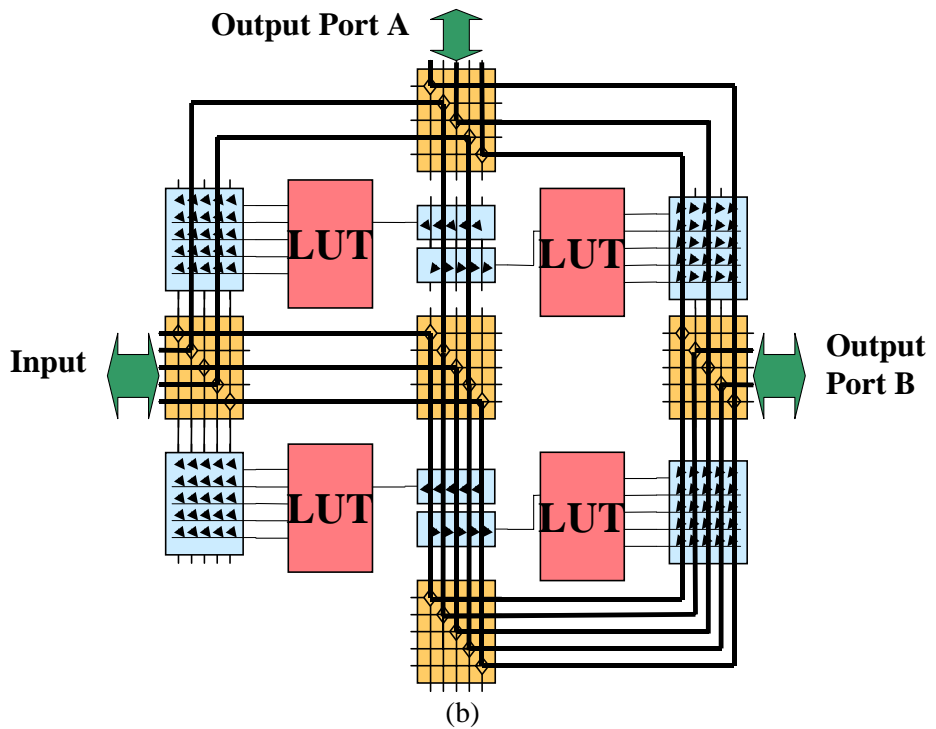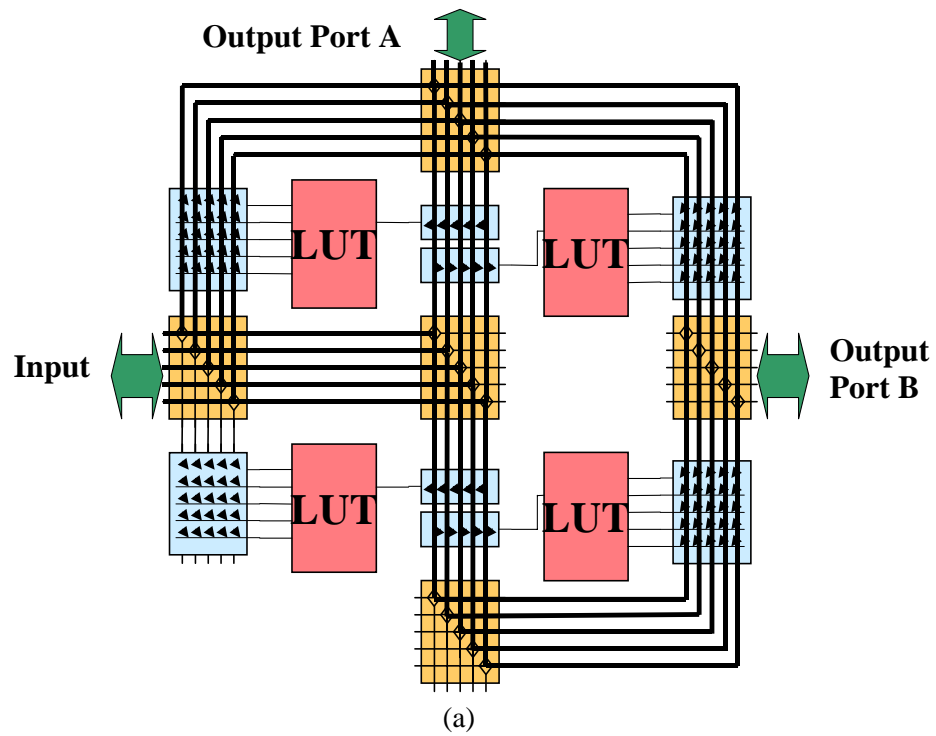
Fig. 2-37. Routing scheme programmed by the two configurations contained in *Hologram II*. (a) Configuration #3 broadcasts the 5-bit input to both Output Port A and B, while (b) Configuration #4 sends the even lines of the input to Output Port A and the odd lines to Output Port B.
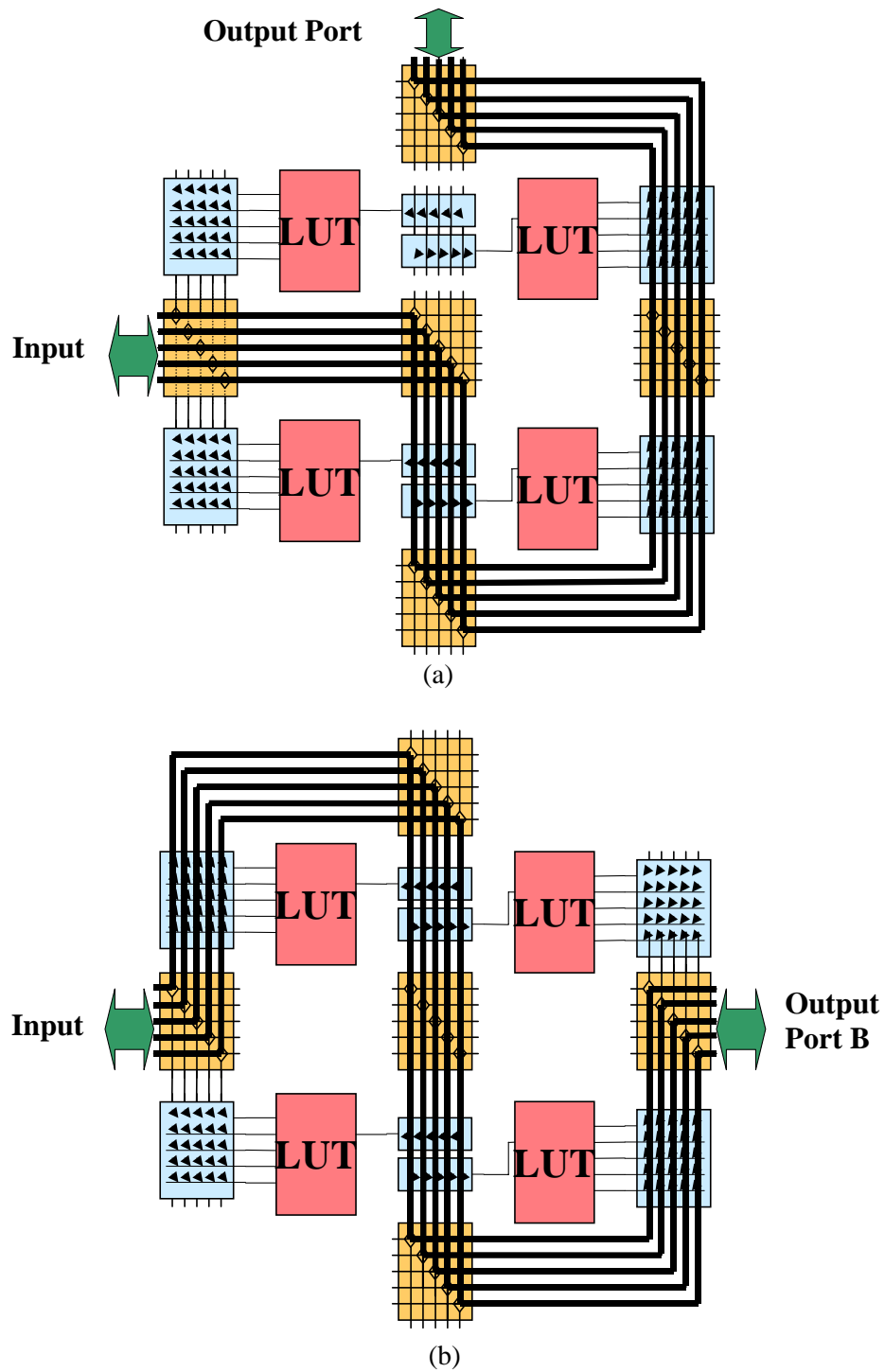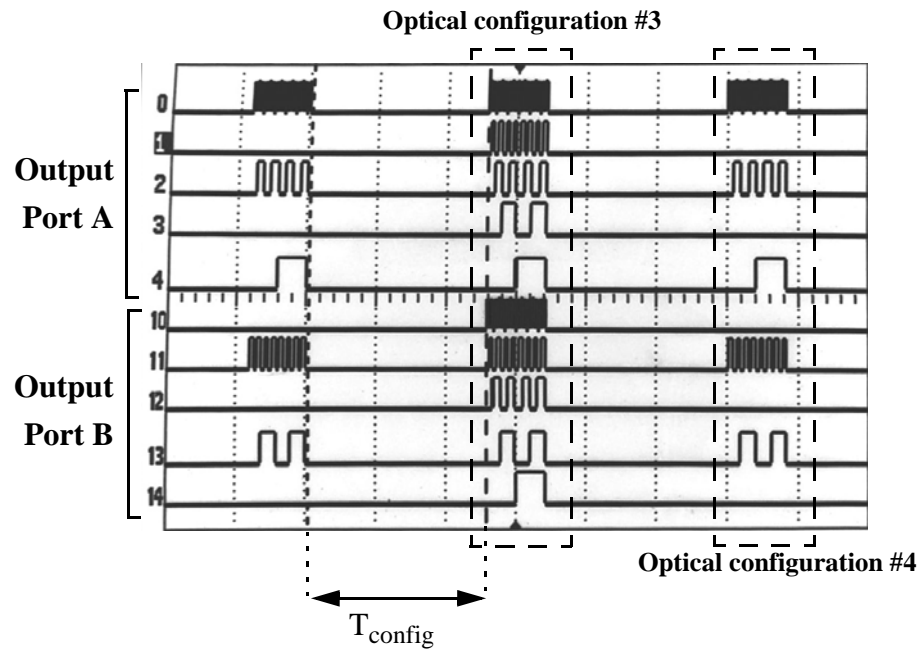
Fig. 2-38. Scope trace of the output of the logic block array as programmed optically by *Hologram II*. The 5-bit input signal is broadcast to both output ports during Configuration #3, and split into even and odd lines during Configuration #4. The reconfiguration time T_{config} is 127 μs.

an upper bound, because it is limited by the master clock signal of 500 KHz generated by the OPGA board.

This last experiment demonstrates the feasibility of transferring information in parallel from a holographic database to a silicon chip, and the high degree of flexibility derived from the reconfiguration capabilities. The system can be expanded to include more holographic templates using materials with larger dynamic range and better optical quality, like Aprilis photopolymer.

Automation of the rotation stages to implement either peristrophic or angular multiplexing should also be carefully explored. The reconfiguration time measured in the experiments did not take into consideration the time it takes to retrieve a particular holographic data page from the optical memory. The use of a VCSEL array in the design of the

OPGA made the readout time be negligible because no mechanical components were involved. However, if a single laser is to be used to overcome the limitations of the red VCSELs, the use of a fast steering device is required to keep the reconfiguration time low. Fortunately, the increase in available output power that a laser diode provides with respect to the VCSELs makes possible to trade off longer retrieval times with shorter photodetector integration times.

References

[2-1] A. V. Krishnamoorthy, K. W. Goossen, L. M. F. Chirovsky, R. G. Rozier, P. Chandramani, W. S. Hobson, S. P. Hui, J. Lopata, J. A. Walker, and L. A. D'Asaro, "16×16 VCSEL array flip-chip bonded to CMOS VLSI circuit," *IEEE Photonics Technology Letters* **12**, 1073-1075 (2000).

[2-2] R. P. Schneider Jr., and J. A. Lott, "Cavity design for improved electrical injection in InAlGaP/AlGaAs visible (639–661 nm) vertical-cavity surface-emitting laser diodes," *Applied Physics Letters* **63**, 917-919 (1993).

[2-3] J. Mumbru, G. Panotopoulos, D. Psaltis, X. An, F. Mok, S. Ay, S. Barna, and E. Fossum, "Optically programmable gate array," *Proc. SPIE of Optics in Computing 2000* **4089**, 763-771 (2000).

[2-4] S. Mendis, S. E. Kemeny, and E. R. Fossum, "CMOS active pixel image sensor," *IEEE Transactions on Electronic Devices* **41**, 452-453 (1994).

[2-5] E. R. Fossum, "CMOS image sensors: Electronic camera-on-a-chip", *IEEE Transactions on Electronic Devices* **44**, 1689-1698 (1997).

[2-6] J. F. Heanue, M. C. Bashaw, and L. Hesselink, "Volume holographic storage and retrieval of digital data," *Science* **265**, 749-752 (1994).

[2-7] D. Psaltis, and G. W. Burr, "Holographic data storage," *Computer* **31**, 52-60 (1998).

[2-8] G. J. Steckman, I. Solomatine, G. Zhou, and D. Psaltis, "Characterization of phenanthrenequinone-doped poly(methyl methacrylate) for holographic memory," *Optics Letters* **23**, 1310-1312 (1998).

[2-9] D. A. Waldman, H.-Y. S. Li, M. G. Horner, "Volume shrinkage in slant fringe gratings of a cationic ring-opening holographic recording material," *Journal of Imaging Science and Technology* **41**, 497-514 (1997).

[2-10] D. A. Waldman, H.-Y. S. Li, and E. A. Cetin, "Holographic recording properties in thick films of ULSH-500 photopolymer," *Proc. SPIE of Diffractive and Holographic Device Technologies and Applications* **3291**, 89-103 (1998).

[2-11] L. Paraschis, Y. Sugiyama, L. Hesselink, "Physical properties of volume holographic recording utilizing photo-initiated polymerization for nonvolatile digital data storage," *Proc. SPIE of Conference on Advanced Optical Data Storage: Materials, Systems, and Interfaces to Computers* **3802**, 72-83 (1999).

[2-12] C. Moser, *Optical Information Processing*, Ph.D. thesis, California Institute of Technology, 2001.

[2-13] K. Buse, A. Adibi, and D. Psaltis, "Non-volatile holographic storage in doubly doped lithium niobate crystals," *Nature* **393**, 665-668 (1998).

[2-14] K. Buse, A. Adibi, and D. Psaltis, "Efficient non-volatile holographic recording in doubly doped lithium niobate," *Journal of Optics A-Pure and Applied Optics* **1**, 237-238 (1999).

[2-15] J. A. Jenney, "Holographic recording with photopolymers," *Journal of the Optical Society of America* **60**, 1155-1161 (1970).

[2-16] M. J. Jeudy, and J. J. Robillard, "Spectral sensitization of a variable index material for recording phase holograms with high efficiency," *Optical Communications* **13**, 25 (1975).

[2-17] S. Blaya, L. Carretero, R. Mallavia, A. Fimia, R. F. Madrigal, M. Ulibarrena, and D. Levy, "Optimization of an acrylamide-based dry film used for holographic recording," *Applied Optics* **37**, 7604-7610 (1998).

[2-18] K. Curtis, A. Pu, and D. Psaltis, "Method for holographic storage using peristrophic multiplexing," *Optics Letters* **19**, 993-994 (1994).

[2-19] A. Pu, K. Curtis, and D. Psaltis, "Exposure schedule for multiplexing holograms in photopolymer films," *Optical Engineering* **35**, 2824-2829 (1996)

[2-20] F. H. Mok, "Angle-multiplexed storage of 5000 holograms in lithium niobate," *Optics Letters* **18**, 915-917 (1993).

[2-21] X. An, D. Psaltis, G. W. Burr, "Thermal fixing of 10,000 holograms in LiNbO$_3$:Fe," *Applied Optics* **38**, 386-393 (1999).

[2-22] E. Chuang, W. H. Liu, J. J. P. Drolet, D. Psaltis, "Holographic random access memory (HRAM)," *Proceedings of the IEEE* **87**, 1931-1940 (1999).

[2-23] F. H. Mok, G. W. Burr, D. Psaltis, "System metric for holographic memory systems," *Optics Letters* **21**, 896-898 (1996).

[2-24] G. W. Burr, *Volume holographic storage using the 90° geometry*, Ph.D. thesis, California Institute of Technology, 1996

3 . **Holographic 4-D imaging**

Optical data storage is one of the areas in which holography has been extensively used. In a holographic memory, the information is encoded into the hologram and retrieved with a laser beam, usually a simple plane wave. This section deals with the use of holography for imaging applications. In this case, the information is no longer stored in the hologram itself, but in the spatially encoded wavefront of the probing beam. The Bragg-selectivity property of a volume hologram that is extremely useful for high-density data storage, can in fact be also efficiently utilized in imaging applications, like confocal microscopy [3-1], [3-2] or tomography [3-3].

The problem here considered is the use of holograms to extract spatial and color information (hence 4-D imaging) of a specimen and project it onto a 2-D space on the detector. Apart from holography, other techniques are used to perform such transformation. For example, the confocal microscope places a pinhole at the finite conjugate distance of the imaging lens before the detector in order to discriminate one point at a particular depth in the specimen. Light originating from neighboring points will miss the pinhole, or will be defocused, so the pinhole filters out background noise improving the resolution of the system. A variation of this technique is the two-photon excitation microscopy (TPEM) [3-4], [3-5], in which 3-D localization is achieved by focusing high-energy femtosecond pulses inside the specimen, instead of using a pinhole.

Both confocal and two-photon microscopy suffer from the same limitation, namely only the information of one point of the specimen is gathered at a time. Consequently, there needs to be a scanning mechanism to reconstruct the entire volume of the specimen. Moreover, if color information is required, several measurements need to be taken using different color filters. The inherent parallelism that holographic systems enjoy can satisfactorily overcome these limitations. Unlike the aforementioned techniques, holographic imaging renders simultaneously a 2-D slice of the specimen on the detector. Furthermore, by multiplexing several holograms, many of such slices (at different depths and in different color bands) can be sensed in parallel, making unnecessary the use of sophisticated and time-consuming scanning schemes. Therefore, the holographic microscope has an enormous potential for applications that demand real-time microscopy.
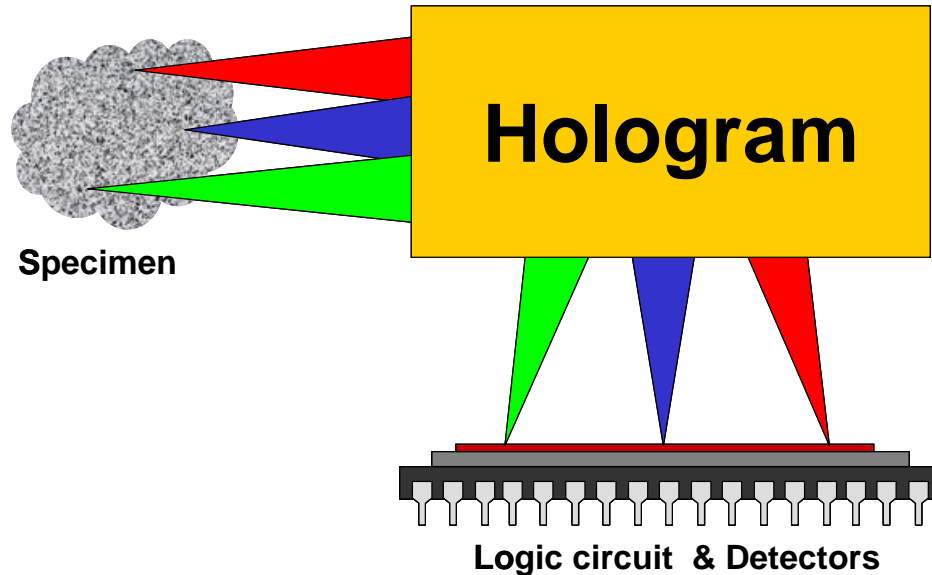
Fig. 3-1. 4-D microscope interfacing a holographic module with a chip that integrates photodetectors and processing resources.

Although essentially different in operation to the OPGA, the 4-D microscope still shares important commonalities with the former. Like an OPGA, the holographic micro-

scope (sketched in Figure 3-1) consists of the integration of three major components: a holographic element, a silicon chip (e.g., CCD camera, CMOS imager...) and an addressing device (e.g., a fluorescent specimen). However in the microscope, instead of having VCSELs reading out complex datapages stored in the optical memory, the spatially encoded light from the specimen is diffracted by simple gratings.

The 4-D microscope also enjoys the concept of reconfigurability, since the holograms stored in the device perform different tasks, like focusing at a particular depth or filtering a specific spectral band. Depending on the light wavefronts emanating from an unknown fluorescent specimen, various holographic templates will be selected, and the information delivered to different areas of the detector array in the chip. As in the OPGA, the adaptability and parallelism of the holographic microscope are vital for the real-time processing of the information contained in the specimen.

Finally, the 4-D microscope could also benefit from a direct interface between its holographic module and a silicon chip that integrates both logic circuitry and a detector array, since it would allow to implement a variety of image-processing tasks, like template matching for example, or even perform on-chip analysis to extract information from the specimen.

3.0.1 Principle of operation

To illustrate the principle of operation of the holographic microscope, consider the case of a transmission-geometry volume hologram, as depicted in Figure 3-2. Assume that a pure sinusoidal grating has been recorded by the interference between a plane wave prop-
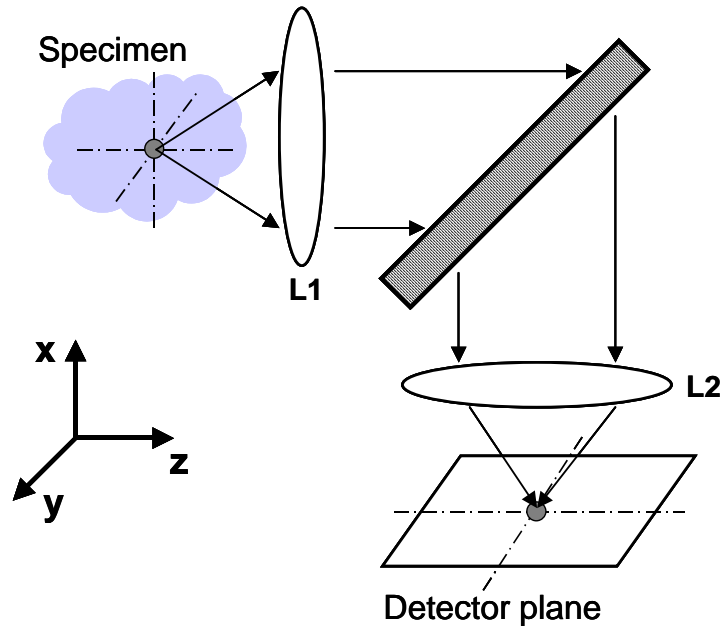
Fig. 3-2.   Schematic of a microscope that utilizes a transmission-geometry volume hologram. L1 and L2 are lenses.

agating along the $-\hat{x}$ direction and a collimated beam propagating along the $\hat{z}$ axis gener-ated by a point source located on-axis at the focal plane of lens L1.

Because of the angular Bragg selectivity of the hologram, strong diffraction is only achieved when the position of a probing monochromatic point source on the (x, y)-plane matches the location of the point source used during recording. The diffracted light is focused into a point on the detector plane. If the probing point source is shifted along the x-axis, the hologram becomes quickly Bragg-mismatched and no light is diffracted towards the detector. One exception to this is what occurs along the y-axis. The recording geometry makes this direction be degenerate, which means that as the probing point source is shifted along this axis, the Bragg condition is always satisfied. Therefore the points in the specimen along a line parallel to the y-axis map into a line on the detector plane.

Similarly, the grating also exhibits Bragg selectivity in wavelength, which means that if the wavelength of emission of the probing point source differs from the wavelength at which the hologram was recorded, then the amount of diffracted power on the detector becomes negligible very rapidly.

In order to produce a full 2-D image on the detector plane, consider the Bragg condition for a symmetric grating given by

$$\Lambda = \frac{\lambda}{2 \cdot \sin\theta},$$

(3-1)

where Λ is the spatial period of the grating, λ the wavelength of the probing beam, and θ its angle of incidence (measured with respect to the surface normal of the material). Equation 3-1 establishes a coupling between wavelength and angle (or equivalently position along the x-axis) that makes it possible for points along the x-axis to Bragg-match the hologram, provided that the appropriate wavelength is selected. Therefore, when a specimen is illuminated with an extended broadband source, the hologram performs a one-to-one mapping between points on the (x, y)-plane and the detector plane.

As in a confocal microscope, the hologram is also able to discriminate light originating from different depths. The selectivity in depth is related to the angular Bragg selectivity of the grating. As the probing point source is shifted along the z-axis away from the focal plane of lens L1, the wavefront after the lens becomes spherical. A spherical wave can be regarded as the superposition of plane-wave components propagating at different angles. As the wave acquires more sphericity, fewer components remain Bragg-matched, therefore the amount of diffracted power decreases to zero.

3.0.2 Experimental imaging

A holographic microscope has been built to test its performance and use it in imaging applications. The sketch in Figure 3-3 depicts a basic transmission-geometry setup, in
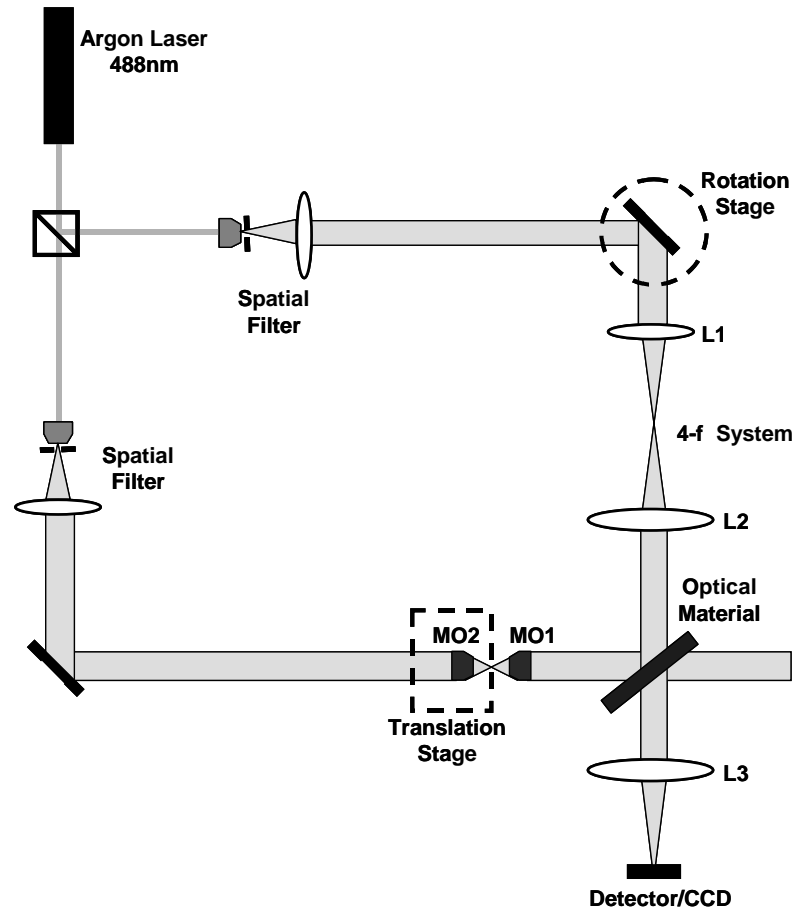
Fig. 3-3. Experimental setup of the recorder for the 4-D microscope. MO1 and MO2 are two microscope objectives, while L1, L2, and L3 are lenses. During normal operation, the microscope consists only of MO1 and L3, in addition to the optical material.

which the angle of incidence of each arm is 45° (in air) with respect to the surface normal of the optical medium. In fact, the holographic microscope consists just of a ×40/0.65NA microscope objective (MO1 in Figure 3-3), the holographic element and an imaging lens (an 8 cm focal-length lens labeled as L3) to relay the specimen on the CCD.

The recording process occurs *in situ*, and requires the additional optical elements shown in the figure. In order to simulate a point source, a second ×40/0.65NA microscope objective (MO2) is placed in the signal path before MO1 to focus the beam. Microscope objective MO1 collimates the signal wavefront before it impinges the optical medium. To tune the hologram to get information from a particular depth, the position of the simulated point source can be varied by means of a motorized translation stage on which microscope objective MO2 has been mounted. After microscope objective MO1, a slightly converging (diverging) signal beam interferes with the reference beam, a simple plane wave, to record a hologram sensitive to a depth longer (shorter) than the focal length of the microscope objective.

The information of multiple depth-slices can be obtained by multiplexing several holograms. In this case, each depth-slice can be separated on the detector plane (the Fourier-plane of L3) by slightly changing the angle of the reference beam during recording. In the experimental setup, this is achieved with a mirror mounted in a rotation stage and a pair of lenses (L1 and L2) forming a 4-f system. Finally, information from different spectral bands can be gathered by tuning the holograms accordingly, which would require to adjust the angle of both recording beams. Although possible, this feature has not been added to the experimental setup.

The resolution of the system has been checked in first place. A single hologram was recorded using the 488 nm line of the Argon laser in a 5 mm thick x-cut $LiNbO_3$:Fe crystal with 0.05% wt doping. The intensity of each beam was 9 mW/cm^2 and the crystal was exposed for 3 hours. At the end of the experiment the diffraction efficiency of the hologram reached 13%. The selectivity in depth of the hologram as the simulated point source is

shifted along the z-axis (as defined in Figure 3-2) from its position during recording is pre-

sented in Figure 3-4. The experimental data (dots) is compared to the theoretical prediction
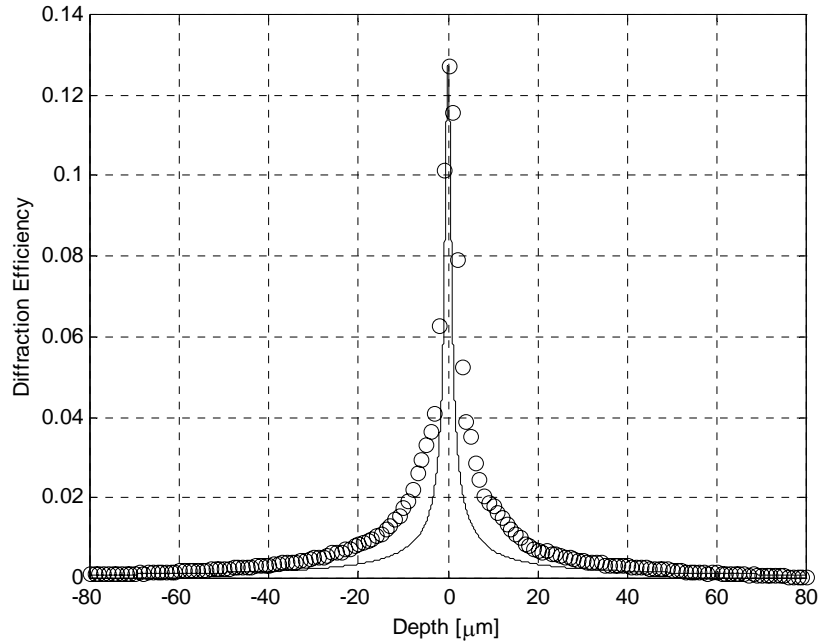
Fig. 3-4. Depth selectivity measurement (dots) of a hologram recorded on 5 mm thick LiNbO$_3$ crystal compared to the theoretical prediction (solid line).

(solid line) calculated using the method described in Section 3.0.3.3. The measured depth

resolution (Δz) is 4 μm FWHM, which is larger than the predicted value of 2 μm. However,

an experimental value larger than the prediction is expected due to aberrations, mainly in

the imaging lens but also in the microscope objective.

The angular selectivity curve of the hologram has also been measured and com-

pared with the theory (Figure 3-5). The Bragg selectivity is approximately 1.25×10^{-2}

degrees (outside the crystal), which means that, using a ×40/0.65 microscope objective, if

a monochromatic point source is shifted by more than 1μm along the x-axis (as defined in

84
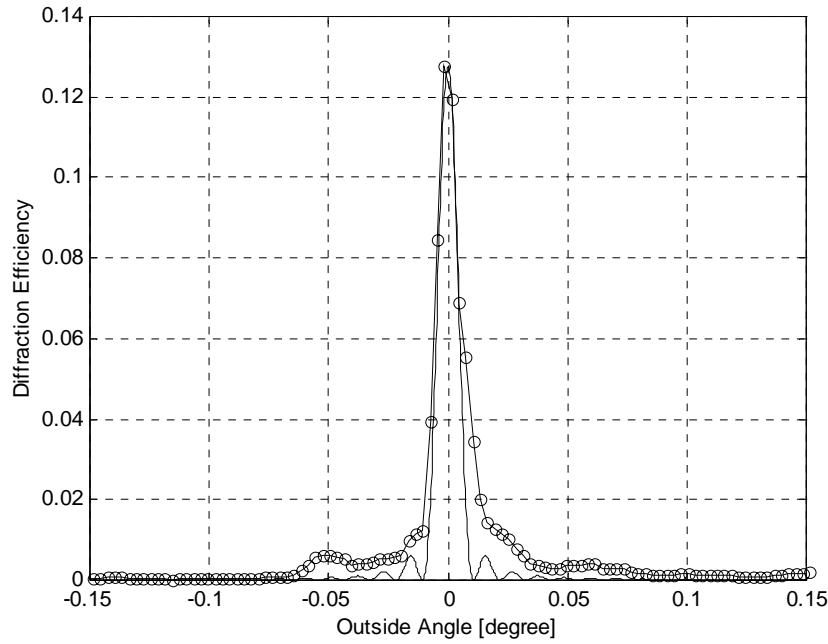
Fig. 3-5. Experimental angular selectivity curve (dots) of a hologram recorded on 5 mm thick LiNbO$_3$ crystal compared to the theory (solid line).

Figure 3-2) on the input plane of the microscope, the hologram will not be Bragg-matched. In other words, the hologram decomposes the input plane into 2 μm thick monochromatic stripes.

The ability of the hologram to image has been tested next. During normal operation (i.e. once the recording process has finished) objective MO2 is retracted so that a specimen can be placed in front of objective MO1 and observed under the microscope using white light illumination. Figure 3-6 shows the image of an 11 μm pixel mask as rendered by the hologram on the CCD camera. For this particular experiment, a ×10/0.25NA objective was used, so a larger field of view can be observed under the holographic microscope.

One of the advantages of the holographic microscope over the more traditional con-focal techniques is that a 2-D image of a depth/color slice of the specimen is obtained
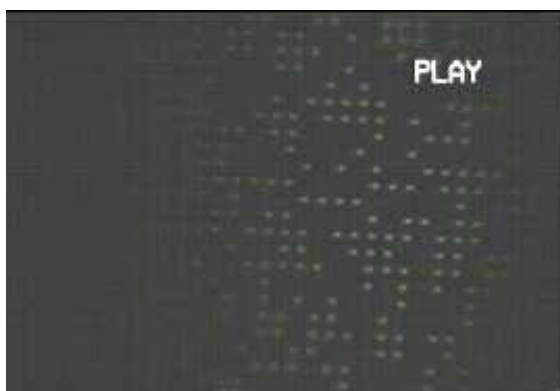
Fig. 3-6.   Image rendered by the hologram on the CCD of an 11 μm pixel mask when illuminated with a white light lamp.

simultaneously rather than just one point of it at a time, thus making unnecessary any mechanical scanning. This property becomes particularly interesting in applications in which information of the specimen needs to be acquired in real time, like, for example, the movement of micron-sized particles in turbulence. In the experiments, an aqueous solution containing 15 μm diameter polystyrene beads was prepared and poured into a container made of micro cover-glass walls. The evolution of the microspheres as they float in the solution was observed under the microscope. Figure 3-7 shows a sequence of four frames in which a single microsphere is tracked as it travels across the field of view of the micro-scope, indicated by the bright vertical stripe in the picture. From frame (a) through (d), the bead goes from the upper-left portion of the bright band to its lower-right corner.

Finally, imaging with multiple holograms has been considered. Five holograms were multiplexed using scheduled recording in the 5 mm thick crystal with a total recording intensity of 12 mW/cm^2. The narrow depth selectivity of the system makes it possible to multiplex depth-slices separated by just 15 μm from each other. Figure 3-8 presents the comb function of the five holograms as the probing point source is scanned in depth

(a)

(b)

(c)

(d)
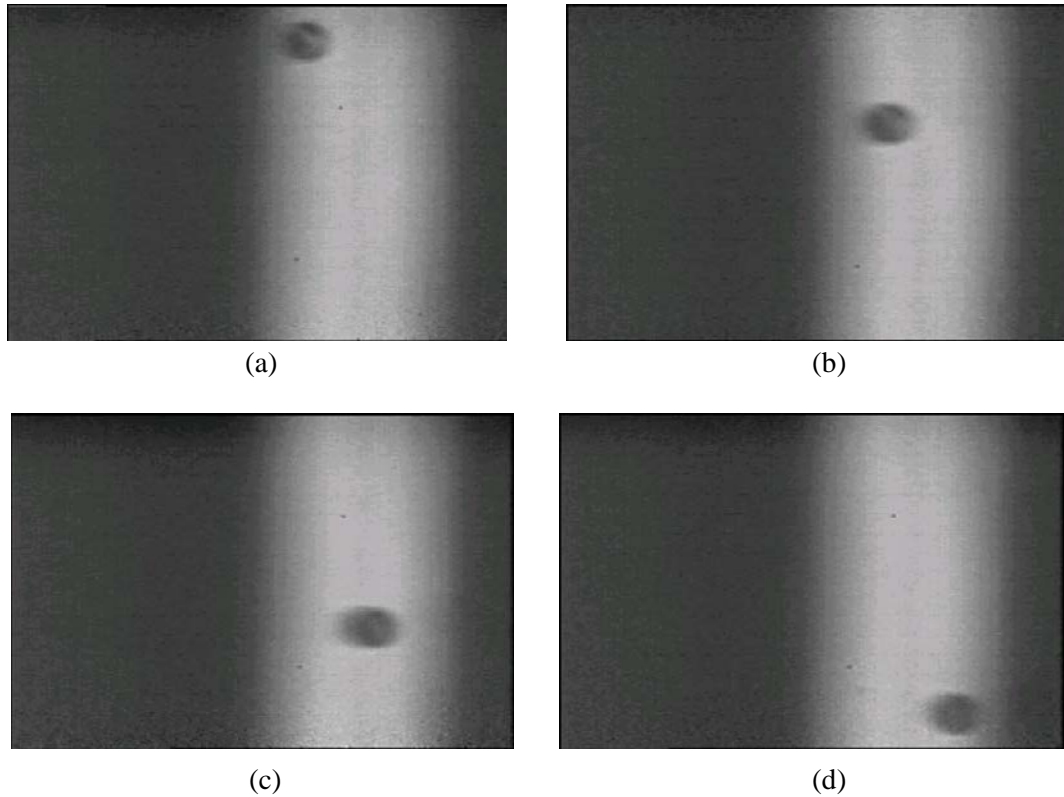
Fig. 3-7. Sequence of four frames, in which (a) is first and (d) is last, obtained with the holographic microscope using a ×40/0.65NA objective of a 15 μm microsphere as it travels across the field of view of the microscope.

(z-axis). Each hologram is projected on the CCD camera with an angular separation of 0.5^{o}.

Again, a solution of suspended microspheres was used as specimen. Figure 3-9 shows the reconstruction of the five holograms when the specimen is illuminated with the laser beam. The holograms appear as narrow vertical stripes on the detector plane, due to the small bandwidth of the laser.

More interesting results can be obtained if broadband light is used to illuminate the specimen, since each one of the stripes in Figure 3-9 broadens and makes it possible to observe the microspheres at different depths without having to physically move the speci-men. Figure 3-10 contains a sequence of three pictures in which a microsphere can be seen
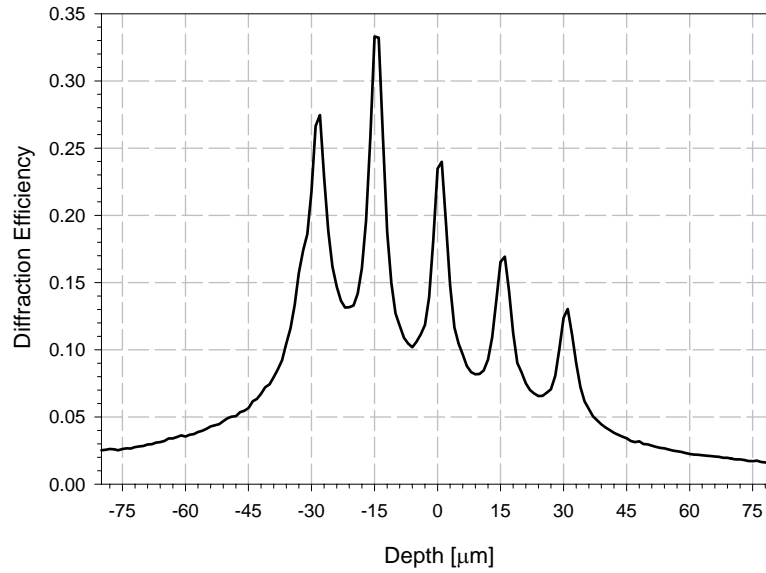
Fig. 3-8.   Scan along the z-axis showing five holograms multiplexed in a 5 mm thick crystal. The holograms are tuned at different depths, with 15 μm spacing, spanning a 60 μm range.
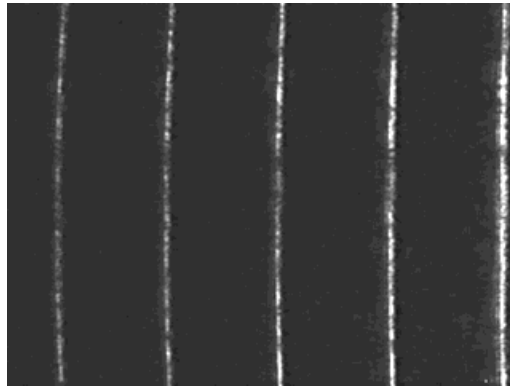
Fig. 3-9.   Simultaneous reconstruction of five depth-multiplexed holograms when a specimen is illuminated with the laser beam.

switching from one stripe to another one as it moves in the solution changing its depth with respect to the microscope objective. As the bead crosses from the left to the right hand side of the image, it also changes its depth. Frame (a) in Figure 3-10, shows a bead on the left-hand side of the image. As the bead moves towards the right and gets to the center of the image, frame (b), a second circular spot appears. This is due to the fact that the microsphere

<div align="center">(a)   (b)   (c)</div>
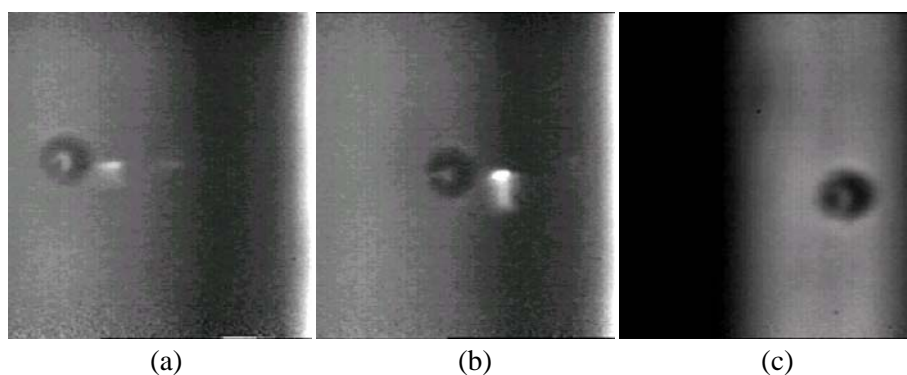
Fig. 3-10. Sequence of three frames showing a microsphere being imaged by two different holograms (on the left and on the right sides of each frame) as the microsphere changes its depth inside the liquid solution from (a) to (c).

begins to be Bragg-matched by a different hologram (i.e., a different depth-slice). By the time the microsphere reaches the right side, frame (c), the original spot has completely vanished and only the second one is visible.

3.0.3 Imaging properties of a reflection-geometry volume hologram

A symmetric reflection-geometry grating has the particularity of being degenerate both in the in-plane and out-of-plane directions. This property can be of special interest when applied to imaging, because an entire 2-D slice of the object would be Bragg-matched to the hologram and thus imaged onto the CCD. This section considers the suitability of a reflection hologram in a system like the 4-D microscope by analyzing the transformation performed by the grating to map the object space into the image plane, and studying how its angular and spectral selectivity influence the transversal and longitudinal (i.e., depth) resolution of the system.

Based on the design of the transmission-geometry microscope presented in Figure 3-2, the reflection-geometry module depicted in Figure 3-11 consists basically of the same elements. The light emitted by the specimen is collimated by lens L1 before it illu-
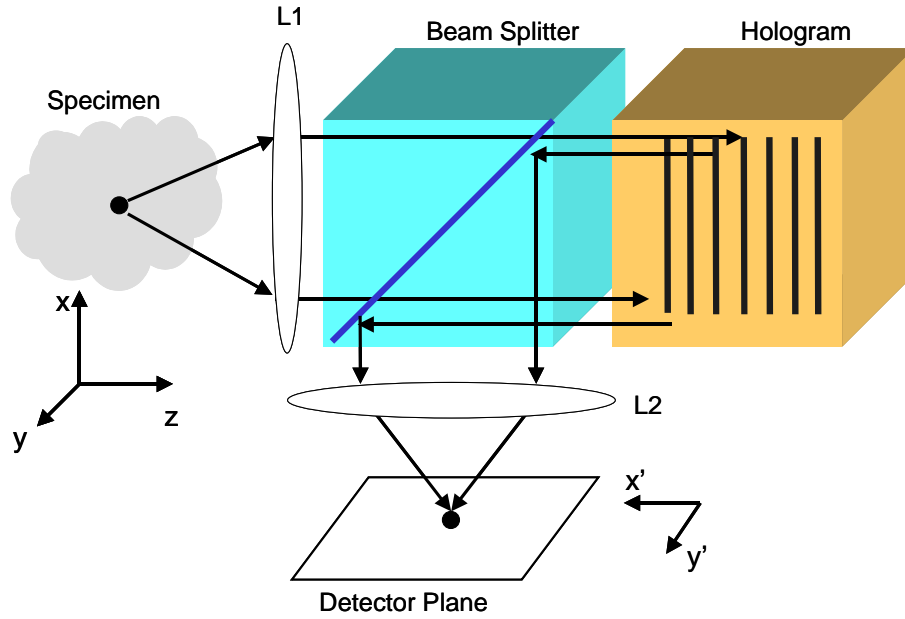
Fig. 3-11.   Schematic diagram of a holographic microscope using a reflection-geometry volume grating. The hologram performs a transformation between the object (i.e., specimen) space (x, y, z) and the image space (x', y'). L1 and L2 are the collimating and imaging lens, respectively.

minates the hologram. The grating senses the collimated wavefront and, depending on its spatial and spectral properties, some of its components are reflected. The beam splitter is used to separate the detector plane, referred to as the (, y')-plane, from the input plane (i.e., the x, y space); and redirects the diffracted light towards the imaging lens (L2).

3.0.3.1 Selectivity and image transformation

Consider a monochromatic point source placed at the focal distance of lens L1 in Figure 3-11 (specified by f_{mo}) and located on the optical axis of the lens (i.e., x=0, y=0). The interference of its collimated wavefront with a plane wave propagating along $-\hat{z}$ records a perfect reflection-geometry grating inside the optical medium defined by the vector $\mathbf{K_G} = -2k \cdot \hat{z}$.

90

If the point source is shifted from its original position along the x-axis by an amount Δx_p, the wavefront after the lens will still be collimated but will propagate with a certain angle $\Delta\theta_R$ with respect to the z-axis. In the paraxial approximation (i.e., $\Delta x_p \ll f_{mo}$), the mapping between position and angle performed by the collimating lens is given by

$$-\frac{\Delta x_p}{f_{mo}} = \Delta\theta_R .$$

(3-2)

As sketched in Figure 3-12, the grating is read out with a slightly tilted reference beam, as
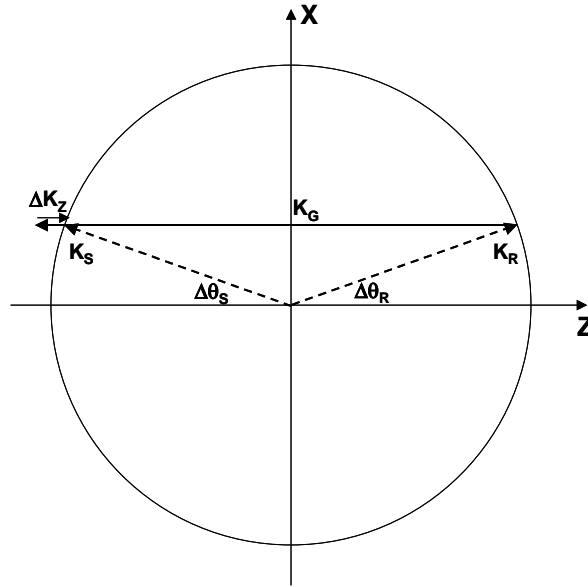
Fig. 3-12.   K-sphere diagram to illustrate the angular Bragg selectivity of a reflection grating.

a result the diffraction propagates along $-\hat{z}$ at an angle $\Delta\theta_S$. Therefore, the wave vectors of the reference ($\mathbf{K_R}$) and signal ($\mathbf{K_S}$) beams take the form:

$$\mathbf{K_R} = k \cdot (\cos\Delta\theta_R \cdot \hat{z} + \sin\Delta\theta_R \cdot \hat{x})$$
$$\mathbf{K_S} = k \cdot (-\cos\Delta\theta_S \cdot \hat{z} + \sin\Delta\theta_S \cdot \hat{x})$$

(3-3)

If the optical medium is assumed to have infinite transversal dimensions and finite thickness along the z-axis (L_z), only the z-component of the diffracted beam can be Bragg-mismatched. In other words, the following vector relation must be satisfied:

$$\mathbf{K_S} = \mathbf{K_R} + \mathbf{K_G} + \Delta K_z \cdot \hat{z} \tag{3-4}$$

The relation $\Delta\theta_S = \Delta\theta_R$ is obtained from the x-component of Equation 3-4, after making the approximation $\sin(\alpha) \approx \alpha$ and $\cos(\alpha) \approx 1 - \dfrac{\alpha^2}{2}$ given that both $\Delta\theta_R$ and $\Delta\theta_S$ are small. This result can be applied in the equation for the z-component to solve for the detuning term (ΔK_z)

$$\Delta K_z = k \cdot (\Delta\theta_R)^2. \tag{3-5}$$

Under Born approximation, the diffraction efficiency of the hologram is related to the amount of detuning by

$$\sqrt{\eta} \sim \mathrm{sinc}\left(\frac{L_z}{2\pi} \cdot \Delta K_z\right). \tag{3-6}$$

The angular Bragg selectivity of the hologram is defined by the first null of the sinc function, which occurs for

$$\Delta\theta_R = \sqrt{\frac{\lambda}{L_z}}. \tag{3-7}$$

Similarly to the collimating lens (L1), the imaging lens (L2 in Figure 3-11) translates the propagation angle of the diffracted beam into a position on the detector plane (i.e., the focal plane of lens L2) as defined by

$$-\frac{\Delta x'_d}{f_i} = \Delta\theta_S, \tag{3-8}$$

where f_i is the focal length of the imaging lens. Combining Equations 3-2 and 3-8, and using the result $\Delta\theta_S = \Delta\theta_R$ from Equation 3-4,

$$\Delta x'_d = -\left(\frac{f_i}{f_{mo}}\right) \cdot \Delta x_p, \tag{3-9}$$

in which the sign reversal comes from the reflection of the incident beam on the hologram. Thus, the hologram performs a linear transformation between points along the x-axis on the input space and points along the x'-axis on the detector plane.

It is worth noticing that the system presents rotational symmetry around the z-axis. Despite the fact that the expression of the angular selectivity has been derived assuming incident and diffracted beams contained in the (x, z)-plane, the orientation of the x- and y-axes is completely irrelevant as the grating is always degenerate. Therefore, the grating is able to perform by itself a 2-D mapping of the (x, y)-plane onto the (x', y')-plane.
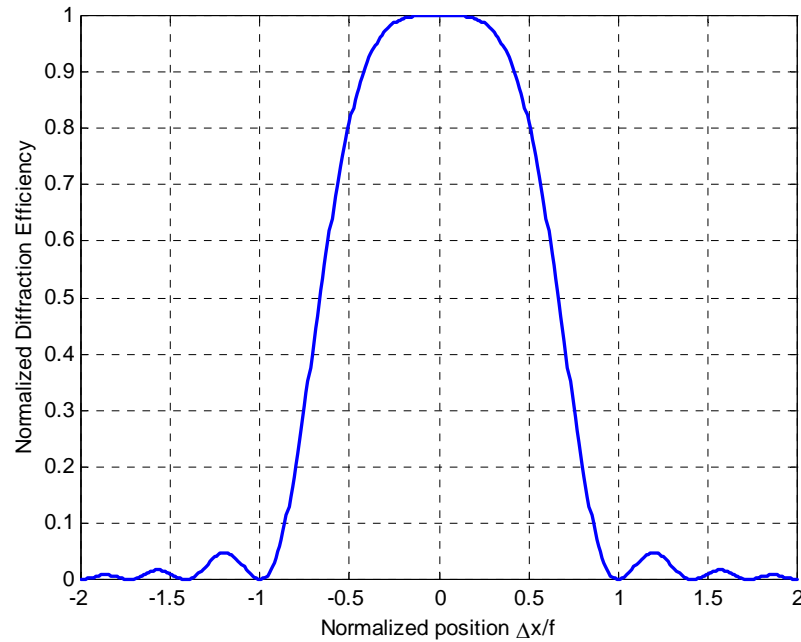

Fig. 3-13.   Normalized diffraction efficiency on detector as a function of the position of a monochromatic point source as it moves along the x-axis.

The amplitude of the imaged points is affected by the sinc function of the hologram (Equation 3-6) as plotted in Figure 3-13. Points along a line that extends beyond the angular selectivity of the grating, will not be relayed to the detector plane. Fortunately, the square-root dependence of $\Delta\theta_R$, due to the degeneracy of the pure reflection grating, results in fairly wide selectivity curve. In the context of the 4-D microscope, the angular selectivity does not determine the transversal resolution of the system (which is solely limited by the numerical aperture of the lenses for a monochromatic point source), but the size of the circular window over which the microscope can observe the specimen. The radius of this disk (ΔX_p) is obtained from combining Equations 3-2 and 3-7, and results in

$$\Delta X_p \;=\; f_{mo} \cdot \sqrt{\frac{\lambda}{L_z}}. \tag{3-10}$$

To illustrate the mapping performed by the hologram, a numerical simulation produces the 2-D intensity distribution of the diffracted spot on the detector plane as a monochromatic point source is shifted along the x-axis. Figure 3-14 shows four instances of a diffraction-limited spot on the detector plane, whose position x'_d changes as the probing point source is shifted in steps of $4.5 \times \lambda$ along the x-axis, but still well within the Bragg selectivity of the hologram.

Consider now the situation in which the readout wavelength (λ') differs from the wavelength used during recording (λ), while the point source remains in the same location as the one during recording. In this case, depicted in Figure 3-15, the wave vectors of the incident and diffracted beams are given by

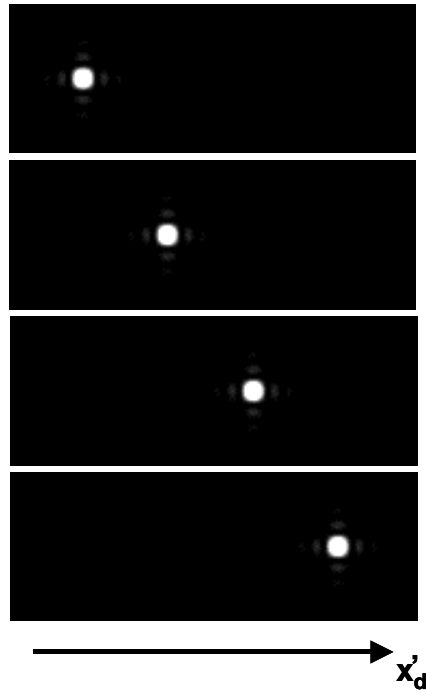Fig. 3-14.   Simulation of the intensity profile and position of the diffracted spot on the detector plane as a monochromatic point source is shifted along the x-axis in $4.5 \times \lambda$ steps. Simulation parameters: λ=514 nm, L_z=200 μm, f_{mo}=4.5 mm, f_i=4.5 mm and NA=0.65.

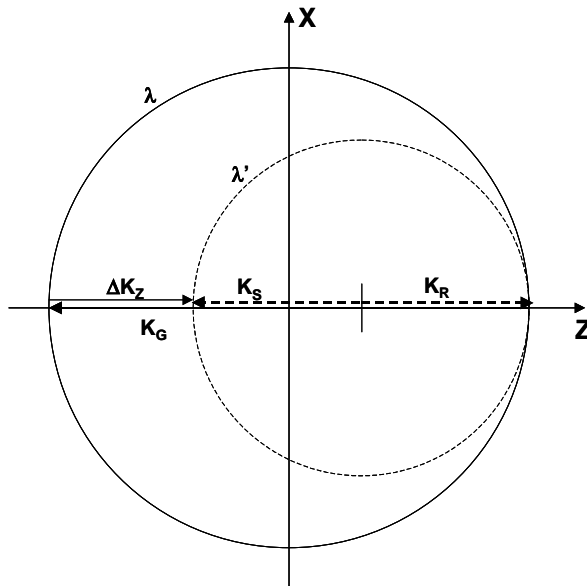Fig. 3-15.   K-sphere diagram to illustrate the wavelength Bragg selectivity of a reflection grating.

$$\mathbf{K_R} = \mathbf{k'} \cdot \hat{z}$$
$$\mathbf{K_S} = -\mathbf{k'} \cdot \hat{z}$$

(3-11)

so in order to satisfy Equation 3-4, the detuning term must be $\Delta K_z = -2 \cdot (k' - k)$. Assuming $k' = k - \Delta k = k \cdot \left(1 + \dfrac{\Delta\lambda}{\lambda}\right)$, the expression in Equation 3-6 hits its first null when

$$\frac{\Delta\lambda}{\lambda} = \frac{\lambda}{2L_z},$$

(3-12)

which is known as the wavelength selectivity of the hologram. Unlike with its angular behavior, the hologram is very sensitive to changes in wavelength. Strong diffraction will occur only when the wavelength used for readout is well within the Bragg selectivity of the hologram.

The numerical simulation in Figure 3-16 shows how the intensity of the diffracted beam profile decreases very rapidly as the wavelength of the probing monochromatic point source is shifted from the Bragg condition in steps of 20% of the value of the wavelength selectivity (Equation 3-12).

To understand how the wavelength selectivity affects the transversal resolution of the microscope, it is necessary to consider the more general case of a slanted (i.e., asymmetric) reflection grating. Suppose two counter-propagating beams with arbitrary angles θ_R and θ_S with respect to the z-axis, their interference results in a grating vector

$$\mathbf{K_G} = k \cdot [(\sin\theta_S - \sin\theta_R) \cdot \hat{x} - (\cos\theta_S + \cos\theta_R) \cdot \hat{z}].$$

(3-13)

Upon readout, the hologram is probed with a beam ($\mathbf{K_R}$) incident at the same angle θ_R but with different wavelength (λ'). Due to the change in wavelength, and in order to verify Equation 3-4, the diffracted beam ($\mathbf{K_S}$) may have to deviate from its initial angle θ_S to a
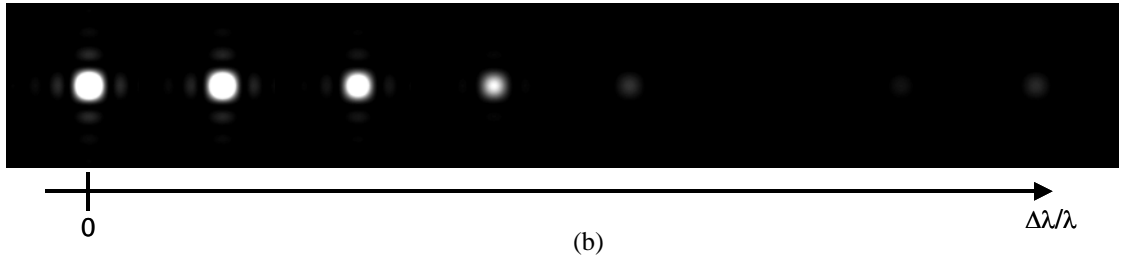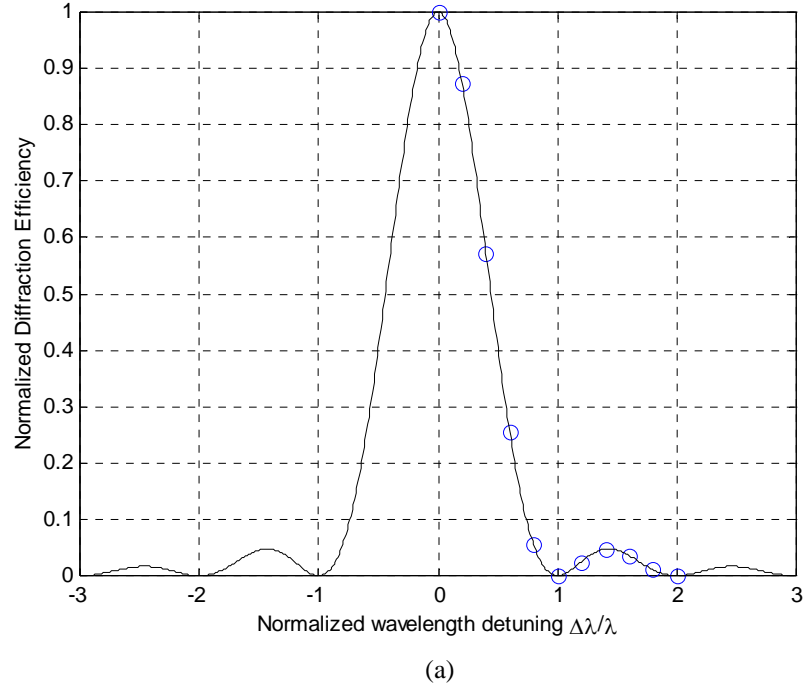
Fig. 3-16. (a) Normalized diffraction efficiency on detector as a function of the wavelength detuning for a monochromatic point source. (b) Simulation of the intensity profile of the diffracted spot on the detector plane as a monochromatic point source changes its emission wavelength in $0.2 \times \Delta\lambda$ steps. The dots in (a) correspond to the points at which wavelength detuning has been simulated. Simulation parameters: $\lambda=514$ nm, $L_z=200$ μm, $f_{mo}=4.5$ mm, $f_i=4.5$ mm and NA=0.65.

new $\theta_S+\Delta\theta_S$. Given the expressions of the wave vectors of the incident and diffracted

beams

$$
\begin{aligned}
\mathbf{K_R} &= k' \cdot [\cos\theta_R \cdot \hat{z} + \sin\theta_R \cdot \hat{x}] \\
\mathbf{K_S} &= k' \cdot [-\cos(\theta_S + \Delta\theta_S) \cdot \hat{z} + \sin(\theta_S + \Delta\theta_S) \cdot \hat{x}]
\end{aligned}, \tag{3-14}
$$

and following a similar derivation as before, it can be easily verified that the wavelength

selectivity of the hologram is given by

97

$$\frac{\Delta\lambda}{\lambda} = \frac{\lambda}{L_z \cdot [1 + \cos(\theta_S + \theta_R)]},$$ (3-15)

which reduces to Equation 3-12 when $\theta_S = \theta_R = 0$. Furthermore, the deflection angle of the diffracted beam is related to the shift in wavelength as

$$\Delta\theta_S = -\frac{\sin\theta_R - \sin\theta_S}{\cos\theta_S} \cdot \left(\frac{\Delta\lambda}{\lambda}\right).$$ (3-16)

Finally, the imaging lens converts the change in angle $\Delta\theta_S$ into a shift in position on the detector plane. The point source that used to be imaged at x'_d for wavelength λ, will be imaged at $x'_d + \Delta x'_d$ for λ', where $\Delta x'_d$ takes the form

$$\Delta x'_d = f_i \cdot [\sin\theta_R - \sin\theta_S] \cdot \left(\frac{\Delta\lambda}{\lambda}\right).$$ (3-17)

This effect has been modeled into the numerical simulation. A slanted grating with angles $\theta_R = 0$ and $\theta_S = 5^o$ is read out by the collimated beam of a monochromatic point source. The sequence of pictures in Figure 3-17 shows the shift along the x'-axis (vertical axis in Figure 3-17) as the wavelength of the probing point source changes in steps of 20% of the spectral selectivity around the Bragg wavelength.

Equation 3-17 is especially important when the point source has a bandwidth, as each spectral component within the selectivity of the hologram will be mapped into a different position on the detector plane, resulting in some sort of rainbow and thus blurring the image of the specimen. Figure 3-18 compares the simulated diffracted spot obtained for a monochromatic source of wavelength λ and the one for a point source with bandwidth from $\lambda - 1.2 \times \Delta\lambda$ to $\lambda + 1.2 \times \Delta\lambda$, shown in Figure 3-18(a) and (b), respectively. The dispersive
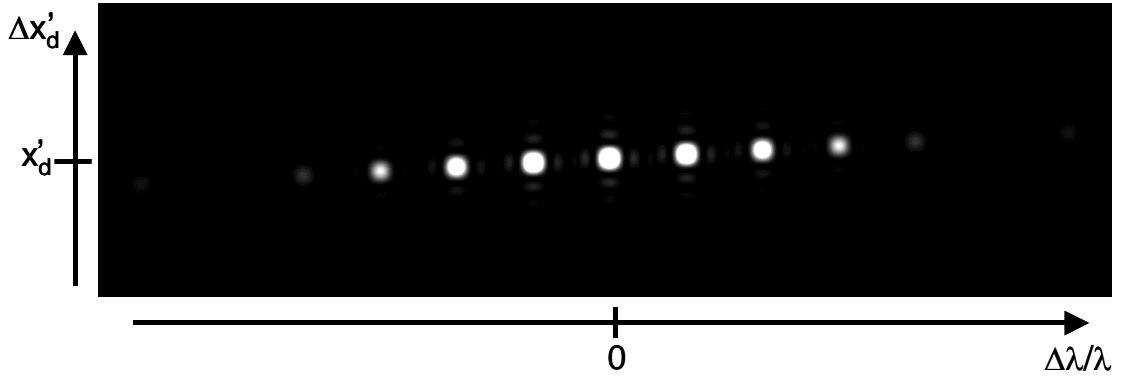
Fig. 3-17. Simulation of the intensity profile and position of the diffracted spot on the detector plane (along the x'-axis) for a slanted grating as a monochromatic point source changes its emission wavelength in $0.2 \times \Delta\lambda$ steps. Simulation parameters: $\theta_R=0^o$, $\theta_S=5^o$, $\lambda=514$ nm, $L_z=200$ μm, $f_{mo}=4.5$ mm, $f_i=4.5$ mm and NA=0.65.

behavior of the grating degrades the resolution of the microscope, as it can be appreciated

in the widening of the diffracted spot in the cross-sectional plot in Figure 3-18(c).

Therefore, the wavelength selectivity plays a key role in defining the transversal

resolution of the holographic microscope. The best resolution can be achieved using a sym-

metric grating, because $\Delta x'_d = 0$ when $\theta_S=\theta_R$. In this particular case the transversal reso-

lution is only limited by the numerical aperture of the lenses in the system. However, the

need to multiplex several holograms to image various color bands and depths on different

regions of the detector plane, makes necessary to introduce some slant in the gratings.

3.0.3.2 Spatial and wavelength coupling

The previous section showed that the hologram is selective in wavelength and capa-

ble of imaging points in a neighborhood of the z-axis (i.e., point x=0, y=0). This section

will consider the coupling between position and color that, like in the transmission-geom-

etry microscope, permits to extend the field of view of the microscope beyond the spatial

99

(a)   (b)

(c)
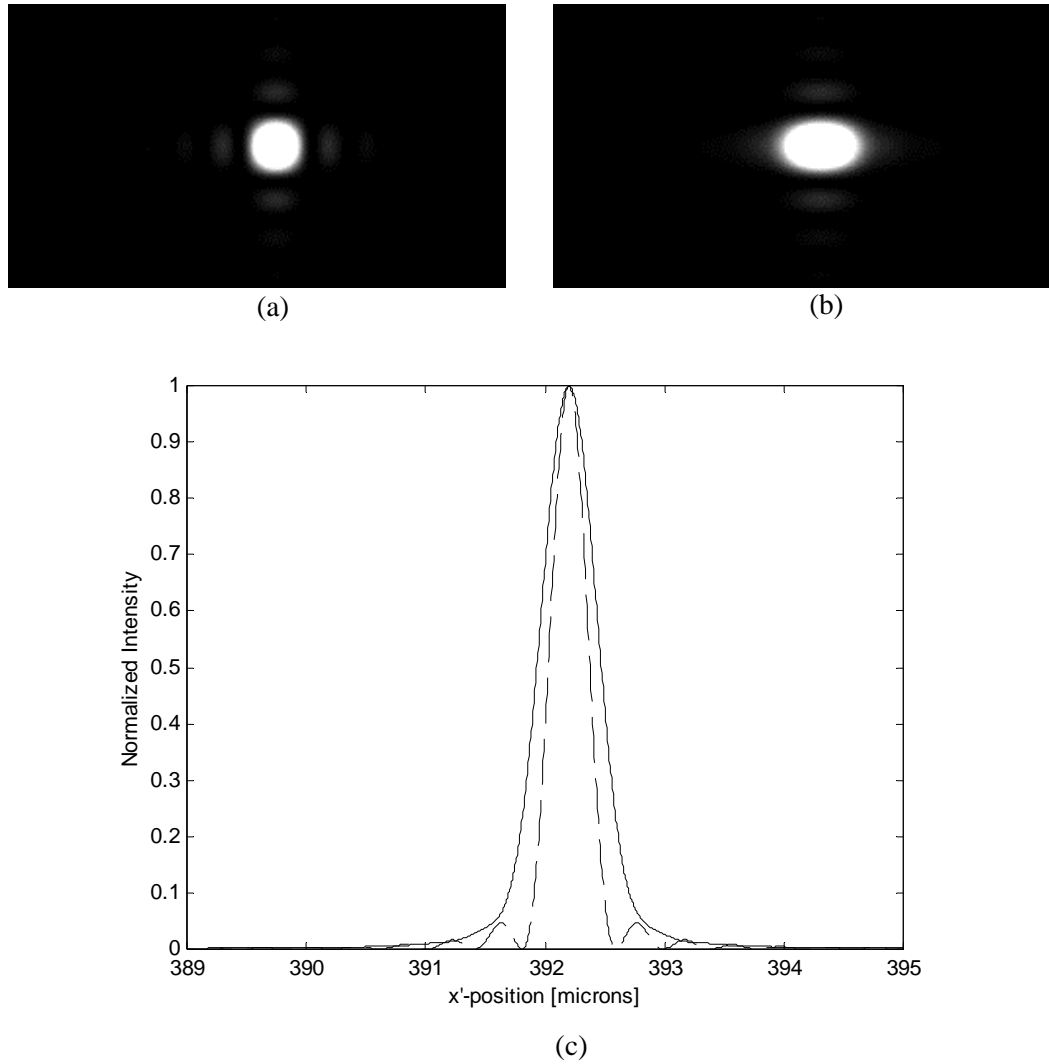
Fig. 3-18. Simulation of the intensity profile of the diffracted spot on the detector plane produced by a slanted grating for (a) a monochromatic point source with emission wavelength λ and (b) a chromatic point source with bandwidth $\lambda \pm 1.2 \times \Delta\lambda$. (c) Comparison of the intensity of the diffracted spot for a cross-sectional cut along the x'-axis for the monochromatic (dashed line) and the chromatic (solid line) point sources. Simulation parameters: $\theta_R=0^o$, $\theta_S=5^o$, $\lambda=514$ nm, $L_z=200$ μm, $f_{mo}=4.5$ mm, $f_i=4.5$ mm and NA=0.65.

selectivity of the hologram; and will also study the dependence of the spatial and wave-length selectivity for an arbitrary point on the (x, y)-plane.

To analyze the coupling between position and wavelength, consider again a sym-metric reflection grating. The detuning term is given by

100

$$\Delta K_z = -2k' \cdot \cos\theta + 2k, \tag{3-18}$$

where θ is measured with respect to the z-axis. Coupling is achieved when the hologram is Bragg-matched (i.e., $\Delta K_z = 0$). Let $r = \sqrt{x^2 + y^2}$ be the distance of point (x, y) to the z-axis, then $\tan\theta = -\dfrac{r}{f_{mo}}$. In the Bragg-matched case, Equation 3-18 can be re-written as

$$r^2 = f_{mo}^2 \cdot \left[\left(\frac{k'}{k}\right)^2 - 1\right], \tag{3-19}$$

which means that the points on a circle of radius r around the z-axis can be imaged onto the detector plane if they emit light at λ'. Figure 3-19 indicates the relative change in wave-

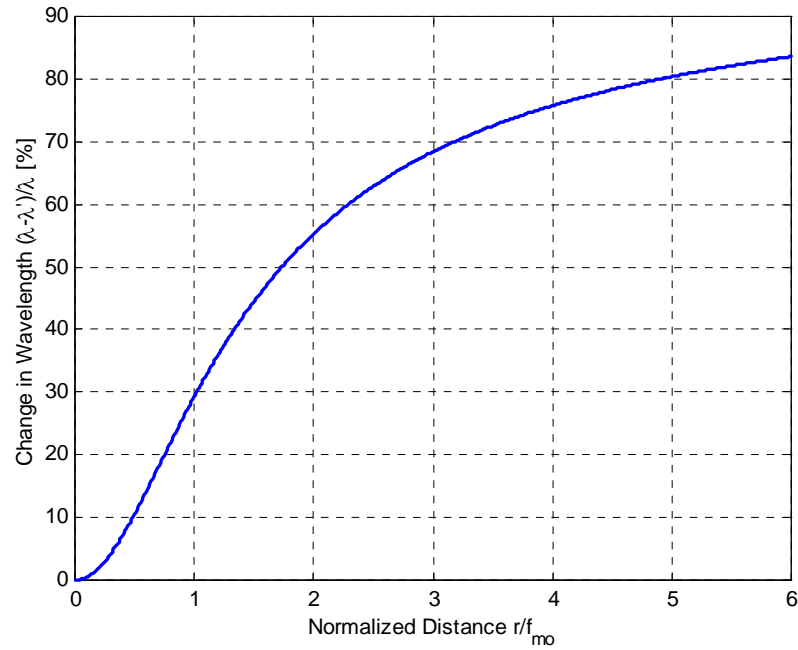Fig. 3-19. Relative change with respect to λ of the emission wavelength of a monochromatic point source required to satisfy the Bragg condition as a function of the distance of the point source from the z-axis.

length required to satisfy Equation 3-19. Therefore, a full 2-D image can be obtained on the detector by sectioning the input plane into monochromatic concentric circles when the

specimen is illuminated with an extended broadband source. It is worth noticing in Equation 3-19 that coupling is only possible for $\lambda' < \lambda$, which is a consequence of $\mathbf{K_G}$ being a 180° grating for wavelength λ.

Consider first the case of angular detuning. Assume $\theta = \theta_o + \Delta\theta$, with θ_o being the Bragg angle. After cancelling out the Bragg-matched terms, Equation 3-18 becomes

$$\Delta K_z = k' \cdot \cos\theta_o \cdot \Delta\theta^2 + 2k' \cdot \sin\theta_o \cdot \Delta\theta \ . \tag{3-20}$$

Using the relation $\Delta\theta = -\dfrac{\Delta r}{f_{mo}}$, valid under the paraxial approximation, the radius of spatial selectivity (Δr) for an arbitrary point located at a distance r from the z-axis is given by

$$\left(\frac{\Delta r}{f_{mo}}\right)^2 + 2\left(\frac{\Delta r}{f_{mo}}\right) \cdot \frac{r}{f_{mo}} = \frac{\lambda}{L_z} \ . \tag{3-21}$$

The solution to Equation 3-21 is plotted in Figure 3-20, assuming a medium of thickness
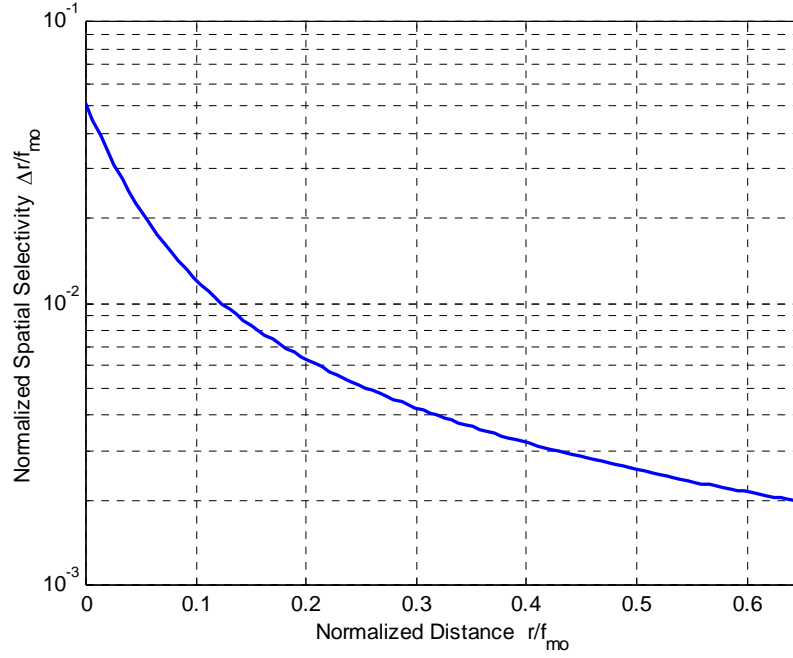

Fig. 3-20.   Radius of the disk of spatial selectivity (Δr) for a monochromatic point source as a function of the distance of the source from the z-axis, assuming a material of thickness $L_z=390 \times \lambda$.

$L_z=390 \times \lambda$. The more off-axis a point is located on the (x, y)-plane, the smaller its spatial selectivity, and consequently the smaller the size of the window that can be imaged by the 4-D microscope.

Similarly, the wavelength detuning can be analyzed assuming $k' = k'_o + \Delta k'$, with Bragg match occurring for $\Delta k'=0$, in Equation 3-18. After simplifying the Bragg-matched terms, the spectral selectivity for a point whose Bragg wavelength λ'_o results in

$$\frac{\Delta \lambda'}{\lambda'_o} = \frac{\lambda}{2L_z}. \qquad (3\text{-}22)$$

103

Equation 3-22 says that the relative wavelength selectivity of the hologram is constant over the entire (x, y)-plane. Plugging Equation 3-19 into 3-22, the spectral selectivity can be explicitly related to position as

$$\Delta\lambda' = \frac{\lambda^2}{2L_z} \cdot \frac{1}{1 + \left(\frac{r}{f_{mo}}\right)^2} . \tag{3-23}$$

Thus, the farther the point source is from the z-axis, the narrower the portion of its spectrum that can be Bragg-matched by the hologram.

3.0.3.3 Depth selectivity

As the point source shifts along the z-axis, the wavefront after the collimating lens (L1) is no longer a plane wave. As the probing beam changes its sphericity, the hologram gradually becomes Bragg-mismatched. A simple analytical approximation can be obtained by decomposing the spherical wave into its spatial frequency components. Each component is a plane wave propagating with angle θ, for which the response of the hologram can be easily calculated. The diffraction efficiency for a monochromatic point source shifted by Δz_p from the focal plane of lens L1 is approximately

$$\eta(\Delta z_p) \cong \frac{1}{\theta_{max}} \int_0^{\theta_{max}} \mathrm{sinc}\left(\frac{L_z}{2\pi} \cdot [2k - 2k' \cdot \cos\theta]\right)^2 \cdot d\theta , \tag{3-24}$$

where the range of transverse spatial components is determined by the amount of defocusing of the point source and the numerical aperture of the lens L1 and results in

$$\theta_{max} = NA \cdot \frac{\Delta z_p}{f_{mo}} . \tag{3-25}$$

104

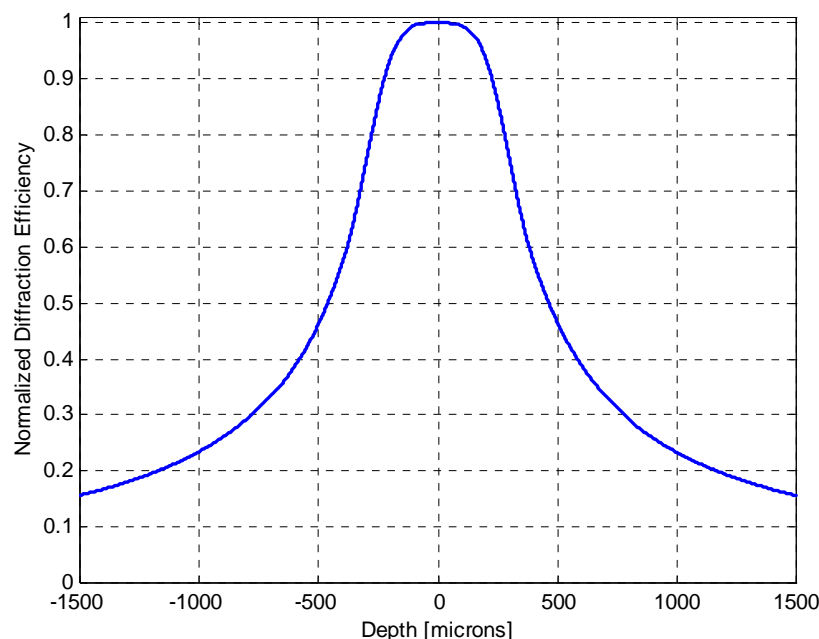Equation 3-24 is solved numerically and plotted in Figure 3-21 for the case L_z=200 μm,

Fig. 3-21. Normalized diffraction efficiency as a function of the position along the z-axis of a monochromatic point source. Simulation parameters: λ=514 nm, L_z=200 μm, f_{mo}=4.5 mm, f_i=4.5 mm and NA=0.65.

λ=514 nm and f_{mo}=4.5 mm. The wide angular selectivity of the reflection hologram results,

as seen in Figure 3-21, in a poor performance to discriminate point sources located at dif-

ferent depths. Therefore, the hologram does not improve the depth of focus of the micro-

scope, which is limited by the numerical aperture of the lenses. On the contrary, it increases

the level of background noise as the hologram cannot filter out light originating at different

depths.

Finally, it is interesting to point out the coupling between depth and wavelength for

a chromatic point source. Figure 3-22 presents the simulation results of the depth scan

along the z-axis for a point source as its wavelength of emission is changed. As the figure

indicates, the hologram can be partially Bragg-matched at shorter wavelengths if the point source is shifted away from the focal plane of the collimating lens. This happens because some of the components of the defocused probing beam can better satisfy the Bragg condition. The figure exhibits an asymmetric behavior in wavelength. This is due to the fact that coupling between depth and wavelength is not possible for wavelengths longer than the Bragg wavelength, which is consistent with the result from Equation 3-19 and, as mentioned earlier, is just the consequence of $\mathbf{K_G}$ being a 180° grating for wavelength λ.
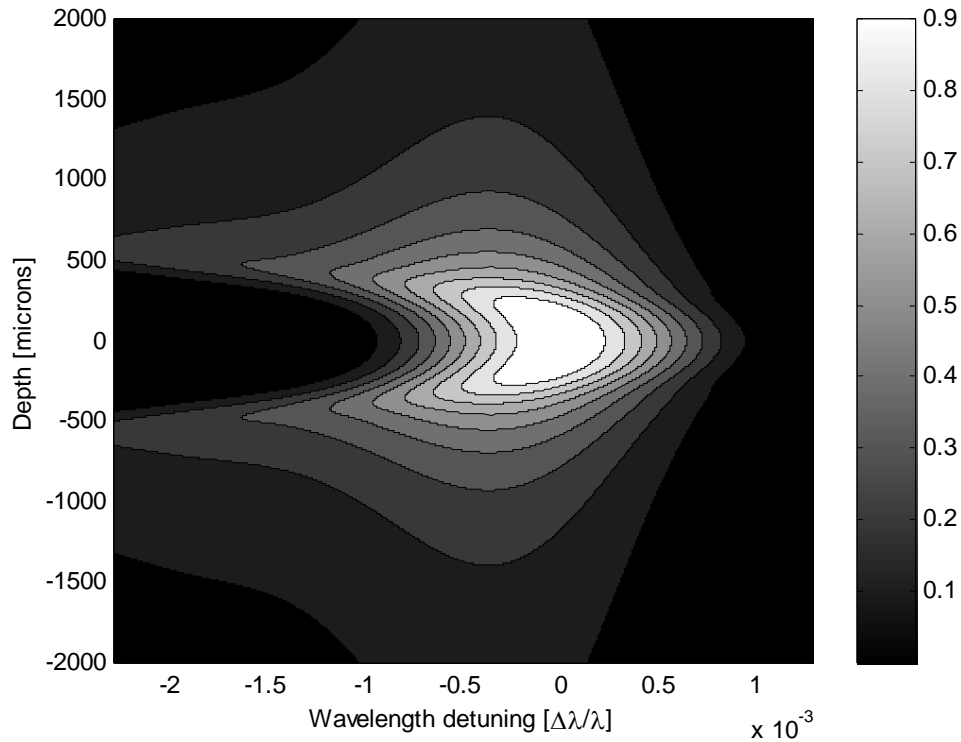

Fig. 3-22. Normalized diffraction efficiency of the hologram (color-coded in grayscale) as a function of the position along the z-axis of a monochromatic point source (vertical axis in the figure) and detuning of its wavelength of emission (horizontal axis).

3.0.4 Discussion

Both the results from experiments done with the transmission-geometry microscope and the theoretical analysis of the reflection-geometry module reveal that the resolution of

the system is in large measure determined by the quality of the collimating and imaging lenses. In this sense, the holographic microscope does not outperform other more conventional solutions used in microscopy. Nonetheless, the 4-D microscope can show its superior performance over competing technologies in the arena of applications that require real-time visualization of the specimen. The 4-D microscope is better suited for those situations in which it is paramount to gather multispectral or multidepth information of the specimen. While its competitors need to trade in resolution in order to gain speed, the holographic microscope can keep the same level of resolution while offering high speed.

The parallel processing ability of the 4-D microscope, in fact, inherent to most holographic systems, derives from the capability of multiplexing various holograms in the optical medium. However, this parallelism comes at the expense of dividing the photon count on the microscope. Therefore, to increase the light efficiency of the system, it is necessary to act either on the holographic material to improve its performance (e.g., larger M/#), or on the hologram to widen its spectral response (e.g., chirping the hologram), or even on the specimen itself by using more efficient and narrow-band fluorescent markers (e.g., quantum dots) [3-6], [3-7].

Finally, the wavelength selectivity of the hologram poses a trade-off between light collection efficiency and resolution. A broad wavelength selectivity benefits the photon count in the microscope, but at the same time degrades its transversal resolution. Fortunately, the reflection geometry can be of assistance in breaking this trade-off as for this geometry the resolution of the system is less sensitive to the bandwidth of the hologram.

Reference

[3-1] G. Barbastathis, M. Balberg, and D. J. Brady, "Confocal microscopy with a volume holographic filter," *Optics Letters* **24**, 811-813 (1999).

[3-2] G. G. Yang, H. S. Chen, and E. N. Leith, "Volume reflection holographic confocal imaging," *Applied Optics* **39**, 4076-4079 (2000).

[3-3] G. Barbastathis, and D. J. Brady, "Multidimensional tomographic imaging using volume holography," *Proceedings of the IEEE* **87**, 2098-2120 (1999).

[3-4] D. W. Piston, "Imaging living cells and tissues by two-photon excitation micros-copy," *Trends in Cell Biology* **9**, 66-69 (1999).

[3-5] A. Diaspro, and M. Robello, "Two-photon excitation of fluorescence for three-dimensional optical imaging of biological structures," *Journal of Photochemistry and Photobiology B-Biology* **55**, 1-8 (2000).

[3-6] M. Bruchez, M. Moronne, P. Gin, S. Weiss, and A. P. Alivisatos, "Semiconductor nanocrystals as fluorescent biological labels," *Science* **281**, 2013-2016 (1998).

[3-7] M. Han, X. Gao, J. Z. Su, and S. Nie, "Quantum-dot-tagged microbeads for multi-plexed optical coding of biomolecules," *Nature Biotechnology* **19**, 631 - 635 (2001).